

Special Section:

The Arctic: An AGU Joint Special Collection

This article is a companion to 2019JC015900RR.

Key Points:

- Lagrangian snow-on-sea-ice simulations revealed high-resolution, snow property spatial structures associated with ice motion
- Ice age, associated with ice dynamics, strongly controlled the spatial distributions and temporal evolution of snow properties
- A new, high resolution snow depth and density product is available for Arctic snow and sea ice studies and applications

Correspondence to:

G. E. Liston,
glen.liston@colostate.edu

Citation:


Liston, G. E., Itkin, P., Stroeve, J., Tschudi, M., Stewart, J. S., Pedersen, S. H., et al. (2020). A Lagrangian snow-evolution system for sea-ice applications (SnowModel-LG): Part I—Model description. *Journal of Geophysical Research: Oceans*, 125, e2019JC015913. <https://doi.org/10.1029/2019JC015913>

Received 25 NOV 2019

Accepted 5 AUG 2020

Accepted article online 6 AUG 2020

A Lagrangian Snow-Evolution System for Sea-Ice Applications (SnowModel-LG): Part I—Model Description

Glen E. Liston¹ , Polona Itkin² , Julianne Stroeve^{3,4} , Mark Tschudi⁵, J. Scott Stewart⁵, Stine H. Pedersen^{1,6}, Adele K. Reinking¹, and Kelly Elder⁷

¹Cooperative Institute for Research in the Atmosphere (CIRA), Colorado State University, Fort Collins, CO, USA,

²Department of Physics and Technology, UiT The Arctic University of Norway, Tromsø, NORWAY, ³Earth Sciences, University College London, London, UK, ⁴National Snow and Ice Data Center (NSIDC), University of Colorado Boulder, Boulder, CO, USA, ⁵Colorado Center for Astrodynamics Research (CCAR), University of Colorado Boulder, Boulder, CO, USA, ⁶Department of Biological Sciences, University of Alaska Anchorage, Anchorage, AK, USA, ⁷Rocky Mountain Research Station, USDA Forest Service, Fort Collins, CO, USA

Abstract A Lagrangian snow-evolution model (SnowModel-LG) was used to produce daily, pan-Arctic, snow-on-sea-ice, snow property distributions on a 25 × 25-km grid, from 1 August 1980 through 31 July 2018 (38 years). The model was forced with NASA's Modern Era Retrospective-Analysis for Research and Applications-Version 2 (MERRA-2) and European Centre for Medium-Range Weather Forecasts (ECMWF) ReAnalysis-5th Generation (ERA5) atmospheric reanalyses, and National Snow and Ice Data Center (NSIDC) sea ice parcel concentration and trajectory data sets (approximately 61,000, 14 × 14-km parcels). The simulations performed full surface and internal energy and mass balances within a multilayer snowpack evolution system. Processes and features accounted for included rainfall, snowfall, sublimation from static-surfaces and blowing-snow, snow melt, snow density evolution, snow temperature profiles, energy and mass transfers within the snowpack, superimposed ice, and ice dynamics. The simulations produced horizontal snow spatial structures that likely exist in the natural system but have not been revealed in previous studies spanning these spatial and temporal domains. Blowing-snow sublimation made a significant contribution to the snowpack mass budget. The superimposed ice layer was minimal and decreased over the last four decades. Snow carryover to the next accumulation season was minimal and sensitive to the melt-season atmospheric forcing (e.g., the average summer melt period was 3 weeks or 50% longer with ERA5 forcing than MERRA-2 forcing). Observed ice dynamics controlled the ice parcel age (in days), and ice age exerted a first-order control on snow property evolution.

Plain Language Summary This study used a high resolution, snow-evolution model to simulate both snow depth and snow density over Arctic sea ice, filling a critical data gap in polar science. The model was run from 1 August 1980 through 31 July 2018 and produced a new snow-on-sea-ice map every day across the Arctic Ocean. This daily snow depth and snow density data set will be used to improve how Earth-System models represent Arctic snow and ice processes.

1. Introduction

Snow-on-sea-ice is a key component of Earth's climate system. It serves as an insulating blanket that influences heat and moisture exchanges between the ocean and the atmosphere, and it plays a key role in defining the surface energy budget. The snow generally follows a seasonal evolution, accumulating during winter and melting during summer. During this seasonal cycle, numerous snow features, such as snow-water-equivalent (SWE), density, grain size and habit, albedo, and thermal conductivity, are continuously changing. The interaction of all these properties result in seasonal evolutions of snow depth and snow density, variables that are commonly measured in the field and typically represented in numerical models.

This snow evolution has important interactions and feedbacks with the rest of the sea ice system. For example, the snow depth and thermal properties impact thermodynamic ice growth during winter (e.g., Maykut & Untersteiner, 1971). In addition, winter snow distributions and properties are known to influence summer melt pond formation and total pond area, thus impacting melt-season albedo evolution (e.g., Petrich

©2020. The Authors.

This is an open access article under the terms of the Creative Commons Attribution-NonCommercial License, which permits use, distribution and reproduction in any medium, provided the original work is properly cited and is not used for commercial purposes.

et al., 2012; Polashenski et al., 2012). Snow also plays a key role in light penetration to the ocean below (e.g., Hancke et al., 2018; Mundy et al., 2005) and snow impacts surface flooding and snow-ice formation (e.g., Granskog et al., 2017; Provost et al., 2017).

On sea ice, pan-Arctic snow depth and density estimates have made strong use of a climatology derived from snow measurements made decades ago (Warren et al., 1999). This climatology is likely no longer relevant considering recent changes in atmospheric forcing, sea ice extent, thickness, motion, and age (e.g., Lindsay & Schweiger, 2015; Rampal et al., 2009; Stroeve & Notz, 2018). In addition, this climatology is based on snow measurements over multiyear ice (MYI). Snow on MYI is known to have different properties than snow on the first-year ice (FYI) that dominates the Arctic today (e.g., Kwok, 2018; Maslanik et al., 2007, 2011; Perovich et al., 2019). The ice seasonality is also changing, including a later onset of ice freeze-up and snow accumulation (Markus et al., 2009; Stroeve & Notz, 2018). These changes will impact snow accumulation quantities, snow distribution patterns, and the evolution of key snow properties (Hezel et al., 2012).

Given the strong role that snow-on-sea-ice plays in Earth's climate system, and the fact that the system is changing, it is imperative to develop state-of-the-art tools that realistically and accurately represent the spatial and temporal variability and evolution of snow properties in sea ice environments. Recent studies have accumulated snowfall outputs from atmospheric reanalyses in either Eulerian or Lagrangian frameworks. These have produced more realistic snow depth estimates than those defined by the climatologies alone. The first physically based modeling approaches (e.g., Blanchard-Wrigglesworth et al., 2018; Kwok & Cunningham, 2008; Petty et al., 2018) provided an attractive alternative to using climatologies, particularly in a rapidly changing climate system.

These initial modeling approaches took two paths: (1) they used a single atmospheric reanalysis data set and performed a simple snow accumulation using a temperature threshold to define snowfall from water-equivalent precipitation inputs, prescribed the snow density using Warren et al. (1999) monthly climatologies, and used a Lagrangian parcel-tracking framework (Blanchard-Wrigglesworth et al., 2018; Kwok & Cunningham, 2008; Webster et al., 2019), or (2) they implemented a simple two-layer, winter-only (no snow melt), snow-budget model in a Eulerian framework with multiple reanalysis data sets (Petty et al., 2018). Although undeniably superior to using the Warren et al. (1999) climatology, these past attempts were performed at relatively coarse resolutions of 75 (Blanchard-Wrigglesworth et al., 2018) and 100 km (Petty et al., 2018). While these resolutions are likely adequate to capture synoptic-scale meteorological forcing conditions, they are insufficient to represent ice dynamical processes that also play an important role in snow evolution in sea ice environments. Petty et al. (2018) used several reanalyses to account for important biases in precipitation and temperature that exist among the different reanalysis data sets (Barrett et al., 2020; Boisvert et al., 2018). Kwok et al. (2017) and Boisvert et al. (2018) used airborne data to analyze snow depth information over specific flight lines and parcel trajectories. Yet none of these approaches accounted for the complete suite of physical processes impacting snow depth and density evolution in the Arctic system.

This study implemented a state-of-the-art, physically based, snow-evolution model in a Lagrangian framework. The model was used to simulate 3-hourly snow property evolution on sea ice, from 1 August 1980 through 31 July 2018 (38 years), on approximately 61,000 sea ice parcels that averaged 14×14 km in size. The novel physical processes simulated by the model include snow density and grain size evolution, blowing-snow sublimation, snow melt, and superimposed ice formation. The simulations were forced with two state-of-the-art atmospheric reanalyses and included a data assimilation procedure to help correct uncertainties in the reanalyses precipitation forcings. This paper (Part I) describes the model, the modeling approach, the Lagrangian simulation method, the input data sets, and the general model results. A companion paper (Part II; Stroeve et al., 2020) compared the model outputs with snow depth estimates from field campaigns, ice mass balance buoys, passive microwave remote sensing, and various snow climatologies. Part II also evaluated the snow-related differences between the two reanalyses, the simulated interannual variability, and the 38-year trends in key snow properties.

2. Methods

2.1. Lagrangian SnowModel (SnowModel-LG)

This study builds on a physically based, Lagrangian snow-on-sea-ice model (SnowModel-LG) developed by Liston et al. (2018) to evolve snow on sea ice parcels using atmospheric inputs of air temperature, relative

humidity, wind speed and direction, and water-equivalent precipitation, and sea ice inputs of ice concentration and parcel motion. The foundation of SnowModel-LG is a terrestrial snow modeling system (called SnowModel) that has been developed over the last three decades (see Liston & Elder, 2006a, and the references contained therein). In the discussions that follow, “SnowModel/SnowModel-LG” refers to the general modeling system, and “SnowModel-LG” refers specifically to Lagrangian sea ice applications (either to this application or others, depending on the context). SnowModel/SnowModel-LG includes the physics required to simulate all the first-order processes that govern the seasonal evolution of snow depth, snow density, and other snow properties over sea ice. These include blowing-snow redistribution and sublimation, density evolution, snow grain size and habit metamorphism, and thermal conductivity, all in a spatially distributed, time-evolving, multilayer snowpack framework. A general overview of SnowModel/SnowModel-LG is provided in Appendices A–H.

SnowModel/SnowModel-LG includes components that (1) simulate the snowpack and surface energy balance (EnBal) (Liston, 1995; Liston et al., 1999); (2) calculate multilayer snow properties, including snow depth, density, temperature, and SWE (SnowPack-ML) (Liston & Hall, 1995; Liston & Mernild, 2012); (3) represent blowing-snow processes (SnowTran-3D) (Liston et al., 2007; Liston & Sturm, 1998); (4) produce high-resolution (meter-scale) snow bedforms over level land or ice (SnowDunes) (Liston et al., 2018); and (5) perform data assimilation procedures (SnowAsim) (Liston & Hiemstra, 2008). The model is forced with atmospheric information from either atmospheric (re)analyses or automatic weather stations using MicroMet (Liston & Elder, 2006b).

An early version of SnowModel-LG was validated over level and ridged sea ice using snow and atmospheric data collected during the Norwegian young sea ICE field expedition in 2015 (N-ICE 2015; Liston et al., 2018). That validation focused on how well SnowModel-LG simulated wind-related snow redistribution around pressure ridges and snow dune formation on level ice. Using simulations that spanned 1 year (summer 2014 through summer 2015), SnowModel-LG was run over a 1.5×1.5 -km domain using a 1-m horizontal resolution and a 3-hr time step. SnowModel-LG reproduced the observed snow depth variability on level ice areas and between pressure ridges within a margin of one standard error (Liston et al., 2018).

While Liston et al. (2018) followed a single ice parcel, the application presented herein follows over 61,000 ice parcels in a pan-Arctic application. At every time step, SnowModel-LG performs a mass-budget calculation (Appendix B), where SWE depth, SWE (m), is defined by mass gains, losses, and Lagrangian ice dynamics (defined to include ice-parcel drift vectors, the formation of new parcels, the loss of old parcels, and changes in parcel size; these are prescribed using parcel trajectory and concentration data sets),

$$\frac{dSWE}{dt} = \frac{1}{\rho_w} [(P_r + P_s) - (S_{ss} + S_{bs} + M) + D], \quad (1)$$

where t (s) is time; $\rho_w = 1,000 \text{ kg m}^{-3}$ is the water density; P_r and P_s are the water-equivalent rainfall and snowfall fluxes ($\text{kg m}^{-2} \text{ s}^{-1}$), respectively; S_{ss} ($\text{kg m}^{-2} \text{ s}^{-1}$) and S_{bs} ($\text{kg m}^{-2} \text{ s}^{-1}$) are the water-equivalent sublimation from static-surface (a nonblowing-snow surface; this term also accounts for vapor deposition on the snow surface) and blowing-snow processes, respectively; M ($\text{kg m}^{-2} \text{ s}^{-1}$) is melt-related mass losses (meltwater that has been removed from the snowpack, not refrozen within the snowpack); and D ($\text{kg m}^{-2} \text{ s}^{-1}$) represents mass loss and gain from sea ice dynamics processes (this includes parcels created and lost through ice motion, divergence, and convergence). For each parcel, all the terms except D in Equation 1 are tracked, at each time step, using SnowModel-LG. At the end of each time step, the parcels are gridded to a rectangular grid, and D is calculated as the residual of all the other terms in Equation 1 (by moving D to the left-hand side of Equation 1 and placing all the other terms on the right-hand side). This application grids the parcel data to the 25×25 -km, National Snow and Ice Data Center (NSIDC) Equal-Area Scalable Earth (EASE) grid (Brodzik & Knowles, 2002).

Equation 1 does not include three of the mass budget terms included in Appendix B, Equation B1. One of those terms is related to sublimation of snow intercepted by forest canopies, and a scale analysis shows the other two terms (snow bedforms $O(1\text{--}10 \text{ m})$ and snow depth variability due to local-scale topographic variability $O(1\text{--}500 \text{ m})$) are negligible for an application where grid increments are greater than a few kilometers (such as the application presented herein).

Snow depth, h_s (m), is related to SWE through the ratio of the snow density, ρ_s (kg m^{-3}), and water density, as shown in Appendix B, Equation B3. Therefore, the snow depth and snow density distributions and evolutions are calculated from

$$\frac{d(\rho_s h_s)}{dt} = (P_r + P_s) - (S_{ss} + S_{bs} + M) + D. \quad (2)$$

As noted in Appendix B, Equation B2 can be used to convert the water-equivalent flux terms on the right-hand side of Equations 1 and 2 to units of water-equivalent depth (m).

2.2. New Model Components

To satisfy the requirements of a pan-Arctic, Lagrangian, snow-evolution modeling system, the following, previously undocumented, process representations were included in SnowModel/SnowModel-LG. Additional information is provided in Appendices A–H. These appendices include summaries of preexisting SnowModel/SnowModel-LG process representations that are incompletely or inadequately documented elsewhere.

2.2.1. Multilayer Snowpack

The SnowModel/SnowModel-LG multilayer SnowPack-ML submodel was reconfigured so that a new snow layer was created for each snowfall-producing storm, thus mimicking the stratigraphy found in natural snowpacks (each modeled snow layer can be traced to the specific storm that created it). There is essentially no limit to the number of snow layers generated during a model simulation (hundreds are possible). In practice, the user can define the maximum number of layers that are simulated (e.g., a maximum of 25 layers was defined for these pan-Arctic Lagrangian simulations); SnowPack-ML includes an algorithm that merges any relatively thin (e.g., thermodynamically unimportant) layer with the layer below to prevent the layer-limit from being exceeded. The vertical resolution or grid increment of the snowpack can range from as small as ~ 1 mm to as large as few tens of centimeters, depending on the precipitation amount that fell during each storm.

Each snowpack layer has unique physical properties, such as thickness, grain size, thermal conductivity, and density. Because the snowpack layer thicknesses are changing with time, the resolution of the vertical grid is also changing with time. Vertical temperature profiles are simulated using the one-dimensional heat transfer equation described in Appendix C, section C1. Additional information about the snowpack layer structure is provided in Appendix G, section G2.

2.2.2. Blowing Snow

The SnowModel/SnowModel-LG blowing-snow module, SnowTran-3D, will not generally allow blowing-snow simulations using grid increments greater than 500 m. This is because, in most terrestrial systems, snow grains rarely travel this far without being caught in a vegetation or topographic snowdrift trap. Since in our pan-Arctic simulations the parcel sizes, $O(14 \times 14 \text{ km})$; see section 2.3.1), were so large, the only mass budget term calculated by SnowTran-3D was blowing-snow sublimation. In order to calculate blowing-snow sublimation, all the SnowTran-3D horizontal mass-transport fluxes were calculated. But, in the model simulations presented herein, the topography on each parcel is flat. Therefore, all simulated blowing snow was uniform over each grid cell and in equilibrium with the surface and there was no simulated erosion and deposition on the parcels (i.e., the spatial derivatives in Appendix D, Equation D1, are zero). This means that snowdrifts were not simulated, e.g., behind pressure ridges and other topographic ice features because that kind of high-resolution surface topography information for each parcel was not available. In addition, snow dunes were not simulated because the pan-Arctic, multidecade information required to drive the SnowDunes model did not exist.

It is well established that sublimation rates are highest when snow particles are moving rather than at rest. In his pioneering work, Schmidt (1972) suggested that high sublimation rates were achieved during blowing-snow events because of the high snow-particle surface-area to mass ratios and because of the high ventilation rates achieved when snow particles are elevated by wind. He calculated that blowing-snow sublimation rates were two orders of magnitude higher than those from a static snow surface under the same atmospheric conditions (Schmidt, 1982). In terrestrial environments, field observations suggest blowing-snow sublimation can remove the entire snowpack (Liston & Sturm, 2004). For these reasons, in this application, we used SnowTran-3D to calculate horizontal blowing-snow equilibrium transport fluxes

and mass lost from blowing-snow sublimation. Equations describing the horizontal blowing-snow fluxes are described in Appendix D, sections D1–D2.

Some other studies have suggested that blowing snow into leads may also be important in reducing overall snow depth on sea ice (e.g., Déry & Tremblay, 2004; Lecomte et al., 2015; Leonard & Maksym, 2011; Petty et al., 2018; Schröder et al., 2019). With some exceptions (e.g., Leonard & Maksym, 2011), these studies are not based on actual observations (blowing snow into leads was typically used as a tuning parameter to help reduce simulated snow depth, e.g., in Petty et al., 2018). Therefore, the true impact of blowing snow on snow depth across the Arctic Basin is largely unknown. Our field observations and understanding of the physical system suggest very little blowing snow ends up in open leads for the following reasons: (1) During winter, air temperatures are often low enough that leads quickly freeze over (in hours or a couple of days), so the time available to capture blowing snow is relatively short. (2) During a cold storm, blowing-snow deposited in the lead cools the water and speeds lead freeze-up. (3) If the leads/cracks are relatively narrow (meters), then the snow drift trap is small and can fill quickly (in tens of minutes; cf. Liston et al., 2018), soon creating a smooth surface incapable of further accumulation. The turbulent suspended load can also be easily transported over small ice openings (cf., Liston & Sturm, 1998). (4) The mean snow-particle transport distance, or the distance a snow grain can travel before completely sublimating away (e.g., Liston & Sturm, 1998, 2004), is generally on the order of 2–3 km in Arctic environments. Large leads (several 100 meters or wider) are typically 5 km or more apart (Overland et al., 1995), therefore most of the blowing snow is not available to be deposited into a lead. (5) Ice roughness features, such as pressure ridges and other ice-surface elements caused by ice dynamics, can be located near leads, and these surface features capture and hold wind-transported snow and reduce the snow available to be deposited in leads (e.g., Fernández-Méndez et al., 2018; Itkin et al., 2018). (6) Over time, surface-layer snow densities generally increase in response to wind and snow microphysical factors; this higher density snow is more resistant to wind transport and limits the highest transport fluxes to periods when it is snowing (e.g., Liston et al., 2007). (7) Winter field measurements show that even near large open leads 1–5 km wide, the average snow deposition can be proportional to the measured precipitation and precipitation from reanalysis (Graham et al., 2019; Liston et al., 2018); these observations suggest that mass is not being lost from the surface and deposited in the leads. (8) In the marginal ice zone, even in deep winter, the environment is typically wet, and this means the snow-surface shear strength is too great for snow to be transported by naturally occurring winds. For these reasons, snow blowing into leads were not included in this study.

2.2.3. Snow Density

Snow densification in SnowModel/SnowModel-LG occurs under the influence of time, temperature, overburden, wind speed, and the snow density itself. Rain falling on cold snow freezes in the snowpack and increases the snow density of the near-surface snow layers. The density of new snow depends on air temperature, water vapor pressure, and wind speed. In a multilayer snowpack, the density of the surface layer defines the snow's surface shear strength, and that controls the blowing-snow fluxes. These functions are described in Appendix C, sections C4–C8.

2.2.4. Grain-Size Parameterization

Grain growth and degree of faceting is parameterized in a snow-structure submodel following Jordan (1991), where snow grains grow in response to within-snow temperature and vapor pressure gradients and snow density. Wind slabs are simulated in response to the simulated variations in wind speed (Liston et al., 2007). The densest wind slab, and fully developed depth hoar, are assumed to have snow grain diameters of 0.1 to 0.5 mm, and 5.0 mm, respectively (Jordan, 1991; Schmidt, 1982). Grain sizes between these two extremes are simulated in response to the atmospheric forcing and within-snow temperatures and gradients. The equations describing the grain-growth parameterization are provided in Appendix C, section C2.

2.2.5. Thermal Conductivity

To simulate snow temperatures and energy and mass transfers within the snowpack, a snow thermal conductivity parameterization was implemented that accounts for snow grain size, density, and habit (e.g., wind slab, depth hoar). Building on the grain-growth parameterization described in section 2.2.4, we define the effective thermal conductivity of wind slab, depth hoar, and all snow grain sizes between these two snow extremes (Figure C1), using a linear weighting of equations fit to the wind slab and depth hoar curves in Figures 9 and 10 of Sturm et al. (1997). A discussion and the equations describing this representation are provided in Appendix C, section C3.

2.2.6. Rain-Snow Precipitation

The Dai (2008) rain-snow precipitation phase fraction parameterization is used in SnowModel/SnowModel-LG to calculate a rain-snow fraction from reanalysis water-equivalent precipitation inputs. This function allows the model to account for rain and snow occurring simultaneously at any given time step. Other studies have shown this is an important snow mass-balance consideration in maritime environments (e.g., Pflug et al., 2019). How this parameterization is implemented within SnowModel/SnowModel-LG is summarized in Appendix G, section G1.

2.2.7. Superimposed Ice

Superimposed ice (defined to form when rainfall or snow meltwater percolates downward through the snowpack and refreezes at the snow-ice interface) was simulated and used to define how much end-of-summer snow was carried over to the next simulation year (a simulation year was defined to be 1 August YEAR through 31 July YEAR + 1). In this application, we assumed that if the snowpack became isothermal (at 0°C) and saturated with snow meltwater, any remaining snow would eventually become superimposed ice and would no longer be considered seasonal snow in the simulations. By way of example, snow depths recently collected from the *R/V Araon* in summer showed an average snow depth of 8 cm over the FYI floes surveyed, though much of this was wet, large, granular snow and ice of relatively high density. In the context of our SnowModel-LG simulations, this would become part of the superimposed ice matrix at the end of the simulation year and no longer identified as snow. In contrast, unsaturated snow from the previous year(s) will last through to the following year.

2.2.8. Lagrangian Parcel-Tracking Procedures

To satisfy the requirement of accumulating snow on ice parcels that are moving in response to winds and currents, we implemented several procedures in SnowModel-LG. These included the following: (1) Weekly parcel positions and concentrations (see section 2.3.1) were linearly interpolated to daily values. (2) The 3-hr SnowModel-LG time step used the daily position and concentration data (i.e., the eight time steps in each day all used the same corresponding daily position and concentration data). (3) The atmospheric reanalysis grid cell that was nearest to a parcel position at any given model 3-hr time step was used to define the atmospheric forcing experienced by that parcel; effectively, there is a time series of meteorological forcing that follows each parcel. (4) At every model time step, for every parcel position, the latitude and longitude were calculated and used to define the top-of-the-atmosphere incoming solar radiation following standard MicroMet procedures (Liston & Elder, 2006b). This was combined with MicroMet calculations of cloud fraction to define the solar radiation reaching the parcel's snow surface at each time step. Note that alternatively, observations or reanalyses data sets could be used to prescribe the incoming radiation components. (5) For each parcel, the ice concentration was read at each time step and used to define whether an ice surface existed on which to accumulate snow. Any parcel having an ice concentration $\geq 15\%$ was initialized with zero snow on it, and it accumulated and evolved the snowpack from that time on. If the parcel's ice concentration dropped below 15%, the parcel no longer existed and any snow that was on it in the previous time step was assumed to have been lost to the ocean. In general, the transition from about 70% to below 15% happened quickly (e.g., days) and the exact value of this threshold did not significantly change the simulation results.

2.2.9. Converting From Parcel Data to Gridded Data

At the end of the SnowModel-LG simulations, snow property data for each parcel were gridded to the 25×25 -km EASE grid to simplify plotting and analyses of the results. This grid resolution was chosen because it is the resolution of the initial parcel data set on 1 August of each year (the resolution increases throughout the winter and spring; see section 2.3.1). The gridding used the following procedure (described here for snow depth; the same approach was used for the other snow properties of interest, such as snow density). On each simulation day, parcel locations were used to calculate any overlap (in fractional area of each EASE grid cell) between the parcels and the corresponding 25×25 -km EASE grid cell. This overlapping area-fraction was multiplied by the parcel's ice concentration (under the assumption that the concentration is proportional to the contributing area-fraction) and used to weight the parcel's snow depth contribution to each EASE grid cell. For the case where an EASE grid cell parcel-area coverage was over 100%, because of parcel creation and trajectory artifacts, the snow depth was scaled by the total area-fraction, thus creating an average snow depth for that EASE grid cell. For the case where an EASE grid cell was not 100% ice covered, the resulting snow depth was further scaled to create a grid-cell-average snow depth, thus preserving the snow volume in each grid cell (e.g., a grid cell with 42 cm of snow and a 50% ice concentration would have a grid cell snow depth value of 21 cm).

2.3. Input Data Sets

Two key input data sets were required to perform the Lagrangian snow-evolution simulations: (1) parcel positions and concentrations, and (2) atmospheric forcings of air temperature, relative humidity, wind speed, wind direction, and water-equivalent precipitation.

2.3.1. Lagrangian Parcel Position and Concentration Data

Lagrangian parcel trajectories and concentrations were used to evolve the Arctic snow-on-sea-ice distributions in space and time. Daily ice concentrations (15–100%) from Cavalieri et al. (1996) were used to define whether an ice parcel existed and whether snow could accumulate on that parcel. Lagrangian ice parcel tracks were prescribed using 25-km spatial resolution ice motion vectors from the NSIDC (Tschudi et al., 2019a, 2020).

To create the required parcel concentrations and positions, on 1 August of each year the ice concentration data were used to determine whether a grid cell contained a parcel (concentration values $\geq 15\%$ were required). After 1 August, if significant divergence had occurred in the ice motion field such that no previously existing parcel had its center in a grid cell, a new parcel was created in that grid cell. In this way, the ice motion algorithm creates new ice parcels to be initialized and subsequently tracked. In addition, new parcels can have ice concentrations as low as 15%. So, over time, there can be many more parcels than grid cells in the 25×25 -km EASE grid. Because each ice parcel was advected by the ice motion at its center (i.e., the parcels are neither rotated nor distorted), they can overlap each other. In practice, by the end of each winter, there was an average of 3.1 times as many parcels in the Arctic Basin than there were 25×25 -km ice-covered grid cells. Therefore, on average, each parcel covered approximately one third of a 25×25 -km EASE grid pixel (e.g., $\sqrt{25.0 \text{ km} \times 25.0 \text{ km}/3.1} = 14.2 \text{ km}$), or each parcel represented an area of approximately $14 \times 14 \text{ km}$.

The accuracy of the Lagrangian tracking employed herein depends on the ice motion vector accuracy, which is largely controlled by the spatial resolution of the source imagery (Tschudi et al., 2020). Passive microwave data at 25-km resolution provided daily motions with a root-mean-square (RMS) accuracy of ~ 6 – 7 km day^{-1} . An optimal interpolation scheme was used to take advantage of the spatial correlation of neighboring motion estimates to create gridded fields with uncertainties of 3–4 km day^{-1} . We used the weekly version of the sea ice motion product and linearly interpolated those weekly values to daily values for our SnowModel-LG simulations.

The Lagrangian position errors are influenced by spatial resolution, geolocation, and binning errors for each image pixel (Meier et al., 2000; Tschudi et al., 2020), as well as atmospheric effects and temporal variability of the surface during summer. Filtering techniques reduce these errors and, in many cases, compensating errors reduce the net parcel-location biases. For example, Kwok et al. (1998) compared ice motion estimated from ERS-1 synthetic aperture radar (SAR) and drifting buoy motion to the Lagrangian motion product and found errors of 5 to 12 km day^{-1} . These errors were not necessarily cumulative; annual displacement errors were on the order of 50–100 km. For example, when an ice drift track was matched up with the drifting SHEBA ice camp, a displacement of only 27 km occurred over 293 days (Tschudi et al., 2010), or an average net change of less than 0.1 km day^{-1} .

2.3.2. Reanalysis Atmospheric Forcing

There are several atmospheric reanalysis data products available to the science community for applications such as those presented herein. To test the sensitivity of our simulated snow depths to the reanalysis input data sets, we used data from two state-of-the-art reanalyses: NASA's Modern Era Retrospective-Analysis for Research and Applications, Version 2 (MERRA-2; Gelaro et al., 2017), and the European Centre for Medium-Range Weather Forecasts (ECMWF) ReAnalysis, 5th Generation (ERA5; Hersbach et al., 2020). The use of two reanalyses is essential to better understand the uncertainty in the precipitation and air temperatures associated with using different atmospheric forcing conditions. Both reanalyses include hourly data from 1980 through present. The MERRA-2 analysis is performed on a 0.66° longitude by 0.50° latitude ($\sim 56 \text{ km}$) grid, and ERA5 is run on a 0.28125° ($\sim 31 \text{ km}$) Gaussian grid. Hourly data (i.e., air temperature, relative humidity, wind speed and direction, and water-equivalent precipitation) from these reanalyses were aggregated to 3-hourly values and provided to SnowModel-LG using standard MicroMet-SnowModel procedures.

Previous Arctic studies of reanalyses products have revealed no one reanalysis consistently outperforms another (e.g., Hurley, 2014; Rapaic et al., 2015; Serreze et al., 2005). Comparisons of ERA-Interim (ERA-I,

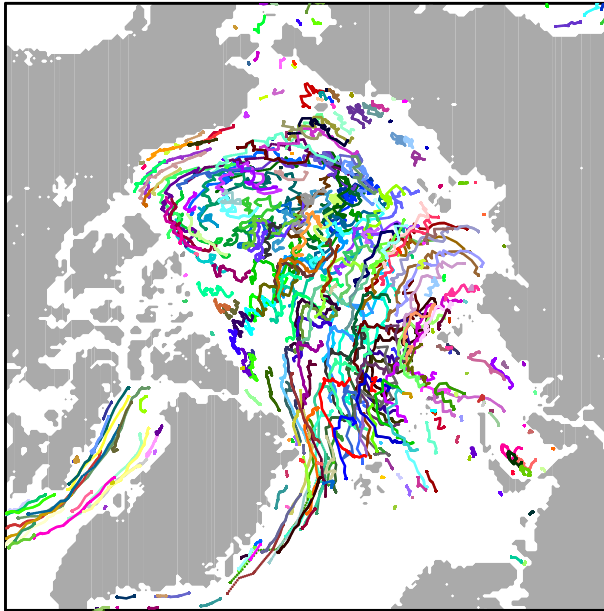


Figure 1. Example parcel trajectories used in the Lagrangian simulations (2013–2014); each color represents a different parcel, every 150th parcel is plotted. Average parcel size was 14×14 km.

tions were performed, one with MERRA-2 and one with ERA5 atmospheric forcings. The snow depth initial condition on 1 August 1980 was assumed to be zero (in the analyses that follow we will show that 1 August is a reasonable start date for the snow accumulation season). The simulation kept track of all ice parcels and where they moved throughout the simulation. During a simulation year, there were an average of approximately 61,000 unique ice parcels within the pan-Arctic simulation domain (Figure 1); the exact number of parcels varied each year.

As part of SnowModel/SnowModel-LG simulations, approximately 150 spatially distributed, time evolving variables are updated at each time step. Daily output from the model runs include all the variables in Equations 1 and 2, and a collection of other meteorological inputs, surface energy balance components, and parameter distributions that control processes like snow density evolution and melt rates.

In addition to the two main SnowModel-LG simulations (one with MERRA-2 and one with ERA5 atmospheric forcing), two additional simulations were performed (again, one using MERRA-2 and one using ERA5) where the ice parcels were not allowed to move. Here the ice extent was prescribed to match that defined by the ice parcel distribution at each time step, with 100% concentration. The snow accumulated and evolved on that stationary ice over the simulation period (so the ice extent changed over time, but the ice itself did not move anywhere). The goal was to compare these with the ice motion simulations to identify the role of ice dynamics (ice motion) in controlling the snow distributions, and to do this at higher resolutions than have been previously considered. These extra simulations are referred to herein as “no motion” (or NoMo) simulations.

To simplify our comparisons with other gridded data sets, after the SnowModel-LG simulations were complete, parcel snow depths, and other properties like snow density, were gridded to the 25×25 -km grid-increment EASE grid following the procedures outlined in section 2.2.9.

Key goals of this project were to (1) understand the contributions of each mass-balance term in Equations 1 and 2 during the snow accumulation season; and (2) to understand the role of the two reanalyses in controlling the spatial patterns associated with their atmospheric forcing conditions. Because of our focus on spatial patterns, we were interested in removing the relative precipitation-magnitude differences between the two reanalyses. To do that we performed the precipitation bias correction procedure described in section 2.5.

the previous ECMWF reanalysis; Dee et al., 2011) and MERRA-2 precipitation, with gauge-measured precipitation from Russian North Pole drifting stations, showed that the signs and magnitudes of reanalysis precipitation biases depend on how gauge corrections are applied. Based on gauge-corrected precipitation from Yang (1999), MERRA-2 precipitation was too high and ERA-I precipitation was too low. Based on gauge-corrected precipitation from Bogdanova et al. (2002), both MERRA-2 and ERA-I precipitation were too high. MERRA-2 showed considerably more precipitation over the eastern Arctic than ERA-I and averaged 90 mm more annual precipitation over the entire Arctic Ocean (Barrett et al., 2020). Wang et al. (2019) showed that over sea ice, ERA5 had greater precipitation than ERA-I, in all seasons. We present our analyses of the differences between the MERRA-2 and ERA5 cold-season precipitation fields in section 2.5.

In addition to precipitation, the two reanalyses have different air temperatures. ERA-I has an important warm bias compared to other reanalyses (e.g., Lindsay et al., 2014), and a 2015 regional study showed that ERA5 was even warmer than ERA-I (Graham et al., 2019).

2.4. Model Configuration

Our SnowModel-LG simulations spanned 38 years, from 1 August 1980 through 31 July 2018. The simulations were run on a 3-hr time step and outputs were saved at the end of each day. Two SnowModel-LG simula-

Table 1

Precipitation Scaling Factors Obtained From Assimilating NASA Operation IceBridge (OIB) Snow Depth Observations Using SnowModel-LG and SnowAssim

| Year | MERRA-2 | ERA5 |
|---------|---------|------|
| 2009 | 1.23 | 1.52 |
| 2010 | 1.28 | 1.65 |
| 2011 | 1.14 | 1.26 |
| 2012 | 1.39 | 1.53 |
| 2013 | 2.08 | 2.37 |
| 2014 | 1.27 | 1.38 |
| 2015 | 1.14 | 1.39 |
| 2016 | 1.46 | 1.55 |
| Average | 1.37 | 1.58 |

2.5. Precipitation Bias Correction

During the years that we had NASA Operation IceBridge (OIB) data (2009–2016, 8 years), SnowAssim was used to bias correct the annual precipitation inputs so the average modeled snow depth equaled the average observed OIB snow depth each year over the year-specific OIB observation tracks. This assimilation used the OIB waveform fitting QuickLook product (GSFC-NK) described by Kwok et al. (2017) (NSIDC, 2016). See Stroeve et al. (2020) for additional details.

As a first step, all the OIB point measurements were gridded to the 25×25 -km EASE grid by averaging all snow depths that fell within each EASE grid cell. Only grid cells that had at least 50 OIB observations were used. Second, all the OIB-EASE grid cells with valid snow depth values in them were averaged to create a single average OIB snow depth for each

OIB year. Third, EASE-gridded, SnowModel-LG snow depth values on 1 April over the coincident OIB grid cells were averaged for each OIB year. The 1 April date was used for all years because it is close to the middle of the OIB observational days for each year. Our analyses suggest the results are largely insensitive to this choice of date or to using the actual OIB observation dates; this is because the OIB data sets were typically collected within one or two synoptic cycles and therefore any observation date within this period represented the general snow conditions during this time of year.

Our analyses of the two reanalyses precipitation forcing fields suggested that, while MERRA-2 and ERA5 showed similar precipitation-event timing and spatial patterns, often their magnitudes differed. Assuming the difference between modeled and observed average quantities represented the precipitation biases, SnowAssim adjusted (multiplied by a single scalar) the SnowModel-LG precipitation input until the average modeled and average OIB snow depths were equal. These calculations were done for the MERRA-2 and ERA5 model runs, for all the OIB years. The resulting precipitation scaling factors are presented in Table 1.

Table 1 shows the following: (1) ERA5 required larger precipitation scaling factors than MERRA-2 to produce enough precipitation to match the OIB snow depth observations. (2) There is considerable interannual variability in the precipitation scaling factors. (3) The scaling factors vary in a consistent manner between the two reanalyses (they increase and decrease each year in a similar way). (4) Both reanalyses require increases in the precipitation inputs (the scaling factors are all greater than 1.0) to reproduce the observed snow depths using this snow modeling system. (5) The 2013 values appear particularly inconsistent; Kwok et al. (2017) noted that 2009 and 2013 had important anomalies that affected the retrievals of those years and discussed the need to produce a more consistent OIB snow depth record. (6) Under the assumption that the average OIB snow depth is approximately consistent from year to year (except for 2013), the precipitation scaling factor variability points to the fact that precipitation is not the sole factor influencing snow depth (cf., Equations 1 and 2). Any errors in the OIB observations or processing procedures, the ice motion fields, and in the other atmospheric fields (e.g., wind speed, humidity, and temperature) would influence not only the snow sources and sinks, but also the snow density that converted SWE to snow depth.

For the 38-year SnowModel-LG simulations, the 8-year average of these scaling factors (1.37 for MERRA-2 and 1.58 for ERA5; Table 1) were applied across all the parcels, during the entire simulation period (all precipitation inputs were multiplied by these scaling factors). This operation effectively scales the snow depth distributions simulated by SnowModel-LG so the mean snow depths in the MERRA-2 and ERA5 model runs are similar, while preserving the snow depth distribution patterns created by the two atmospheric forcing representations. The averaging also ignores fine-scale spatial differences due to collating the OIB flights to 1 April and errors in the simulated parcel drift. These snow-precipitation biases are similar to other snow studies using station observations and MERRA, MERRA-2, and ERA-I reanalyses. For example, in Arctic Alaska, precipitation scaling factors ranged from 0.6 to 0.9 (Liston & Sturm, 2002) and, in another study, averaged 0.8 (Liston et al., 2016); in Colorado, precipitation scaling factors ranged from 0.4 to 2.4 (Liston et al., 2008); in east-central Greenland, scaling factors varied between 0.8 and 1.8 (Pedersen, 2017); and in the Arctic Basin, precipitation scaling factors were 0.72 and 0.93, depending on the season (Liston et al., 2018).

A caveat about this analysis is that the OIB flights preferentially sampled the region north of Greenland, the Canadian Archipelago, and north-coastal Alaska (cf., Kwok et al., 2017). In addition, ice floes are advected into this region under the influences of winds and currents, so the snow on them does not typically represent the precipitation that fell in that area. Therefore, snow depth differences are the result of biases in precipitation over the entire period of snow accumulation along the ice floe trajectories, not just for the region sampled by OIB. Also, these corrections were imposed under the assumption that the snow densities produced by SnowModel-LG were realistic. Differences in the simulated snow densities will have a direct impact on the calculated precipitation scaling factors. Certainly, the snow depth differences between SnowModel-LG and OIB do not necessarily reflect true precipitation biases for other months (like springtime), in other Arctic regions, and throughout the 38-year simulation period. The data required to perform such an analysis do not exist, and our goal is not to assess the quality of the different reanalyses; that has been done elsewhere (e.g., Barrett et al., 2020; Boisvert et al., 2018). This approach fulfills our general objective of creating snow-output data sets from the two reanalysis forcings that (1) are tied in some way to snow observations, (2) have similar mean values, and (3) preserve the spatial patterns associated with the forcing fields.

3. Results

We begin our analyses of the SnowModel-LG simulations by looking at plots of each mass-balance term listed in Equation 1. Figure 2 displays each term on 1 April 2014. This date was chosen solely because this OIB observation year covered the most area with its flight lines. Late-winter snow property distributions are similar for the other 37 years (Stroeve et al., 2020); the details are different, but the general conclusions are the same as those revealed by looking at the 1 April 2014 data. Domain-average quantities from the Figure 2 panels are provided in Table 2. In the Figure 2 panel labels, and the discussions that follow, “NoMo” refers to the no-motion simulation, and “LG” refers to the Lagrangian simulation. For the NoMo case, because there were never any ice (and snow) exported and lost to areas like Fram Strait, and there were no new ice parcels created during the year (and therefore there were no young parcels that would typically have less snow on them at a later date), the 1 April 2014 mass balance contributions were greater than in the LG case. To make the Figure 2 panels more visually comparable, all the NoMo mass balance panels were scaled (multiplied by) the ratio of the 1 April 2014 domain-average LG SWE to that of the NoMo SWE (MERRA-2: 6.8 cm/10.9 cm = 0.62, a 38% reduction).

Figure 2a displays the rainfall contribution to the 1 April 2014 SWE distribution. In SnowModel/SnowModel-LG, rain falling on a cold snowpack will freeze within the cold layer and add to the SWE content. This contribution was largely confined to the coastal areas, and early in the snow accumulation season where and when it was relatively warm. The rainfall mass balance contribution over the entire domain was relatively small, and the NoMo and LG simulations were nearly identical.

Figure 2b presents the water-equivalent snowfall contribution to the 1 April 2014 SWE distribution. Arctic-wide snowfall was the dominant contributor to the snowpack. The spatial patterns displayed in Figure 2b reflect the synoptic-scale precipitation patterns contained within the reanalysis forcing. In addition, in the LG panel there are finer-scale features associated with ice parcels appearing, moving, and disappearing over the simulation period.

Figure 2c shows that static-surface sublimation makes a minimal contribution to snowpack loss during winter. These quantities also include vapor deposition on the snow surface (negative sublimation). The displayed patterns correspond to the synoptic-scale wind patterns during winter, and the NoMo and LG distributions are similar.

Figure 2d quantifies the blowing-snow sublimation that removed mass from the snowpack. The blowing-snow sublimation patterns reflect the synoptic-scale wind patterns for speeds high enough to transport snow (cf., Liston & Sturm, 1998).

Figure 2e displays meltwater losses from the snowpack. This represents snowmelt that has drained from the snowpack; it does not include meltwater that has refrozen within the snowpack. The patterns and magnitudes are similar to the rainfall contributions shown in Figure 2a and reflect the location and timing of relatively warm-related processes.

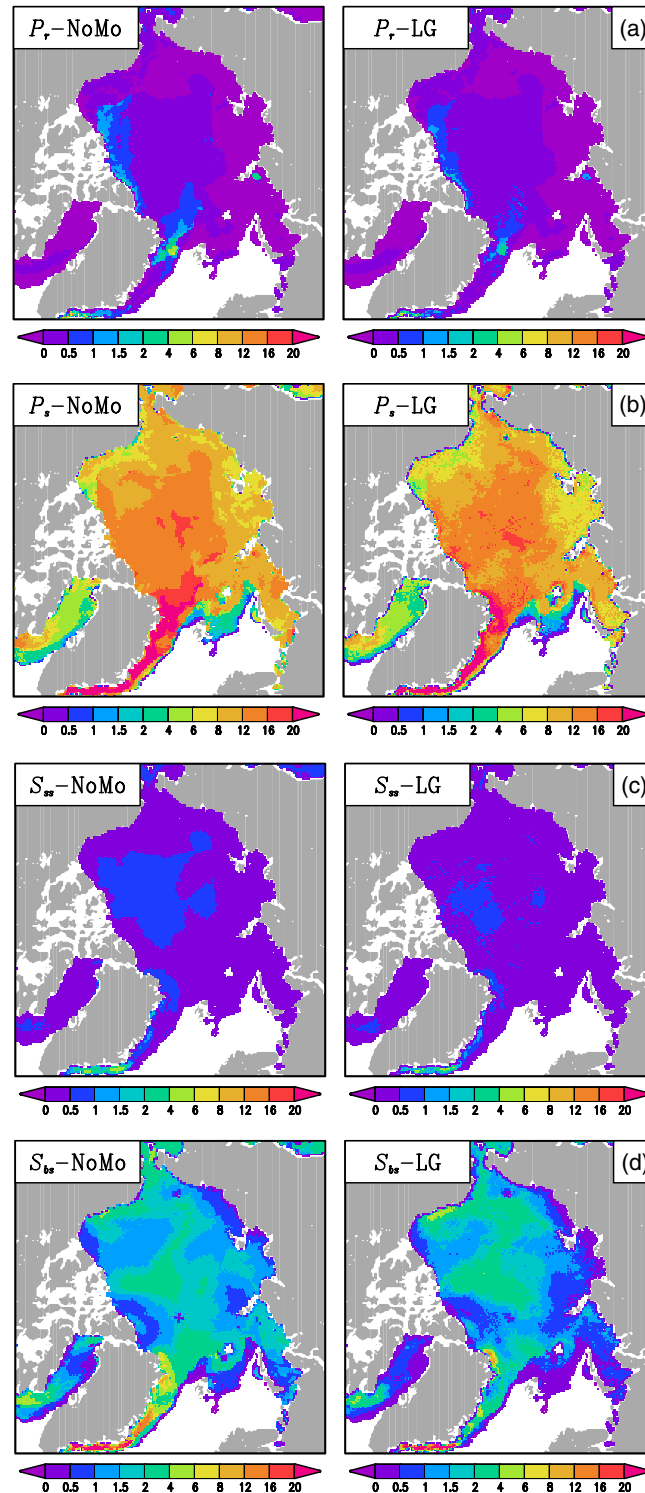


Figure 2a. MERRA-2 SnowModel-LG simulation outputs on 1 April 2014 (color shades; cm water-equivalent). Figure panel pairs (a)–(g) highlight each component of the snowpack mass budget given by Equation 1, where the term in the budget equation is listed in the upper left corner of each panel. In addition, these panels quantify the role of ice motion on the snowpack evolution; shown are two simulations, one with no ice motion (denoted NoMo), and one with Lagrangian ice motion (denoted LG). (a) Rainfall, (b) snowfall, (c) static-surface sublimation, (d) blowing-snow sublimation, (e) snowmelt, (f) ice dynamics, and (g) snow-water-equivalent (SWE) depth. The NoMo panels were scaled to be visually compatible with the LG panels (see section 3). Except for (f), the color bar increments are not linear; the increments were chosen to optimize visibility of the spatial structures and patterns displayed in the plots.

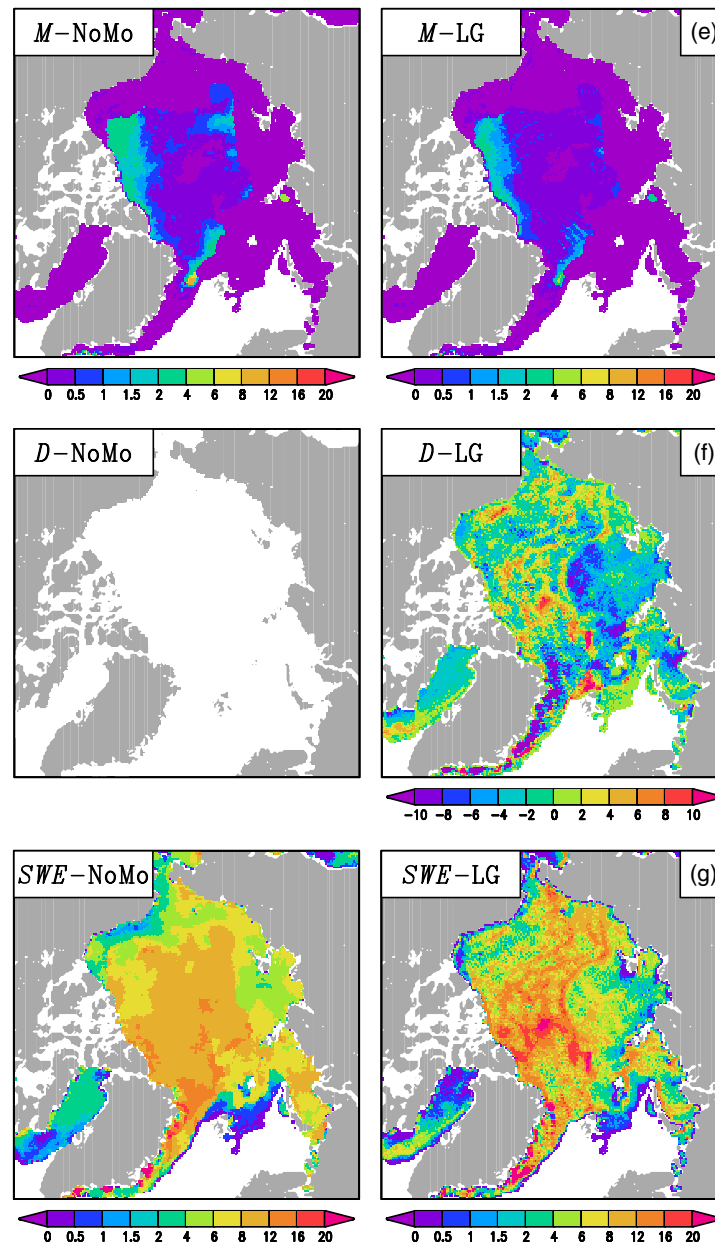


Figure 2b. (continued)

Figure 2f quantifies the ice dynamics contribution to the snowpack mass balance; this distribution was obtained by gridding all the other terms in Equation 1 and defining D to be the residual. By definition, there was no dynamics contribution in the NoMo case. For the LG case, ice motion created spatial variability at length scales much smaller than the synoptic-scale patterns found in the other Figure 2 panels.

Figure 2g presents the SWE distribution resulting from all the contributions to the mass balance. Figure 2 suggests the main contributors to the late-winter, LG SWE distribution are snowfall, blowing-snow sublimation, and ice dynamics. It is also clear that the ice dynamics contribution transforms what is basically a NoMo simulation into a much more spatially complex snow distribution (compare Figures 2b, 2d, 2f, and 2g).

Figure 3 displays the additional terms provided in Equation 2 that convert SWE, in Equation 1, to snow depth. Figure 3a presents the snow density distribution on 1 April 2014. Domain-average quantities from the Figure 3 panels are provided in Table 2. The domain-average snow density in Figure 3a-NoMo and

Table 2

Domain-Average Quantities of the Variables in Figures 2, 3, and 4 on 1 April 2014, With MERRA-2 and ERA5 Atmospheric Forcing, and for the SnowModel-LG No-Motion (NoMo) and Lagrangian (LG) simulations

| Variable | Equation number(s) (#), and variable | Units | MERRA-2 | | ERA5 | |
|----------------------------|--------------------------------------|--------------------|---------|------|------|------|
| | | | NoMo | LG | NoMo | LG |
| Rainfall | (1) (2), P_r | cm SWE | 0.2 | 0.1 | 0.3 | 0.2 |
| Snowfall | (1) (2), P_s | cm SWE | 10.8 | 10.1 | 11.2 | 10.3 |
| Static-surface sublimation | (1) (2), S_{ss} | cm SWE | 0.4 | 0.3 | 0.3 | 0.3 |
| Blowing-snow sublimation | (1) (2), S_{bs} | cm SWE | 3.6 | 1.5 | 3.8 | 1.5 |
| Snowmelt runoff | (1) (2), M | cm SWE | 0.3 | 0.2 | 0.6 | 0.4 |
| Ice dynamics | (1) (2), D | cm SWE | - | -1.5 | - | -1.5 |
| SWE depth | (1), SWE | cm SWE | 6.8 | 6.8 | 6.7 | 6.7 |
| Snow density | (2), ρ_s | kg m ⁻³ | 336 | 322 | 325 | 311 |
| Snow depth | (2), h_s | cm | 19.0 | 19.7 | 19.5 | 20.5 |

Note. Included are all the mass-balance variables (SWE = snow-water-equivalent) in Equation 1, and those in Equation 2 required to convert from SWE to snow depth. Appendix B, Equation B2, was also used to convert the mass flux variables to depth units. While Equation 2 is satisfied at every point in the domain, this may not be true for these domain-averaged values, because the SWE average includes zero values, while the snow density at a point is undefined if the SWE is zero.

Figure 3a-LG are 336 and 322 kg m⁻³, respectively. The NoMo and LG distributions are quite similar, with fine-scale variations due to ice dynamics superimposed on synoptic-scale patterns. Figure 3b presents the associated snow depth distribution; the domain-average snow depth in Figure 3b-LG is 20 cm. Like the Figure 2g SWE distribution, the snow depth distribution includes spatial structures associated with both synoptic-scale and ice-dynamic-scale contributions.

To supplement the results shown for MERRA-2 in Figure 2, we show the snow depth created by the ERA5 atmospheric forcing in Figure 4. The domain-average snow depth in Figure 4-LG is 21 cm and the associated domain-average snow density is 311 kg m⁻³ (Table 2). Like Figure 2, the Figure 4 NoMo panel was scaled (multiplied by) the ratio of the 1 April 2014 domain-average LG SWE to that of the NoMo SWE (ERA5: 6.7 cm/10.8 cm = 0.62, a 38% reduction). The patterns (and magnitudes) are similar to those in Figure 3b, but they differ in detail associated with the differences in atmospheric forcing (primarily precipitation patterns; not shown) between the two reanalyses. In general, the spatial patterns displayed by the ERA5 simulations, for all the simulated variables, are similar to the MERRA-2 simulations displayed in Figures 2 and 3.

4. Discussion

These SnowModel-LG simulations are validated against snow depth and snow density field observations in Part II of this paper (Stroeve et al., 2020). Part II also compares the model outputs with other Arctic snow-related data sets, including those from other OIB data sets, passive microwave products, and two climatologies, and analyzes the long-term trends in the simulated snow properties. The discussion below focuses on the roles of different physical processes that influence the overall snow depth and density distributions.

4.1. Snow Density

Snow densities simulated by SnowModel-LG ranged from approximately 150 to 450 kg m⁻³ during winter and reached 550 kg m⁻³ during summer. The 1 April 2014 snow densities displayed in Figure 3a-LG using MERRA-2 forcing averaged 322 kg m⁻³, and the same distribution for the ERA5 simulation averaged 311 kg m⁻³ (not shown). These are similar to density measurements collected across the Arctic (see Stroeve et al., 2020).

4.2. Blowing-Snow Sublimation

A key suggestion from the analysis of Figure 2d was that blowing-snow sublimation is an important contribution to the snowpack mass budget. To confirm that this might be true, Figure 5 plots the average MERRA-2 wind speed for the period 1 August 2013 to 1 April 2014. Most of the ice-covered simulation domain has average wind speeds greater than that typically sufficient to transport snow (>5 m s⁻¹; Liston & Sturm, 1998) for 8 months of the year. Blowing-snow sublimation fluxes depend on other factors in

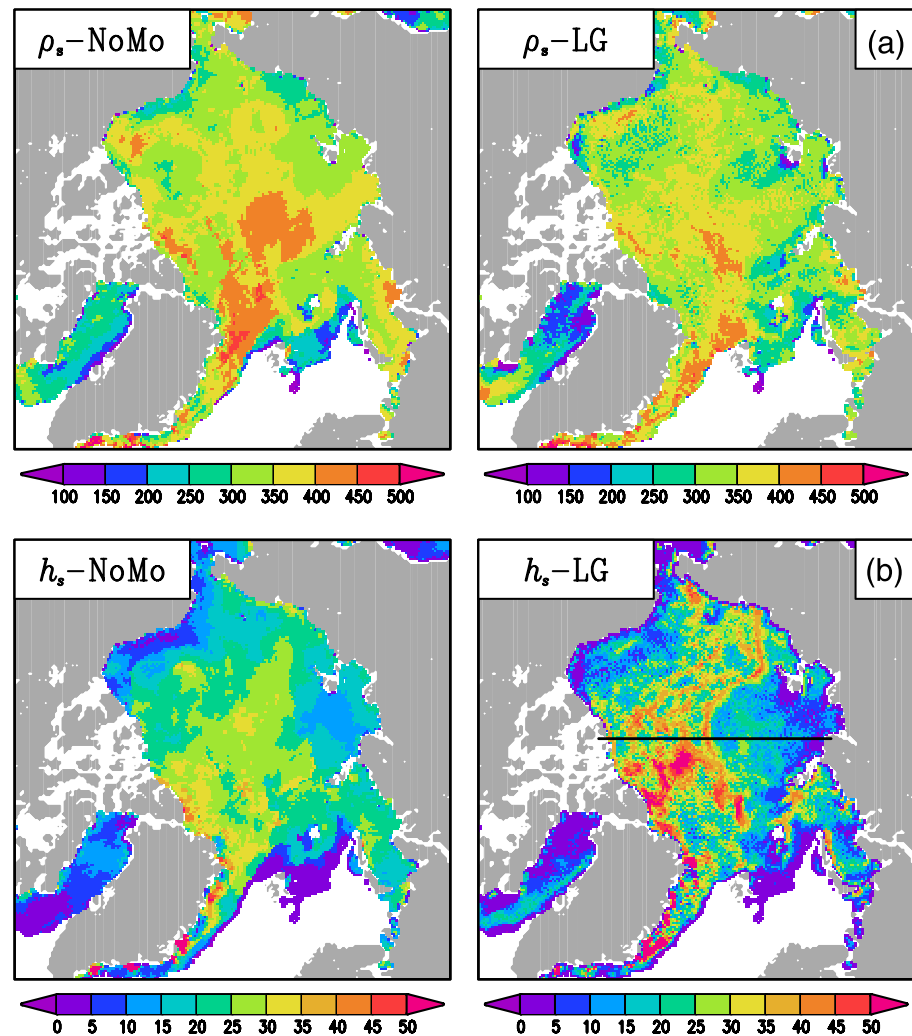


Figure 3. MERRA-2 SnowModel-LG simulation outputs on 1 April 2014. Panels (a) and (b) display the conversion from snow-water-equivalent (SWE) depth in Equation 1 to snow depth and density given by Equation 2. Shown are two simulations, one with no ice motion (denoted NoMo), and one with Lagrangian ice motion (denoted LG). (a) Snow density (kg m^{-3}), and (b) snow depth (cm). NoMo panel (b) was scaled to be visually compatible with LG panel (b) (see section 3).

addition to wind speed, such as humidity deficit and air temperature; these are accounted for in SnowTran-3D's blowing-snow sublimation module (Liston & Sturm, 1998). Throughout large areas of the Central Arctic, blowing-snow sublimation losses were 2–4 cm SWE (Figure 2d), compared to the 8–12 cm SWE depth on 1 April 2014 (Figure 2g). Therefore, more than 20% of the water-equivalent snowfall sublimated during blowing-snow events.

4.3. Ice-Parcel Age

Conceptually, our understanding of snow accumulation processes in virtually any environment suggests that the longer any point can accumulate snow, the more snow that point is likely to accumulate. Figure 6a displays the 1 April 2014 ice-parcel age (in days). We tested the relationship between parcel age and snow depth (Figure 3b-LG) in Figure 6b, yielding an r^2 value of 0.70. This finding suggests that an accurate representation of snow depth evolution on sea ice requires a realistic matching of parcel age with the atmospheric forcing that is building the snowpack. Therefore, since snow accumulation in this environment is governed by synoptic-scale precipitation events, parcel age needs to be provided at a similar temporal scale

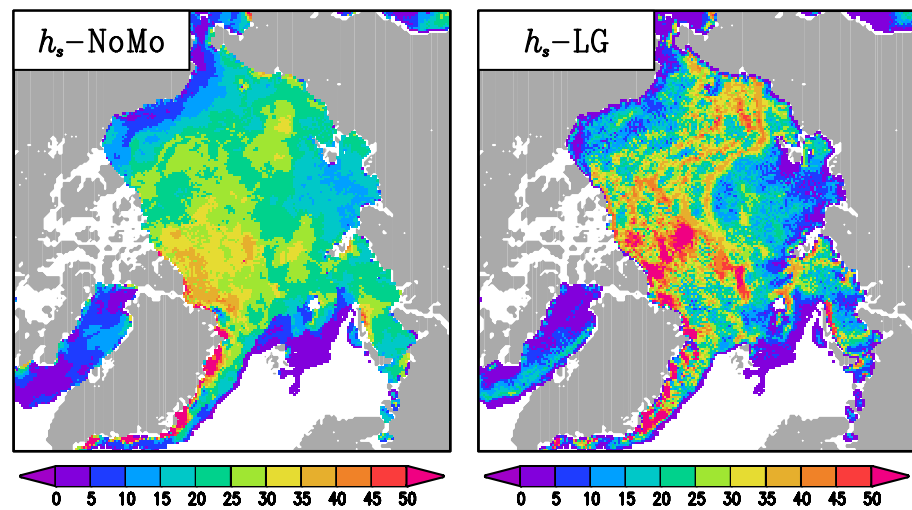


Figure 4. Same as Figure 3b but for ERA5, showing the snow depth (cm) given by Equation 2. Shown are two simulations, one with no ice motion (denoted NoMo), and one with Lagrangian ice motion (denoted LG). The NoMo panel was scaled to be visually compatible with the LG panel (see section 3).

(i.e., approximately weekly). This means that it is not sufficient to just know whether a parcel is FYI, we also must know how old (in days or weeks) the FYI is.

A second conceptual understanding of this environment is that ice-parcel age is directly related to ice dynamics. Divergence of the ice-motion field creates open water that freezes and creates new parcels of younger age than the surrounding parcels. These younger parcels begin to accumulate snow on them in response to subsequent storms, and they also must typically have less snow on them than adjacent, older parcels. These ideas must be true for largely continuous ice-covered regions during winter, where the ice-drift errors are small, the atmosphere is well-below freezing, and strong divergence will create new ice parcels. To eliminate marginal-ice-zone processes from our analyses, we created a mask that removed these regions and isolated the interior of the Arctic Basin (Figure 7a). Then we tested the relationship between parcel age over that masked region (Figure 7a) and the ice dynamics from Figure 2f-LG (with the Figure 7a mask applied). The result was Figure 7b, which produced an r^2 value of 0.72 for the linear relationship between parcel age and ice dynamics.

Because ice age appeared to so strongly control snow evolution, we sought to create a display that would quantify the snow depth contribution from ice parcels that were present on 1 August 2013 (MYI), and the snow depth contribution from ice parcels that formed after that date (FYI). The result was Figure 8. Together, the FYI and MYI snow depth contributions combine to yield the pan-Arctic snow depth distribution (Figure 3b-LG). Figure 8 also shows the regional contributions of these two ice types, with the MYI occupying roughly the left half of Figure 8a. Furthermore, the intrusions of FYI in the area dominated by MYI explain the high spatial snow depth variability in that same area. To validate the MYI extent displayed in Figure 8a, we have included MYI extent boundaries provided by NSIDC ice age (Tschudi et al., 2019b) and European Organization for the Exploitation of Meteorological Satellites (EUMETSAT) Ocean and Sea Ice-Satellite Application Facility (OSI-SAF) ice-type

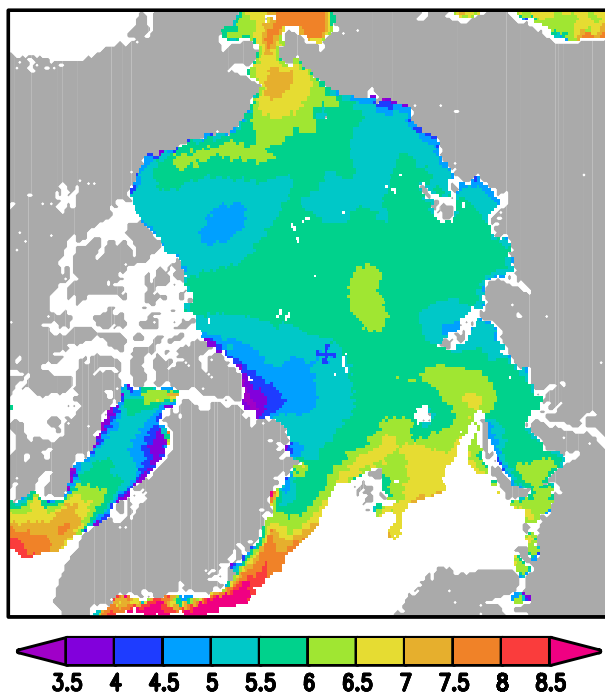


Figure 5. Average (1 August 2013 to 1 April 2014) 10-m height wind speed (m s^{-1}) for the MERRA-2 forced simulation. This figure corresponds to, and identifies the wind forcing associated with, the blowing-snow sublimation quantities presented in Figure 2d. Over much of the domain the average winter wind speeds are sufficient ($>5 \text{ m s}^{-1}$) to transport snow, hence the relatively strong influence of blowing-snow sublimation on the snowpack mass budget.

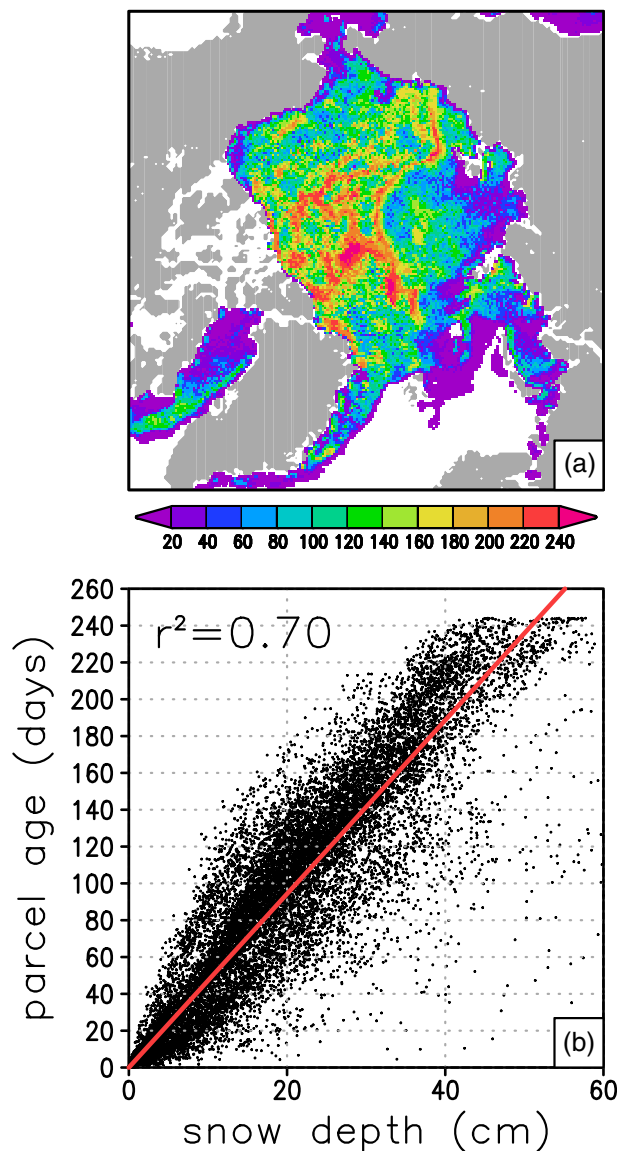


Figure 6. MERRA-2 simulation results on 1 April 2014. (a) Parcel age (days). (b) The relationship between parcel age (days) (from panel (a)) and snow depth (cm) (from Figure 3b-LG). Parcel (or ice) age is a first-order control on snow depth.

(Aaboe et al., 2018) products. Our oldest parcels are roughly contained within the MYI boundaries defined by both products. All three of these representations include MYI throughout the western Arctic and in the East Siberian Sea.

Within SnowModel/SnowModel-LG (and the natural system), the interactions and feedbacks between snow density evolution and the snow depth and snow density itself mean that younger, thinner snow has different snow properties than deep snow. For example, deeper, older snow has higher densities, and higher densities mean the snow strength is higher and more resistant to wind transport (e.g., Liston et al., 2007), and this, in turn, impacts snowpack temperature (through the conduction term in the surface energy budget), wind-slab production, and blowing-snow sublimation.

4.4. Superimposed Ice and Multiyear Snow

Superimposed ice forms by refreezing snow meltwater and, despite its meteoric composition, is regarded as part of the sea ice and not snow (Granskog et al., 2004). Significant amounts of such ice have been found in the Baltic Sea (averaging 20–35% of the total ice thickness; Granskog et al., 2004) and Antarctica (4–12 cm; Haas et al., 2001). Until now, quantifying the volume of superimposed ice in the pan-Arctic sea-ice system, and the amount of snow from the previous accumulation year that lasts into the next year (i.e., multiyear snow), has been elusive. These simulations produced data sets that can address these questions, and they suggest four things: (1) the amount of superimposed ice is minimal; (2) the volume of superimposed ice has been decreasing for the last four decades; (3) snow carryover to the next accumulation season is minimal; and (4) superimposed ice, and snow carryover to the next year, are sensitive to the melt-season atmospheric forcing (primarily air temperature).

Figure 9a displays the superimposed ice volume on 1 August for 1981–2018. The model took any isothermal, melting, water-saturated snow on 31 July, converted it from snow depth to SWE ice using the snow density, and assumed it would either melt or be turned into superimposed ice, depending on the subsequent atmospheric forcing. This snow was no longer considered part of the seasonal snowpack and did not contribute snow to the next snow accumulation season. This definition of superimposed ice does not include the ice formed in refrozen melt ponds that may be important in some sea ice environments. To help conceptualize what the superimposed ice-volume values in Figure 9a mean,

we numerically spread those volumes uniformly over the sea ice present on 1 August of each year and calculated the average superimposed ice thicknesses. The thicknesses averaged 3.3×10^{-5} and 2.3×10^{-6} mm of superimposed ice, for MERRA-2 and ERA5, respectively; this is very little superimposed ice. Figure 9a shows that MERRA-2 superimposed ice values were generally decreasing throughout the simulation period, and that the MERRA-2 values average approximately 19 times those of ERA5.

Figure 9b shows the pan-Arctic seasonal snow that was carried over from the summer to the beginning of the next snow accumulation season (this is remaining snow that was not converted to superimposed ice shown in Figure 9a). Four things are highlighted in Figure 9: (1) this snow is rare (nonzero values only occurred in 1981 and 1989); (2) volumes were insignificant (in 1989 it was the equivalent of 4.9×10^{-6} mm spread uniformly over the available sea ice on 1 August); (3) its presence decreased over the last four decades; and (4) snow formation differed greatly between the MERRA-2 and ERA5 atmospheric forcing (it is nonexistent in the ERA5 simulation). The lack of snow carryover from 1 year to the next is consistent with Lindsay (1998)

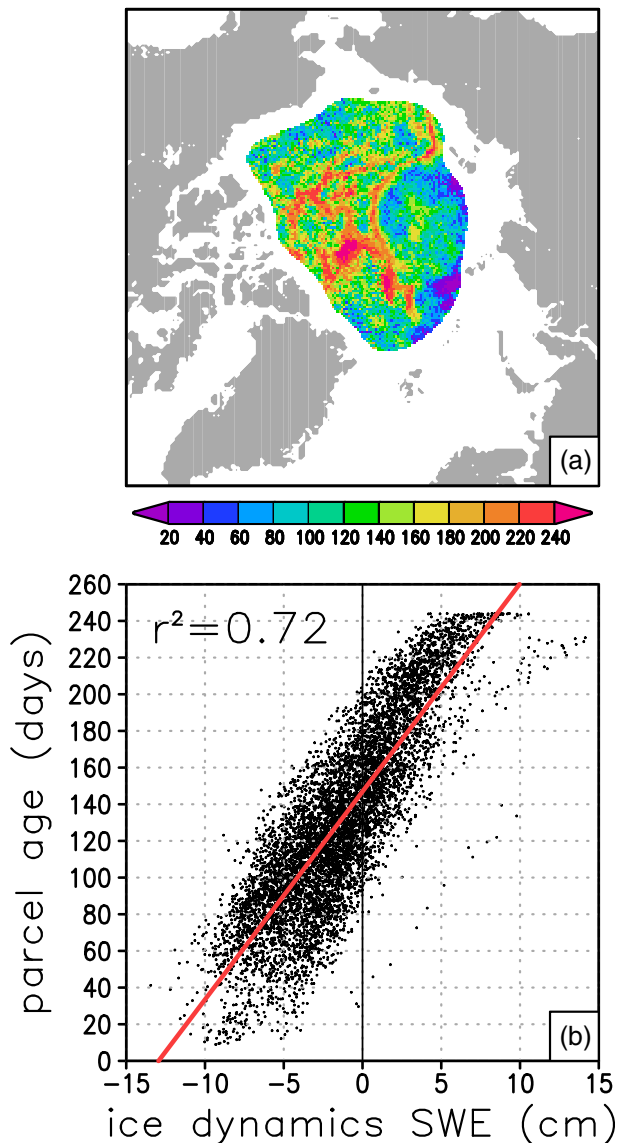


Figure 7. MERRA-2 simulation results on 1 April 2014. (a) Parcel age (days). (b) The relationship between parcel age (days) (from panel (a)) and the ice dynamics contribution to snow-water-equivalent (SWE) depth (cm) (from Figure 2f-LG). Here ice dynamics is D in Equation 1, and it represents SWE changes in response to ice parcels being created and lost through ice motion, including divergence and convergence. To eliminate regions where rainfall and snowmelt play key roles in the snow evolution prior to 1 April 2014, those areas have been removed from the analyses; see the data mask in (a). Parcel (or ice) age is intimately tied to the ice dynamics.

who demonstrated that most of the winter snow melts during summer, and with Warren et al. (1999) who noted that the ice throughout the Arctic is mostly snow-free during August.

To highlight the spatial distribution of superimposed ice and snow depth carryover in Figure 9, the 1 August 1981 values are presented in Figure 10. If the data in Figure 10a are added to those in Figure 10b, the result is the snow depth on 31 July 1981. Our approach of assigning all wet, melting snow to the superimposed ice class has removed most of the snow from the following year's simulation. We do not have any data to show this approach is correct; it is possible that our representation of superimposed ice formation oversimplifies the natural system.

The differences between the MERRA-2 and ERA5 results presented in Figure 9 encouraged further investigation. To assess why almost no superimposed ice and snow carryover was simulated by ERA5, and why MERRA-2 had nonzero values, we plotted the domain-average 2-m air temperature for MERRA-2 and ERA5 during the spring through summer months (Figure 11). This showed that the Arctic-average ERA5 air temperature was approximately 0.7 K higher than MERRA-2 from about 16 June through 16 August (Figure 11), and the time between when the air temperature rose above freezing and dropped back below freezing was 6 weeks and 9 weeks for MERRA-2 and ERA5, respectively (Figure 11). This difference, in general terms, means that the average summer melt period was 3 weeks, or 50%, longer with the ERA5 forcing than the MERRA-2 forcing, and was enough to produce the additional ERA5 melt reflected in Figure 9. Clearly, the melt-period is sensitive to small differences in atmospheric forcing, and this has important consequences for the snow's distribution and seasonal evolution. Graham et al. (2019) found an ERA5 warm bias that was consistent with the ERA-I biases described by Lindsay et al. (2014), and that are consistent with the differences we found between MERRA-2 and ERA5.

In addition, the simulations showed that even though the sea ice extent minimum generally occurs in mid-September (e.g., Cavalieri & Parkinson, 2012) snow can start accumulating on ice parcels at any time when then air temperature is below a couple of degrees above freezing (e.g., Dai, 2008), and Figure 11 suggests this can easily happen in early August (similarly, Liston et al., 2018, found a MYI snowpack began forming on 29 July 2014). The implication of this result is that snow analyses must start their annual snow accumulation cycle in early August to account for early-season snow accumulation on MYI.

These findings, and those from section 4.3 on ice-parcel age, are consistent with Hezel et al. (2012) and Liston et al. (2018) who found that the different snow depths on FYI and MYI were because MYI has a longer snow accumulation period in a given year, not because of snow carryover from 1 year to the next. To account for the impact of ice age on snow accu-

mulation, we must know the age of the FYI (in days or weeks). In addition, because there is minimal carryover of seasonal snow from 1 year to the next, the most significant role of MYI on snow accumulation stems from its presence early in the accumulation season (its existence means it has the longest possible snow accumulation season). It is particularly important to account for ice age late in the summer and early in the fall, because this period is characterized by relatively high precipitation amounts (Boisvert et al., 2018).

4.5. Ice Dynamics

The key role that ice dynamics plays in driving the snow distribution is highlighted in Figures 3b-LG and 4-LG, particularly when compared to the no-motion data in Figures 3b-NoMo and 4-NoMo. The LG figures

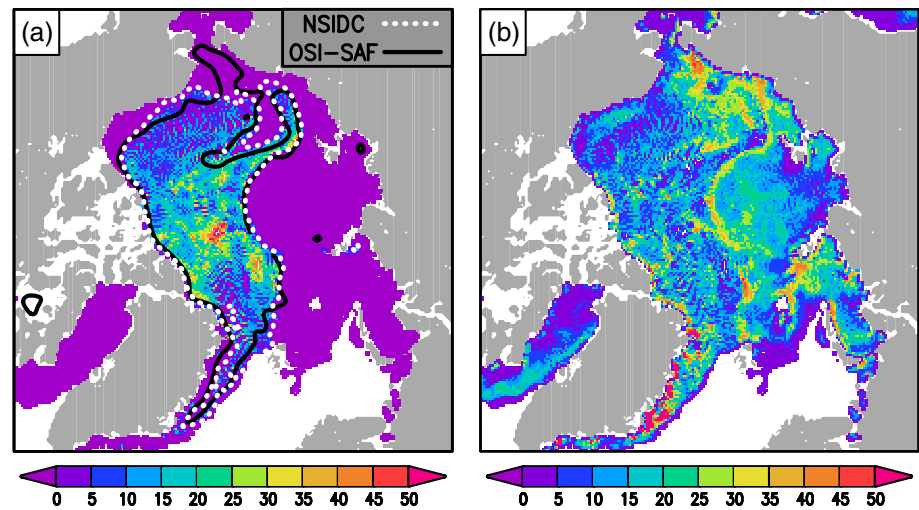


Figure 8. The 1 April 2014 snow depth (cm) distribution contribution from (a) ice parcels that were present on 1 August 2013 and (b) ice parcels that formed between 1 August 2013 and 1 April 2014. The sum of these two panels yields the 1 April 2014 snow distribution plotted in Figure 3b-LG. Panel (a) includes the 1 April 2014 NSIDC and OSI-SAF ice-age extent boundaries that surround the multiyear ice (MYI) in the simulation domain. The OSI-SAF product does not extend beyond 87°N latitude, so their ice-age extent boundary is not plotted above that latitude.

include spatial structures associated with synoptic-scale meteorological forcing (these are also displayed in the NoMo figures) and shorter “regional-scale” spatial structures associated with ice dynamics that can be represented with a 14×14 -km parcel size and 25×25 -km grid (Figure 2f-LG). An important consequence of ice motion is that, when new parcels are formed, they are initiated with zero snow on them (as in the natural system). The divergence that creates a new parcel is not compensated by ice compression and a mechanical thickening of snow depth on adjacent, existing ice; if this occurred, then the thicker snow

would depress the ice below the water line and snow-ice would form. Instead, in the natural system, some snow is lost by flooding and the submerging of ice blocks below the water level in pressure ridges and ice rubble fields. In our simulations, this is simplified by the scaling of converged parcels' variables to 100% area when they are gridded to the 25×25 -km EASE grid (see section 2.2.9). Therefore, both divergence and convergence are snow sinks, where the later only occurs during the gridding process. In general, such groups of converged parcels stay together until they reach the ice edge. Section 3 showed that the Lagrangian simulations had 38% less snow on 1 April 2014, for both MERRA-2 and ERA5, than the “no motion” simulations.

To quantify the general length-scale associated with this regional-scale spatial structure, we plotted the snow depth on 1 April 2014, from the MERRA-2 forced SnowModel-LG simulation (Figure 3b-LG), along the transect identified by the solid black line in Figure 3b-LG (Figure 12a). Figure 12a shows a relatively systematic spatial structure across the entire transect, and Figure 2f-LG suggests this structure is controlled by ice dynamics. We performed a semivariogram analysis over this transect and fit a spherical model through the analysis points following Liston et al. (2018). This yielded a length-scale (half the wavelength) of 130 km (Figure 12b). This is consistent with visually detectable snow depth distribution patterns present throughout the simulation domain (e.g., Figure 3b-LG). Further analyses are required to quantify how this length-scale varies across the Arctic and from one season to the next.

The ice dynamics played three key roles: (1) the parcels were moved to different areas of the Arctic Ocean, so there was an advection of snow to

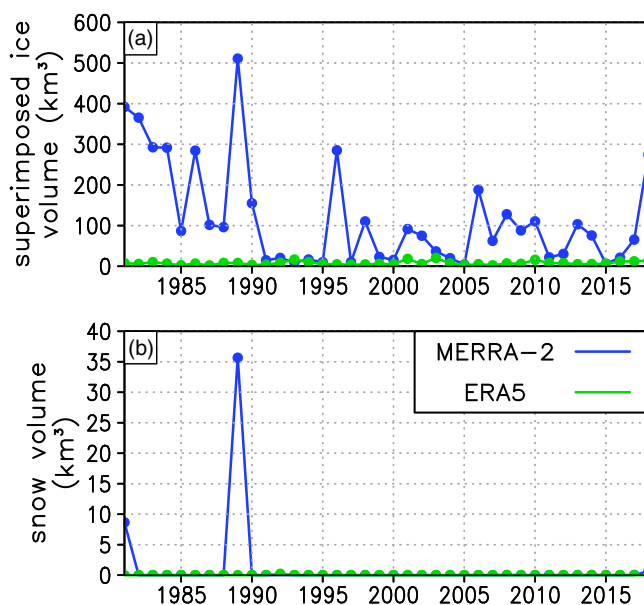


Figure 9. (a) Total volume of superimposed ice on 1 August, 1981–2018, and (b) total snow volume on 1 August, 1981–2018, for the MERRA-2 and ERA5 simulations. The carryover of snow from 1 year to the next is negligible in all years, for both atmospheric forcing data sets. There are significant differences in superimposed ice and snow carryover between the MERRA-2 and ERA5 simulations.

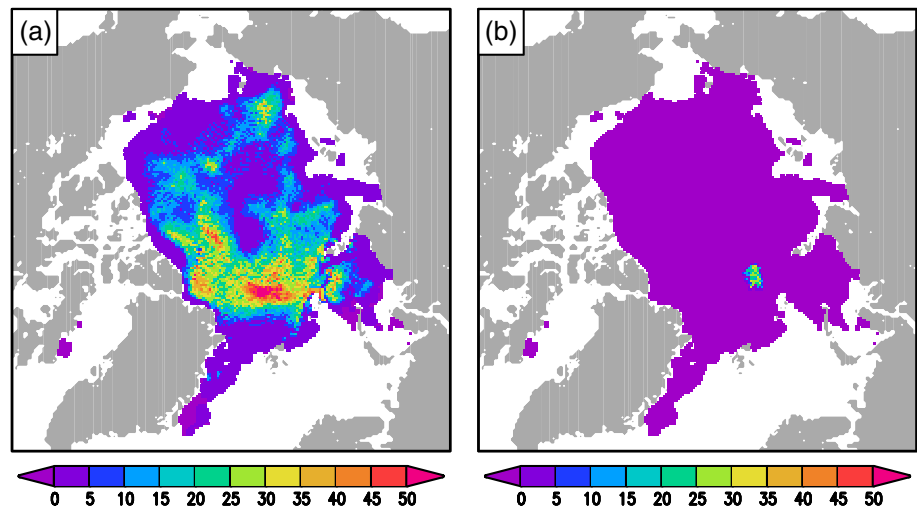


Figure 10. MERRA-2 results on 1 August 1989 (the date of maximum superimposed-ice and snow-depth volumes presented in Figure 9). (a) Superimposed ice distribution (cm) and (b) snow depth distribution (cm).

places with meteorology that is different than the snow stratigraphy and attendant properties might suggest; (2) new parcels of younger age than the surrounding parcels were created, and these newer parcels have less snow on them; and (3) the gridded products lost some snow in convergence zones where the area covered by the parcels exceeds 100%. All three processes lead to relatively high spatial variability in snow properties.

SnowModel-LG initialized new parcels with zero snow depth. Other snow and sea ice modeling efforts have employed artificial procedures that initialize new ice parcels with a mean snow depth from adjacent parcels (e.g., Schröder et al., 2019), or effectively apply smoothing functions in time or space to their distributions, or are run at resolutions too coarse to capture these structures (e.g., Blanchard-Wrigglesworth et al., 2018; Kwok & Cunningham, 2008; Petty et al., 2018). In addition, other numerical approaches such as incremental remapping (e.g., Lipscomb & Hunke, 2004) and Eulerian schemes (e.g., Petty et al., 2018) can include significant numerical diffusion that may also create unrealistically smoothed fields (Quarteroni & Valli, 1994). As an illustration of such diffusion, we compare our SnowModel-LG NoMo outputs (Figure 3b-NoMo) with the Petty et al. (2018) outputs shown in Figure 15a of our Part II paper (Stroeve et al., 2020). Both models use the same atmospheric forcing and produce similar snow depth spatial distributions, but the first has no motion and the second uses a Eulerian scheme.

All these practices produce more-uniform snow property distributions than those produced herein. We see no physical reason to do such smoothing since the natural system does not function in this way. When sea

ice initially forms, there is no snow on it until precipitation or blowing snow deposits it there. As evidenced by the spatial structures displayed in Figures 2f-LG, 6, and 7, initializing new parcels with zero snow depth has an important impact on the simulated snow property distributions. In the future, when similar simulations are performed using higher resolution parcel information (smaller parcels), this approach of initializing new parcels with zero snow depth will be even more physically realistic and appropriate.

Other aspects of our model simulations likely create smoother snow property fields than found in the natural system. A considerable smoothing of the model simulation is already achieved by gridding the Lagrangian parcels to the Eulerian (EASE) grid (see section 2.2.9). In addition, sea ice drift represented by 14×14 -km parcels, gridded to a 25×25 -km resolution grid is too coarse to effectively represent long, narrow features like leads; these seldom have widths larger than a few kilometers. Imagine a scenario where several parallel leads of 1-km width appear in an area

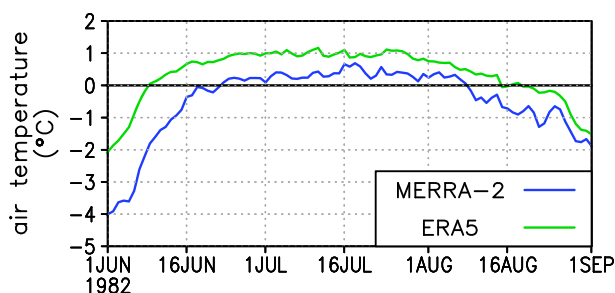


Figure 11. Domain (ice-covered area) averaged 2-m air temperature for the MERRA-2 and ERA5 atmospheric forcing data. The period between when the air temperature rises above freezing, and 1 August, is approximately 2 weeks less for MERRA-2 than ERA5 (5 and 7 weeks, respectively). This generally longer snowmelt period for ERA5 means the superimposed ice and snow on 1 August are significantly less in the ERA5 simulation.

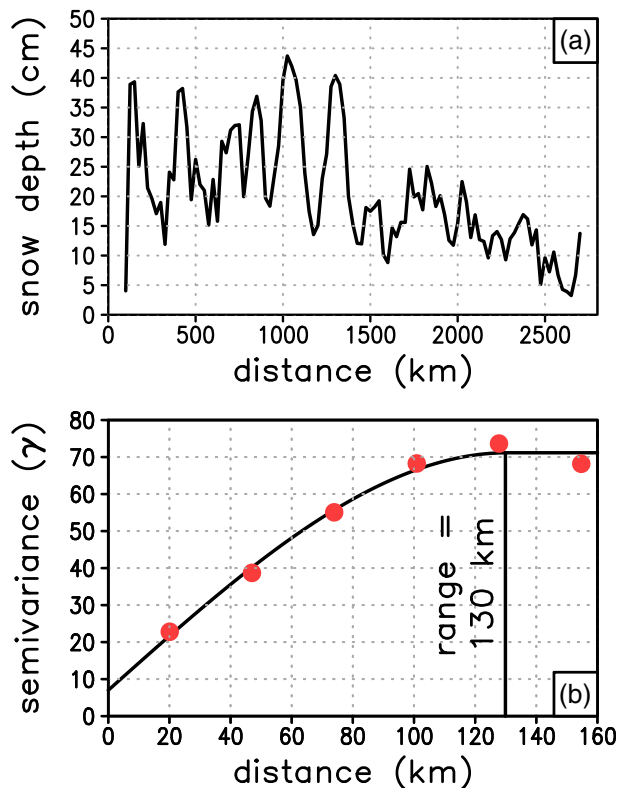


Figure 12. (a) SnowModel-LG simulated snow depth across the horizontal black line plotted in Figure 3b-LG. (b) Semivariogram analysis (solid red dots) of the spatial length scale associated with the snow depth distribution in (a). The black line is a spherical model fit through the analysis points (e.g., Liston et al., 2018). The calculated range, or length scale, of the snow depth distribution features in (a) is 130 km.

that is 100 km wide. The decrease in sea ice concentration caused by sea ice divergence would be sufficient to produce new parcels in our parcel-generation scheme. These parcels will appear in the form of an intermittent line of square parcels, while, in nature, we would expect long, narrow leads. This imprecise representation of ice formation also influences the characteristics of the snow depth evolution.

To help analyze the role of ice motion on producing realistic Arctic snow property distributions, we compared snow depth relative frequency distributions along the 2014 OIB flight lines with the coincident data in Figures 3b-NoMo and 4-NoMo (Figure 13a) and in Figures 3b-LG and 4-LG (Figure 13b). For this comparison, the OIB data were aggregated to a 25×25 -km EASE grid following the procedures described in section 2.2.9. The representation is much improved when ice dynamics are included. At higher resolutions, the redistribution of snow by sea ice motion must also be included to reproduce typical sea ice snow distributions (e.g., Liston et al., 2018). Numerous factors control the snow depth distribution on sea ice, many of which are related to ice dynamics and the associated ice age, and the interactions between ice surface roughness and wind (e.g., Liston et al., 2018). The net effect of these factors is that the distribution becomes wider and fewer values are concentrated around the mean. Unfortunately, the OIB data are not direct observations, but are processed airborne measurements that can (1) have several distinctly different solutions (e.g., Kwok et al., 2017) and (2) include biases over deformed ice (King et al., 2015).

In addition to OIB data, there are very few Arctic winter snow depth data sets that span both the synoptic scale and the 130-km regional scale (Figure 12) captured by our SnowModel-LG simulations. One of the exceptions are data from the European Space Agency's (ESA) April 2017 CryoSat-2 Validation Experiment (CryoVEx) campaign (Haas et al., 2017). Figure 14 presents a comparison of snow depths collected

during CryoVEx 2017 and our simulations. CryoVEx data were collected in a relatively straight line from the Alert airbase on Ellesmere Island in Nunavut, Canada (starting at 83°N latitude), to the northwest, and ended at 87°N latitude. The transects included 10 locations spaced approximately 50 km apart, where between 217 and 2,311 snow depth measurements, spaced 1–3 m apart, were recorded at each location. The most interesting feature of the CryoVEx data for our SnowModel-LG study is that it spanned several different sea-ice dynamics regimes and regional ice types. The southern-most locations were on relatively immobile sea ice areas near the coast (referred to as the “ice bridge” by Haas et al., 2017). Farther north was a “shear zone” characterized by compressed, deformed ice where no measurements were made because the plane could not land (Haas et al., 2017). This was followed by two areas with more leads in the ice pack: first a “MYI area,” and finally “FYI area” closest to the North Pole (Haas et al., 2017).

To help satisfy our goal of comparing ground-based observations with SnowModel-LG simulated regional-scale spatial variability over different sea-ice dynamics regimes, Figure 14a displays the in situ CryoVEx data on top of the SnowModel-LG MERRA-2 data averaged over the time period coincident with the field campaign. The model was able to represent not just the higher snow depths expected in the shear zone, where there was very little young, thin ice, but also the thinner snow north of it, where some measurements sampled snow over refrozen leads. Figure 14a also highlights the complexity of the natural system and the challenges of reproducing these snow- and ice-related spatial structures with a pan-Arctic modeling system.

Figure 14b presents the probability distributions of the observations and SnowModel-LG outputs over the regional measurement transect. The thin ice and older ice distribution modes from the model and observations are similar. Clearly, the measurements also include high-resolution snow depth distribution features (cf., Liston et al., 2018) that are not accounted for in the 25×25 -km gridded simulation data. This is

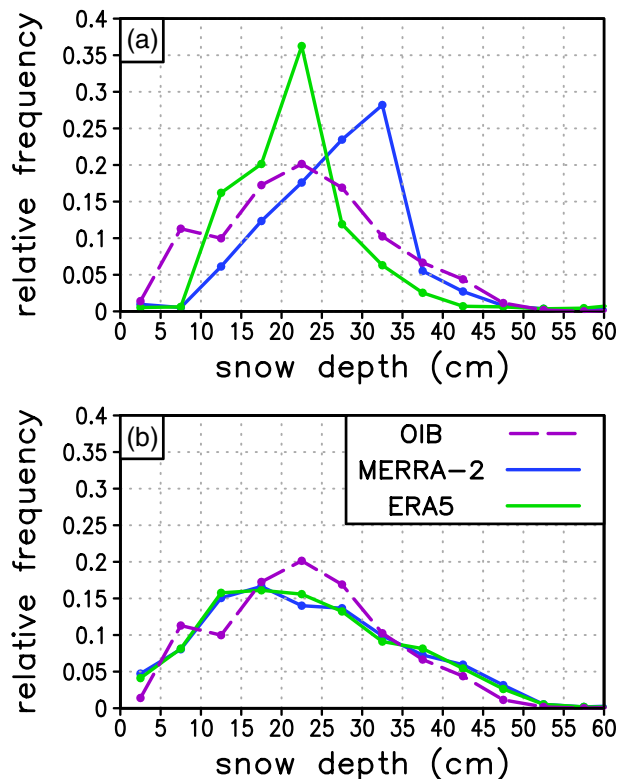


Figure 13. Observed and SnowModel-LG snow depth relative frequency histograms of 5 cm depth bins (0–5, 5–10 cm, etc.; markers sum to 1.0) over the OIB flight lines, gridded to the 25×25 -km EASE grid, on 1 April 2014. (a) With no ice motion (from Figure 3b-NoMo), and (b) with ice motion (from Figure 3b-LG).

highlighted by the “tail” of the CryoVEx distribution curve in Figure 14b; this tail is typical of snow distributions on deformed ice (e.g., snowdrifts behind the pressure ridges and other ice-topography features). This tail does not exist in the course-resolution SnowModel-LG simulations. Although, in Figure 14b, we included all the measurements from the 10 CryoVEx observation sites (in contrast to Haas et al., 2017), the complete suite of natural variability is still not represented. The measurements included the main ice types in the area, but the new ice in leads and deformed ice were undersampled, since most of the measurements were taken across a sequence of level ice floes (Haas et al., 2017).

4.6. Limitations

Many aspects of snow-on-sea-ice are unknown. Throughout this project, we were continually confronted by the lack of accurate, detailed, quantitative information with which to compare our modeled processes and outputs. Often, observations were either nonexistent or inadequate in spatial or temporal scale, or snow variable or property. Moreover, the data sets that do exist (see Stroeve et al., 2020) frequently have such grave deficiencies they are largely without value (e.g., climatologies from over four decades ago, passive microwave data during the summer wet season).

SnowModel/SnowModel-LG is comprehensive and versatile enough to reasonably match available information associated with almost any snow-related environmental variable. It has been designed to merge model representations with observations, to build the most realistic possible depiction of winter snow processes and evolutions. However, in almost every aspect of this project, we lacked sufficient information to gauge our success in accurately representing the natural system. There are too many things about the snow-on-sea-ice environment that we do not know to the required degree of accuracy.

For example, the sea ice community has a strong interest in snow depth on the ice (hence, the study presented herein), but the large uncertainty in water-equivalent precipitation and snow density may have prevented us from accurately quantifying snow depth. When we assimilated OIB snow depths to adjust the reanalysis water-equivalent precipitation inputs, we had to assume that the SnowModel/SnowModel-LG densities were realistic, because there was no information to guide us otherwise. While we do know that the simulated snow densities fit within realistic bounds, actual observed values are nonexistent over the spatial and temporal domains of this study. Without such observational data sets, we were unable to evaluate the accuracy of our corrected water-equivalent precipitation inputs.

In addition to needing improved observations of state variables (e.g., the variables on the left-hand side of Equations 1 and 2, for which the value at the previous time step must be retained for use in the next time step), improved process understanding is also required. For example, this study showed that blowing-snow sublimation may be an important term in the snow mass budget. However, there were no observational data sets available to compare with our simulation results. Blowing-snow sublimation depends on atmospheric inputs like humidity deficit (i.e., how dry the air is), turbulence ventilation functions (i.e., wind speed), and the amount of snow entrained in the airstream (e.g., Liston & Sturm, 1998). So, e.g., if the air is saturated, or if there is no blowing snow because of low wind speeds, there will be no blowing-snow sublimation. These atmospheric forcing inputs have not been independently validated as thoroughly as the more common reanalyses variables such as air temperature and precipitation. Even if the blowing-snow submodel was perfect, we have almost no information about the quality of the required input data sets.

Snow blowing into leads was also identified as a process that the sea ice community does not adequately understand. Field observations of the issues and concerns presented in section 2.2.2 are required to resolve this issue. In addition, model sensitivity simulations could be used to lend insights into when and where

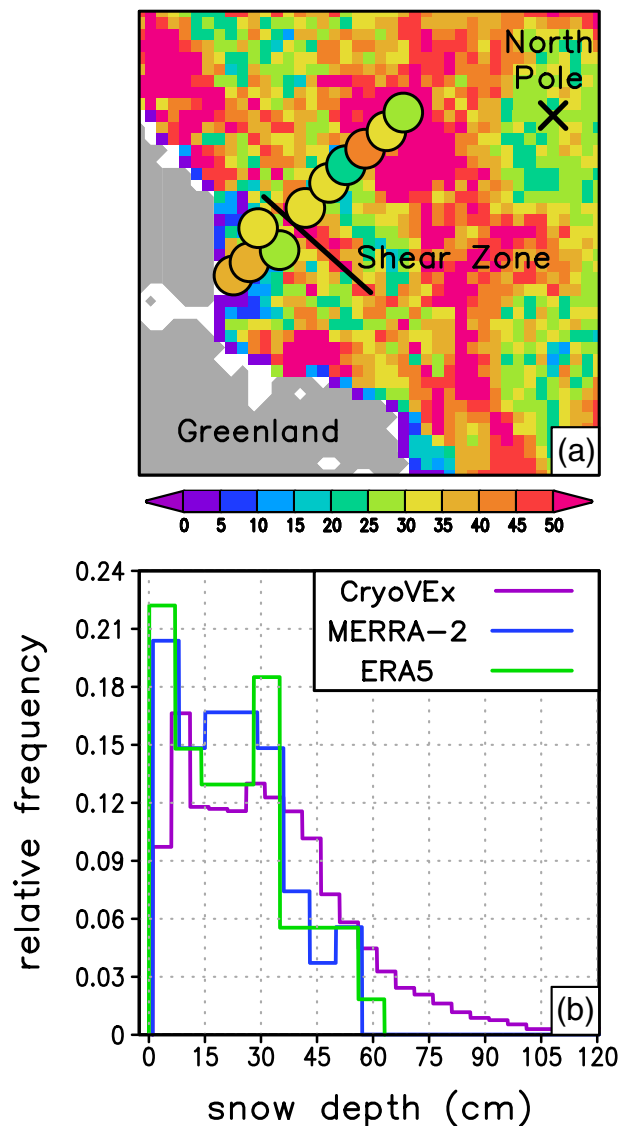


Figure 14. (a) CryoVEx 2017 snow measurement transect (colored circles; Haas et al., 2017) and SnowModel-LG outputs (colored grid cells) for an area north of Greenland. Included is a black line showing the shear zone identified by Haas et al. (2017). The SnowModel-LG data were averaged over the CryoVEx observing period, 11–18 April 2017. The two CryoVEx observation sites that are aligned with the shear zone were separated in the plot to improve clarity. (b) Probability distributions for the CryoVEx observations ($n = 10,901$) and the SnowModel-LG parcels (MERRA-2, $n = 54$; ERA5, $n = 54$) roughly coincident with the CryoVEx circles in (b). The MERRA-2 and ERA5 lines in the histogram were offset by one line-width to prevent overlap.

snow lost to leads is significant. SnowModel-LG could also be run at relatively high-resolution (meters to tens-of-meters) to quantify the role of fetch, lead width, and snow-surface strength properties on the amount of snow blown into the ocean through ice cracks and leads.

Numerous high-resolution, $O(1\text{--}500\text{ m})$, snow features are known to exist in sea ice environments. Snow bedform features and snow trapped in the lee of pressure ridges and around other ice roughness elements are ubiquitous on sea ice. These were not represented in our $14 \times 14\text{-km}$ parcel simulations. The consequences of not including them likely depends on the application.

One of the limiting factors of these SnowModel-LG simulations was the spatial and temporal resolution of the sea ice drift-product inputs. As noted in section 2.2.8, weekly parcel positions and concentrations were linearly interpolated to daily values. Since the distance a typical parcel travels in a week is generally well within the synoptic spatial scale, we do not expect that there was much information lost because of this approach. In the future, higher temporal resolution parcel data will help establish the validity of this method.

This study would also benefit from higher spatial resolution ice motion and ice age data sets. In the natural system, ice dynamics and the associated parcel formation timing and new-parcel sizes certainly occur at higher resolutions than those represented in these simulations. We have shown previously that SnowModel-LG can be run over high-resolution (meters-scale) ice-surface topography to build snowdrifts in the lee of pressure ridges (Liston et al., 2018). The ongoing development of higher resolution sea ice formation, movement, concentration, and ice-surface topography will help advance our understanding of the regional importance of narrow features like leads and ridges for snow distribution on sea ice.

Other possibly important processes were not included in these model runs. For example, snow-ice formation (defined to form when seawater floods and refreezes at the snow-ice interface due to a heavy snow load that submerges the ice surface below sea level) (e.g., Merkouriadi et al., 2017) was not accounted for. This process would remove snow from the system. Accounting for snow-ice formation requires coupling SnowModel-LG to an ice-growth model. Both the processes and features associated with snow-ice have a direct impact on the seasonal snow evolution across the Arctic Basin and both require further study. In addition, summer processes were identified as being particularly sensitive to both atmospheric forcing and model representation. Additional work is required to better understand how summer processes can be best represented in snow-evolution modeling systems.

A modeling system as complex and comprehensive as SnowModel/SnowModel-LG contains numerous parameters that impact solutions

such as those presented herein (see Appendices A–H). However, errors in the model parameters are generally smaller than errors in the currently available atmospheric forcing inputs. As an example, section 2.5 indicated that errors in reanalyses precipitation forcing range from approximately 50% to 200%, and uncertainties in the reanalyses air temperatures (of 1 or 2 K) can effectively half or double the snow-melt season length (see section 4.4). With these atmospheric forcing errors, grain size and thermal conductivity errors are relatively unimportant; these snow properties only directly impact the conduction term in the surface energy balance (conduction is typically a few percent of the energy budget, or less) and these snow properties only indirectly affect the snow temperature and, therefore, the snow density. In addition, as noted above, we do

not have adequate, high-quality, snow observations to compare our model outputs against. For these reasons, we have not performed any parameter sensitivity simulations as part of this SnowModel-LG application.

In addition to the need for more process studies and improved input data sets, there is also likely much to be learned from sea-ice modeling studies that include snow process and snow property representations. For example, those included in the Los Alamos Sea Ice Model (CICE; e.g., Holland & Landrum, 2015; Holland et al., 2012; Hunke et al., 2013; Schröder et al., 2019) and in the Louvain-la-Neuve Sea Ice Model (LIM; e.g., Lecomte et al., 2013, 2015; Rousset et al., 2015).

5. Conclusions

5.1. Simulation Summary

We used a state-of-the-art, parcel-following (Lagrangian), snow-evolution model (SnowModel-LG) to produce daily, pan-Arctic, snow-on-sea-ice, snow property distributions on a 25×25 -km grid, for the period 1 August 1980 through 31 July 2018 (38 years). The model was forced with MERRA-2 and ERA5 atmospheric reanalyses, and NSIDC sea-ice parcel concentration and trajectory data sets (approximately 61,000, 14×14 -km parcels). Eight years (2009–2016) of OIB snow depth data were assimilated prior to running the 38-year simulations. To reproduce the mean OIB snow depth observations, the MERRA-2 and ERA5 precipitation forcings were increased by 37% and 58%, respectively. These adjustments were applied uniformly (in space and time) to the 38-year simulations, thus allowing us to focus on the spatial patterns, instead of the magnitudes, of the snow properties produced by the two reanalyses.

The simulations performed full surface and internal energy balances, and a full mass-balance accounting. A key goal of the project was to understand the contributions of each mass-balance term on the evolution of SWE and snow depth. The following mass balance terms were accounted for and produced the resulting SWE distributions: rainfall, snowfall, sublimation from static-surfaces and blowing-snow, snow melt, and ice dynamics. The SWE data were converted to snow depth using the simulated snow density.

The snow density evolution included a multilayer snowpack representation, where each stratigraphic layer corresponded to a precipitation event. The blowing-snow submodel calculated horizontal blowing-snow equilibrium transport fluxes and the associated wind-related snow densification processes. Other snow density evolution contributions included the influence of time, snow temperature, snow overburden, snow density itself, and rain on snow. Grain-growth and the degree of faceting were parameterized in a snow-structure submodel, where snow grains grew in response to within-snow temperature and vapor pressure gradients and snow density. Snow temperatures and energy and mass transfers within the snowpack were simulated using a snow thermal conductivity parameterization that accounted for snow grain size, density, and habit (e.g., wind slab, depth hoar).

Superimposed ice was simulated and used to define how much end-of-summer snow accumulation was carried over to the next simulation year. This, in addition to knowledge about ice age (in days), helped quantify the seasonal-snow evolution differences on FYI and MYI.

To assess the role of ice motion on the snow-property evolution, two additional model simulations were performed (one with MERRA-2 and one with ERA5 atmospheric forcing) where the ice parcels fixed in space. At the end of the four SnowModel-LG simulations, snow data for each 14×14 -km parcel were gridded to the 25×25 -km EASE grid using an area- and concentration-weighting, property-conserving procedure. Other simulation results and comparisons with observational and remote sensing data are presented in Part II (Stroeve et al., 2020).

5.2. Key Findings

A Lagrangian formulation is required to produce realistic snow-on-sea-ice spatial structures. Sea ice characteristics include sharp edges, instant start times, and longevity that can take system components far beyond their origins. Lagrangian approaches are ideally suited for such an application. Eulerian and incremental remapping approaches are numerically diffusive and, while they generally work well for spatially and temporally continuous variables, they are inappropriate for structures that have large discontinuities in space and time, such as those found in sea ice environments. Sufficient spatial and temporal resolution is also

required to capture the features simulated in this study (e.g., at least 25-km spatial and daily temporal resolution).

Blowing-snow sublimation was found to make an important contribution to the snowpack mass budget. The other primary contributors during the accumulation season were snowfall and ice dynamics.

Superimposed ice was found to be decreasing over the last four decades. In addition, snow carryover to the next accumulation season was minimal and sensitive to the melt-season atmospheric forcing (e.g., the average summer melt period was 3 weeks, or 50%, longer with the ERA5 forcing than the MERRA-2 forcing). The melt period was sensitive to small differences in atmospheric forcing, and this had important consequences for the snow's distribution and seasonal evolution.

A further finding was that ice-parcel age is directly related to ice dynamics; the two are inseparable. Ice dynamics created new parcels, and the age, resolution, movement, and location of those parcels defined the resulting snow-property spatial patterns and evolutions. The ice dynamics played two key roles: (1) it moved the parcels to different areas of the Arctic Ocean over time, so each parcel's snowpack stratigraphic profile represented the atmospheric forcing experienced during the parcels' advection history; and (2) it created new parcels of younger age than the surrounding parcels. Both processes produced relatively high snow property spatial variability. Accounting for ice dynamics was required to reproduce the 2014 OIB snow depth distributions.

Parcel age exerted a first-order control on snow depth in this sea ice environment. Relatively new parcels had less snow on them than surrounding older parcels. Snow properties differed between FYI and MYI primarily because the snow accumulation period was longer on MYI. Snow can accumulate on existing ice when air temperatures are a couple of degrees above freezing, while new ice cannot form until air temperatures are a couple of degrees below freezing. This delay of at least 1 or 2 months means there is typically more snow on MYI later in the snow accumulation season. Our results highlight that actual *parcel age* (in days) is the key variable required to capture the physics associated with snow evolution and the resulting snow properties on ice parcels. It is inadequate to just consider whether ice is classified as FYI or MYI.

Because of the feedbacks between snow density evolution and the snow depth and snow density itself, younger and thinner snow on newer parcels had different snow properties than the older, deeper snow. For example, deeper, older snow had higher densities and was more resistant to being blown by wind. This, in turn, impacts processes such as wind-slab production and blowing-snow sublimation, which were all accounted for in the SnowModel-LG simulations.

5.3. The Future

These Lagrangian snow-evolution simulations set a new standard for understanding snow-on-sea-ice properties and distributions. The resulting pan-Arctic, multidecade data sets include spatial structures and process representations that have not been revealed in previous studies spanning these spatial and temporal domains. The novelty of our results calls for further investigation to demonstrate their validity, or lack thereof. Such investigations should include process-based, field and remote-sensing studies that span large areas at sufficient spatial and temporal resolution to quantify the snow-related features of interest. The simulations presented herein set the stage and encourage us to seek new ways to observe and understand snow processes, properties, and features found in sea ice environments.

Appendix A: SnowModel-LG Overview

SnowModel-LG has its origins as a terrestrial, multilayer, spatially distributed, snow evolution modeling tool called SnowModel (see Liston & Elder, 2006a, and the references contained therein). SnowModel's general development goal was to represent snow processes in any snowscape found anywhere in the world, in computationally efficient and physically realistic ways. SnowModel and SnowModel-LG are identical, with the exception that SnowModel-LG uses prescribed (e.g., daily or weekly) sea ice parcel concentration (0–1) and position data sets to define the substructure that the snow evolves on (sea ice concentrations > 0 can accumulate a snowpack, and sea ice concentrations = 0 cannot). SnowModel evolves snow on land.

Coupled to SnowModel/SnowModel-LG are two other modeling tools: a high-resolution atmospheric model called MicroMet (Appendix G) that provides the meteorological forcing (Liston & Elder, 2006b); and

SnowAssim (Appendix H) that assimilates available field and remote sensing observations (Liston & Hiemstra, 2008). These tools have been designed to be completely flexible in terms of *spatial domain* (i.e., they can be used anywhere in the world, including mountain tops near the equator, middle-latitude mountains and prairies, and the Polar Regions), *temporal domain* (i.e., they can be used for past climates, the current climate, and future climates, for periods that range from hours to centuries), *spatial and temporal resolution* (e.g., 1 m to 100 km, 1-hr to daily), and *subject or variable of interest* (e.g., snow-water for hydrologic applications, and snow strength for wildlife applications).

The coupled MicroMet, SnowModel/SnowModel-LG, SnowAssim tools have been widely used for climate, hydrology, remote sensing, wildlife, vegetation, avalanche, glacier and ice sheet mass balance, and other studies. Results from these studies range from identifying snow-related Wēkiu bug (*Nysius wekiuicola*) population health and distributions near the summit of Mauna Kea, Hawaii; to mapping polar bear (*Ursus maritimus*) maternity den habitat in Alaska, Svalbard, and Franz Josef Land; to quantifying the annual mass balance of every Northern Hemisphere glacier larger than 1 km²; to simulating snow-water resources in the western United States for water-management and infrastructure-design purposes; to simulating pan-Arctic snow-property trends for climate applications.

Processes simulated by SnowModel/SnowModel-LG (Appendix B) include snow precipitation; blowing-snow redistribution and sublimation; forest canopy snow interception, unloading, and sublimation; snow density evolution; and snowpack ripening and melt. SnowModel/SnowModel-LG incorporates first-order physics required to simulate snow evolution within each of the global snow classes (i.e., Ice, Tundra, Taiga, Alpine, Prairie, Maritime, and Ephemeral) defined by Sturm et al. (1995).

MicroMet, SnowModel/SnowModel-LG, and SnowAssim have been used to evolve snow distributions in Colorado, Wyoming, Idaho, Oregon, Alaska, Arctic Canada, Siberia, Japan, Tibet, Chile, Germany, Austria, Svalbard, Norway, Greenland, Antarctica, and the Arctic Ocean as part of a wide variety of snow and ice studies. These applications used grid increments ranging from 1 m to 25 km, over spatial domains ranging from points to continental, and over temporal domains ranging from hours to decades; descriptions of these studies are available in over 100 refereed publications (e.g., Boelman et al., 2019; Bruland et al., 2004; Fletcher et al., 2012; Gascoin et al., 2012; Greene et al., 1999; Hasholt et al., 2003; Hiemstra et al., 2002, 2006; Hoffman et al., 2014, 2016; Liston & Mernild, 2012; Liston & Sturm, 1998, 2002; Liston et al., 2000, 2002, 2007, 2008, 2016, 2018; Liston & Winther, 2005; Liston & Hiemstra, 2008, 2011a, 2011b; Merkouriadi et al., 2020; Mernild et al., 2006, 2008, 2009, 2010, 2011, 2014, 2015; Mernild & Liston, 2010; Pedersen et al., 2015, 2018; Pflug et al., 2019; Prasad et al., 2001; Stuefer et al., 2013; Suzuki et al., 2011; Suzuki, Liston, & Kodama, 2015; Suzuki, Liston, & Matsuo, 2015).

MicroMet, SnowModel/SnowModel-LG, and SnowAssim have evolved extensively over the past several years, and many of those changes have not been formally documented. In addition, some parts of the modeling system have changed from those presented in previous publications. Therefore, the description below provides a comprehensive summary of the SnowModel/SnowModel-LG modeling system used in this pan-Arctic sea ice application. In places where the existing published documentation is accurate and adequate, the summary below references those publications and equations and describes how they fit within the general modeling tool. MicroMet, SnowModel/SnowModel-LG, and SnowAssim are comprised of the 63 equations presented in Appendices A–H, plus the additional 111 equations referenced below that are in other refereed publications, for a total of 174 equations.

Appendix B: SnowModel/SnowModel-LG Mass Budget Equations

SnowModel is a spatially distributed snow-evolution modeling system designed for application in all areas and climates where snow occurs (Liston & Elder, 2006a). For sea ice applications, the Lagrangian (LG) version (SnowModel-LG; see Figure 6 of Liston et al., 2018, for model schematic) includes the ability to track snow evolution on ice parcels that come, go, and move in time and space. SnowModel/SnowModel-LG is an aggregation of four submodels: (1) SnowPack (Liston & Hall, 1995; Liston & Mernild, 2012) is a multilayer snowpack model that simulates snow depth, density, temperature, snow-grain properties, and SWE evolutions (Appendix C); (2) SnowTran-3D (Liston & Sturm, 1998; Liston et al., 2007) accounts for snow transport by wind and the formation of snowdrifts around variable land or ice topography (Appendix D); (3) SnowDunes (Liston et al., 2018) simulates snow depth variations over relatively flat surfaces, including

undeformed, mostly level, sea ice (Appendix E); and (4) EnBal (Liston, 1995; Liston et al., 1999) calculates surface energy exchanges and snowmelt quantities (Appendix F).

SnowModel/SnowModel-LG performs a snow mass-budget calculation at every time step during the year, over a spatial domain where x (m) and y (m) are the horizontal coordinates in the west-east and south-north directions, respectively. Snow-water-equivalent depth, SWE (m), evolution is defined by mass gains, losses, redistributions, and Lagrangian ice dynamics, according to the equation

$$\frac{dSWE}{dt} = \frac{1}{\rho_w}[(P_r + P_s) - (S_{ss} + S_{bs} + S_{ci} + M) + B + Q_{bs} + D], \quad (B1)$$

where t (s) is time; $\rho_w = 1,000 \text{ kg m}^{-3}$ is the water density; P_r and P_s are the water-equivalent rainfall and snowfall fluxes ($\text{kg m}^{-2} \text{ s}^{-1}$), respectively; S_{ss} ($\text{kg m}^{-2} \text{ s}^{-1}$), S_{bs} ($\text{kg m}^{-2} \text{ s}^{-1}$), and S_{ci} ($\text{kg m}^{-2} \text{ s}^{-1}$) are the water-equivalent sublimation from static-surface (a nonblowing-snow surface; this term also accounts for vapor deposition on the snow surface), blowing-snow, and forest canopy snow interception processes, respectively; M ($\text{kg m}^{-2} \text{ s}^{-1}$) is melt-related mass losses (meltwater that has been removed from the snowpack, not refrozen within the snowpack); B ($\text{kg m}^{-2} \text{ s}^{-1}$) represents bedform snow distributions on relatively level land and sea ice surfaces; Q_{bs} ($\text{kg m}^{-2} \text{ s}^{-1}$) is the erosion and deposition at the surface due to blowing snow. In a Lagrangian sea ice application, D ($\text{kg m}^{-2} \text{ s}^{-1}$) represents mass loss and gain from sea ice dynamics processes (this includes parcels created and lost through ice motion, divergence, and convergence). D is calculated by tracking all the other terms in Equation B1 for each parcel, gridding those parcel terms to a rectangular grid, and computing D as the residual of those terms.

The canopy interception sublimation term, S_{ci} , is only invoked in the presence of forests in a terrestrial application. The bedform term, B , only applies to horizontal length scales of $O(1\text{--}10 \text{ m})$, and is therefore prescribed to be zero for model grid increments greater than this scale. The blowing snow erosion and deposition term, Q_{bs} , only applies to horizontal length scales of $O(1\text{--}500 \text{ m})$, and is therefore defined to be zero for grid increments larger than 500 m. The sea ice dynamics term, D , is only present in the SnowModel-LG version of SnowModel. These are all turned on and off with SnowModel/SnowModel-LG setup flags and input fields; therefore, the same model code is used for any and all simulation configurations and applications.

Each term on the right-hand side of Equation B1 can be converted from mass flux units, V_{flux} ($\text{kg m}^{-2} \text{ s}^{-1}$), to water-equivalent depth units, V_{depth} (m), using the formula

$$\rho_w \frac{\partial V_{depth}}{\partial t} = V_{flux}, \quad (B2)$$

where V is the variable of interest. SnowModel/SnowModel-LG uses this relationship when depth is more appropriate to calculate, work with, or output than mass flux.

Snow depth, h_s (m), is related to SWE through the ratio of the snow density, ρ_s (kg m^{-3}), and water density,

$$SWE = \frac{\rho_s}{\rho_w} h_s. \quad (B3)$$

Therefore, the snow depth and snow density distributions and evolutions are calculated from

$$\frac{d(\rho_s h_s)}{dt} = (P_r + P_s) - (S_{ss} + S_{bs} + S_{ci} + M) + B + Q_{bs} + D. \quad (B4)$$

Equations B1 and B4 are the fundamental equations solved by SnowModel/SnowModel-LG. In addition to the state variables (defined here to be variables that require knowledge of the variable value at time t in order to determine the variable value at time $t + \delta t$) represented above (i.e., SWE , snow depth, and snow density), the modeling system evolves other state variables, including snow temperature, snow albedo, and snow-grain diameter.

In the following Appendices we describe the contributions to the evolution of all the SnowModel/SnowModel-LG variables presented in Equations B1–B4: Appendix B covers SWE , h_s , and D ;

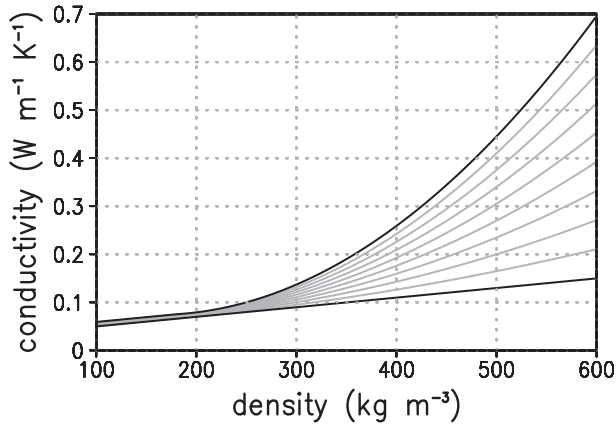


Figure C1. Effective thermal conductivity variation with snow density for wind slab (top black line; assumed grain diameter = 0.1 to 0.5 mm) and fully developed depth hoar (bottom black line; assumed grain diameter = 5.0 mm), and grain diameters in 0.5 mm increments between these two extremes (gray lines). Adapted from Sturm et al. (1997).

Appendix C covers S_{ci} , M , and ρ_s ; Appendix D covers S_{bs} and Q_{bs} ; Appendix E covers B ; Appendix F covers S_{ss} and M ; Appendix G covers P_r and P_s ; and Appendix H covers the data assimilation of observational data sets.

Appendix C: SnowPack

The SnowPack submodel evolves a multilayer snowpack that represents (1) vertical temperature profiles (section C1); (2) snow grain growth (section C2); (3) vertical thermal properties (section C3); (4) the influence of new snow, compaction, wind speed, meltwater percolation and refreezing, and vapor transfers on snow density profiles and evolution (sections C4–C8); (5) forest canopy snow interception sublimation losses for terrestrial applications (section C9).

C1. Snowpack Temperature Evolution

Energy is assumed to be transferred through the snowpack by conduction. The vertical, time-evolving, snow-temperature distribution is described by a one-dimensional heat-transfer equation,

$$\rho_s C_p \frac{\partial T_s}{\partial t} = \frac{\partial}{\partial z} \left(k_s \frac{\partial T_s}{\partial z} \right), \quad (\text{C1})$$

where T_s (K) is the snow temperature and z (m) is the vertical coordinate. The specific heat of ice, C_p ($\text{J kg}^{-1} \text{K}^{-1}$), varies with temperature, and is defined following Anderson (1976),

$$C_p = 92.885 + 7.364 T_s. \quad (\text{C2})$$

The snow thermal conductivity, k_s ($\text{W m}^{-1} \text{K}^{-1}$), is defined after accounting for snow grain-size, density, and habit (e.g., wind slab, depth hoar).

Equation C1, in conjunction with the boundary and initial conditions (Appendix F), and snow density (sections C4–C8), snow thermal conductivity (section C3), snow grain size (section C2), and other snow properties defined below are solved using the finite control-volume methodology described by Patankar (1980).

C2. Grain-Size Parameterization

Grain-growth and degree of faceting is parameterized in a snow-structure submodel following Jordan (1991), where snow grains grow in response to within-snow temperature and vapor pressure gradients and snow density. Wind slabs are simulated in response to the simulated variations in wind speed (Liston et al., 2007). The densest wind slab and fully developed depth-hoar are assumed to have snow-grain diameter limits of 0.1 and 5.0 mm, respectively (e.g., Jordan, 1991; Schmidt, 1982). Grain sizes between these two extremes are simulated in response to the atmospheric forcing and within-snow temperatures and gradients.

For dry snow, the snow grain diameter, G_d (m), grows in response to snowpack temperature gradients, and thus vapor pressure gradients. The snow grain diameter evolution is given by

$$\frac{\partial G_d}{\partial t} = \frac{g_1}{G_d} |U_v|, \quad (\text{C3})$$

where the parameter $g_1 = 5.0 \times 10^{-7} \text{ m}^4 \text{ kg}^{-1}$ (Jordan, 1991).

The mass vapor flux, U_v ($\text{kg m}^{-2} \text{s}^{-1}$), is given by

$$U_v = -\psi E_{es} C_{iT} \frac{\partial T_s}{\partial z}, \quad (C4)$$

where E_{es} ($\text{m}^2 \text{s}^{-1}$) is the effective diffusion coefficient for snow and C_{iT} ($\text{kg m}^{-3} \text{K}^{-1}$) is the ice equilibrium vapor density variation with temperature. E_{es} is defined to be

$$E_{es} = E_{e0s} \left(\frac{1.0 \times 10^5}{\Lambda_a} \right) \left(\frac{T_s}{T_m} \right)^6, \quad (C5)$$

where Λ_a (Pa) is the atmospheric pressure, $T_m = 273.15 \text{ K}$ is the melting temperature, and $E_{e0s} = 9.2 \times 10^5 \text{ m}^2 \text{s}^{-1}$ is the effective diffusion coefficient at $\Lambda_a = 1.0 \times 10^5 \text{ Pa}$ and $T_s = T_m$ (Jordan, 1991).

The atmospheric pressure, Λ_a (Pa), for the location of interest is given by

$$\Lambda_a = \Lambda_0 \exp\left(-\frac{H}{H_s}\right), \quad (C6)$$

where $\Lambda_0 = 101,300 \text{ Pa}$ is a reference sea level pressure, H_s (m) is the scale height of the atmosphere ($\approx 8,000 \text{ m}$), and H (m) is the surface elevation (Wallace & Hobbs, 1977).

C_{iT} is defined to be

$$C_{iT} = \frac{c_{li}}{T_s^2} \left(\frac{L_{vi}}{R_w T_s} - 1 \right) e^{-\left(\frac{L_{vi}}{R_w T_s}\right)}, \quad (C7)$$

where the parameter $c_{li} = 7.964 \times 10^9 \text{ kg K m}^{-3}$, $L_{vi} = 2.838 \times 10^6 \text{ J kg}^{-1}$ is the latent heat of sublimation for ice, and $R_w = 461.5 \text{ J K}^{-1} \text{ kg}^{-1}$ is the gas constant for water vapor (Jordan, 1991).

In contrast to Jordan (1991), we assume the vapor fluxes are proportional to the snow porosity. This has the desired effect of driving the fluxes to zero when the porosity is zero. The ratio of the pore volume to the total volume, or porosity, ψ ($\text{m}^3 \text{m}^{-3}$), is defined to be

$$\psi = 1 - \frac{\rho_s}{\rho_i}, \quad (C8)$$

where $\rho_i = 917 \text{ kg m}^{-3}$ is the ice density.

The initial grain diameter, G_0 (m), required by Equation C3 depends on whether there is blowing snow present. G_0 is given by

$$G_0 = G_{0i} - A_1 \{1.0 - \exp[-A_2(W_r - 5.0)]\}, \quad (C9)$$

where $G_{0i} = 0.0005 \text{ m}$, and A_1 and A_2 are constants set equal to 0.0004 m and 0.2 s m^{-1} , respectively; A_1 defines the maximum diameter reduction for an approximately 30.0 m s^{-1} wind speed, and A_2 controls the progression weight from low to high wind speeds. The wind speed, W_r (m s^{-1}), is defined to be at reference height $z_r = 2 \text{ m}$.

Equation C9 produces an initial grain diameter of 0.5 mm for wind speeds below 5 m s^{-1} (where no blowing snow occurs), and diameters between 0.5 and 0.1 mm for wind speeds between 5 and 30 m s^{-1} , respectively (diameter decreases with increasing wind speed and increasing blowing snow transport). These diameters are consistent with blowing snow particle sizes measured by Schmidt (1982, 1986). The fluxes associated with grain evolution are computed following the control volume and harmonic-mean diffusion coefficient calculations of Patankar (1980).

C3. Thermal Conductivity

The snow thermal conductivity for the two snow-grain-size extremes defined in the grain-size parameterization are defined using Figures 9 and 10 of Sturm et al. (1997), where the wind slab (0.1 to 0.5 mm grain size) thermal conductivity is

$$k_{s; 0.1mm - 0.5mm} = \begin{cases} 3.94 \times 10^{-2} + 2.00 \times 10^{-4} \rho_s; & \rho_s < 180 \\ 1.55 \times 10^{-1} - 1.02 \times 10^{-3} \rho_s + 3.21 \times 10^{-6} \rho_s^2; & 180 \leq \rho_s \leq 600 \end{cases}, \quad (C10)$$

and the fully developed depth hoar (5.0 mm grain size) thermal conductivity is

$$k_{s; 5.0mm} = 3.00 \times 10^{-2} + 2.00 \times 10^{-4} \rho_s; \quad \rho_s \leq 600. \quad (C11)$$

For simulated grain sizes between these two extremes, the thermal conductivity is defined to be a linear weighting between the Equations C10 and C11 curves (Figure C1).

C4. Snow Density Evolution

The density of new snow, ρ_{ns} (kg m^{-3}), is assumed to receive additive contributions from air temperature and moisture, and blowing snow,

$$\rho_{ns} = \rho_{tm} + \rho_{bs}, \quad (C12)$$

where ρ_{tm} (kg m^{-3}) is the temperature and moisture contribution and ρ_{bs} (kg m^{-3}) is the blowing snow contribution.

The snow density associated with temperature and moisture is defined following Anderson (1976), based on data by LaChapelle (1969),

$$\rho_{tm} = 50 + 1.7(T_{wb} - 258.16)^{1.5}; \quad T_{wb} \geq 258.16, \quad (C13)$$

where T_{wb} (K) is the wet-bulb air temperature. The wet-bulb temperature is given by Rogers (1979),

$$T_{wb} = T_a + (e_a - e_s T_{wb}) \left(\frac{0.622 L_v}{\Lambda_a C_{pa}} \right), \quad (C14)$$

where T_a (K) is the air temperature, $L_v = 2.500 \times 10^6 \text{ J kg}^{-1}$ is the latent heat of vaporization at 0°C , $C_{pa} = 1,004 \text{ J kg}^{-1} \text{ K}^{-1}$ is the specific heat of air at 0°C , e_a (Pa) is the vapor pressure of air, and e_s (Pa) is the saturation vapor pressure at T_{wb} .

The vapor pressure of air is defined following Buck (1981),

$$e_a = \frac{RH}{100.0} A \exp \left(\frac{B(T_a - T_f)}{C + (T_a - T_f)} \right), \quad (C15)$$

where RH (%) is the relative humidity and $T_f = 273.15 \text{ K}$ is the freezing temperature. Over water, the coefficients A , B , and C are 611.21, 17.502, and 240.97, respectively (Buck, 1981). For applications over ice, these A , B , and C coefficients are 611.15, 22.452, and 272.55, respectively. The saturation vapor pressure is found by setting RH to 100.0 in Equation C15.

Equation C14 is solved iteratively for T_{wb} using the Newton-Raphson method (Burden & Faires, 1989). Sadeghi et al. (2013) provided an analytical alternative to this solution method.

During a precipitation event, the initial snow density of the newly forming top snow layer increases through the influence of blowing and drifting snow. For wind speeds $\geq 5 \text{ m s}^{-1}$, a blowing-snow new-snow density contribution, ρ_{bs} (kg m^{-3}), in Equation C12, is given by

$$\rho_{bs} = C_1 + C_2 \{1.0 - \exp[-C_3(W_r - 5.0)]\}, \quad (C16)$$

where C_1 , C_2 , and C_3 are constants set equal to 25.0 kg m^{-3} , 250.0 kg m^{-3} , and 0.2 s m^{-1} , respectively; C_1 defines the density offset for a 5.0 m s^{-1} wind; C_2 defines the maximum density increase due to wind; and C_3 controls the progression from low to high wind speeds (Liston et al., 2007).

After each layer of the snowpack has been initialized with the above new-snow densities, the density of each snowpack layer evolves in time in response to known contributors following

$$\frac{\partial \rho_s}{\partial t} = \rho_{sc} + \rho_{sw} + \rho_{sf} + \rho_{sv}, \quad (\text{C17})$$

where snow density changes occur due to compaction, ρ_{sc} (kg m^{-3}), wind (i.e., blowing snow), ρ_{sw} (kg m^{-3}), freezing of liquid water, ρ_{sf} (kg m^{-3}), and vapor migration through the snowpack, ρ_{sv} (kg m^{-3}).

C5. Snow Density Changes From Compaction

Snow density increases from compaction following Anderson (1976),

$$\rho_{sc} = \beta_u N_1 W_s \rho_s \exp[-N_2 (T_f - T_s)] \exp(-N_3 \rho_s), \quad (\text{C18})$$

where W_s (m) is the weight of snow above a given layer expressed in water-equivalent-depth units; N_1 , N_2 , and N_3 are constants set equal to $0.0013 \text{ m}^{-1} \text{ s}^{-1}$, 0.08 K^{-1} , and $0.021 \text{ m}^3 \text{ kg}^{-1}$, respectively, based on Kojima (1967); and β_u (dimensionless) is a user-defined snow density rate adjustment factor that can be used to make the snow density increase faster ($\beta_u > 1.0$) or slower ($\beta_u < 1.0$). Usually β_u is defined based on available snow density observations, otherwise it is set to 1.0.

C6. Snow Density Changes From Wind

Wind speed contributes to snow density evolution during periods of no precipitation. In this case, the density of the top snow layer evolves similar to Anderson (1976), but with a wind-speed contribution, U . This temporal change in snow density from blowing snow, ρ_{sw} , is given by

$$\rho_{sw} = m_1 N_1 U \rho_s \exp[-N_2 (T_f - T_s)] \exp(-N_3 \rho_s), \quad (\text{C19})$$

where $m_1 = 0.10$ is a nondimensional constant that controls the simulated snow density change rate.

For wind speeds $\geq 5 \text{ m s}^{-1}$, U is given by

$$U = E_1 + E_2 \{1.0 - \exp[-E_3 (W_r - 5.0)]\}, \quad (\text{C20})$$

with E_1 , E_2 , and E_3 defined to be 5.0, 15.0, and 0.2 s m^{-1} , respectively; E_1 defines the U offset for a 5.0 m s^{-1} wind; E_2 defines the maximum U increase due to wind; and E_3 controls the progression of U from low to high wind speeds (Liston et al., 2007). For wind speeds $< 5 \text{ m s}^{-1}$, U is defined to equal 1.0 m s^{-1} . This approach limits the density increase resulting from wind transport to winds capable of moving snow (assumed to be winds $\geq 5 \text{ m s}^{-1}$). Numerous studies have observed a 4- to 5-m s^{-1} snow-transport wind speed threshold for new or slightly aged cold, dry (e.g., below approximately -2°C) snow; see Kind (1981) and the references contained therein and Li and Pomeroy (1997).

C7. Snow Density Changes From Freezing of Liquid Water

Liquid water available at the snow surface, either through snowmelt or rainfall, percolates into the snowpack from top to bottom, freezing within each layer, depending on each layer's cold content or energy available to freeze the liquid water. This process is described using a simple continuity equation (see Equation C17)

$$\rho_{sf} = \frac{\partial M}{\partial z}. \quad (\text{C21})$$

Here the snowmelt, M ($\text{kg m}^{-2} \text{ s}^{-1}$), is given by

$$L_f M = Q_m, \quad (\text{C22})$$

where the snowmelt energy, Q_m (W m^{-2}), is calculated from a full surface energy balance (Appendix F) and $L_f = 3.34 \times 10^5 \text{ J kg}^{-1}$ is the latent heat of fusion of water at 0°C .

The cold content available freeze liquid water in the snowpack, Q_f (W m^{-2}), is used to calculate the potential freezing, F_p ($\text{kg m}^{-2} \text{ s}^{-1}$), of any available liquid water, and is given by

$$L_f F_p = -Q_f, \quad (C23)$$

where Q_f is obtained by setting the surface temperature in the surface energy balance (Appendix F) to the freezing temperature and solving for the residual. M and F_p can be converted to depth units using Equation B2. Available liquid water moves through the snowpack, freezing when the potential freeze depth is nonzero, until a maximum snow density (550 kg m^{-3}) is reached. Any additional meltwater drains out the snowpack bottom and is considered snowpack runoff. Alternatively, the more complex, and physically realistic, gravity drainage representation by Pflug et al. (2019) is available to simulate liquid water percolation through the snowpack.

C8. Snow Density Changes From Vapor Movement

Vapor movement through the snowpack can redistribute mass between layers. This is defined following Sturm and Benson (1997) as

$$\rho_{sv} = -K \frac{\partial U_v}{\partial z}, \quad (C24)$$

where the mass vapor flux, U_v , is given by Equation C4, and K is a nondimensional user-defined parameter that is set based on snow density profile observations. Equation C24 describes the change of snow layer density with time, in response to vapor transfers between layers; it is solved following Patankar (1980).

C9. Forest Canopy Snow Interception

SnowPack modifications resulting from forest canopy snow interception, and the associated sublimation fluxes, S_{ci} ($\text{kg m}^{-2} \text{ s}^{-1}$), are described by Equations 3–24 in Liston and Elder (2006a).

Appendix D: SnowTran-3D

SnowTran-3D is a 3-dimensional model that simulates wind-driven snow depth evolution over topographically variable terrain (defined by the land or ice surface topography). This blowing snow model has been thoroughly described in Liston and Sturm (1998) and Liston et al. (2007, 2018). SnowTran-3D's primary components are (1) the wind-flow forcing field, (2) the wind-shear stress on the surface, (3) the transport of snow by saltation and turbulent suspension (the dominant wind-transport modes), (4) the sublimation of saltating and suspended snow, and (5) the accumulation and erosion of snow at the snow surface.

D1. Erosion and Deposition

The foundation of SnowTran-3D is a mass-balance equation that describes the temporal variation of snow depth at each point within the simulation domain, in response to blowing snow deposition and erosion, Q_{bs} ($\text{kg m}^{-2} \text{ s}^{-1}$). Changes in snow depth result from spatial variation in horizontal mass-transport rates of saltation, Q_{salt} ($\text{kg m}^{-1} \text{ s}^{-1}$), and differences in horizontal mass-transport rates of turbulent-suspended snow, Q_{turb} ($\text{kg m}^{-1} \text{ s}^{-1}$). Transport in the creeping and rolling modes are assumed to be negligibly small. Combined, Q_{bs} is given by

$$Q_{bs} = \frac{\partial Q_{salt_x}}{\partial x} + \frac{\partial Q_{turb_x}}{\partial x} + \frac{\partial Q_{salt_y}}{\partial y} + \frac{\partial Q_{turb_y}}{\partial y}, \quad (D1)$$

where mass fluxes to the surface are defined to be positive. At each time step, Equation D1 is solved for individual grid cells within the domain and is coupled to the neighboring cells through spatial derivatives ($\partial/\partial x$, $\partial/\partial y$).

High resolution, spatially varying wind fields are simulated across surface topographic features following Liston and Sturm (1998), Liston and Elder (2006b), and Liston et al. (2007). This wind field exerts a surface shear stress on the snow. SnowTran-3D also includes an accounting of the snow-surface shear strength (Liston et al., 2007) through the snow density equations listed above. When the surface shear stress exceeds the snow-surface shear strength of the snow, snow is transported at the flux rates defined by Liston and Sturm (1998). The spatial variation in these fluxes (Liston & Sturm, 1998) define the snow erosion and deposition fields.

The blowing-snow transport component of SnowTran-3D is described by Equations 1–21 of Liston and Sturm (1998), and Equations 19–24 of Liston et al. (2007).

D2. Blowing-Snow Sublimation

During transport by saltation and turbulent-suspension, snow particles can lose mass to the atmosphere through sublimation. The sublimation rate of wind-transported snow, S_{bs} ($\text{kg m}^{-2} \text{s}^{-1}$), is given by

$$S_{bs}(x^*) = \Psi_s \varphi_s h^* + \int_{h^*}^{z_t} \Psi_t(x^*, z) \varphi_t(x^*, z) dz, \quad (\text{D2})$$

where x^* (m) is the horizontal coordinate in a reference frame defined by the wind-flow direction (increasing downwind), the subscripts s and t refer to saltation and turbulent-suspension, respectively, Ψ (s^{-1}) is the sublimation-loss rate coefficient, φ (kg m^{-3}) is the vertical mass-concentration distribution, and the integration limits are from the snow surface through the saltating and turbulent-transport regimes. Here we have assumed that the saltation layer contribution ($z = 0$ to $z = h^*$; first term on the right-hand side) is separated from the turbulent-suspension contribution ($z = h^*$ to $z = z_t$; second term on the right-hand side), and coupled through their common boundary.

Our formulation for the sublimation rate of wind-transported snow follows Schmidt (1972, 1991), Pomeroy et al. (1993), and Pomeroy and Gray (1995). The sublimation-loss rate coefficient, Ψ , describing the rate of particle mass-loss as a function of height within the blowing and drifting snow profile is a function of (1) temperature-dependent humidity gradients between the snow particle and the atmosphere, (2) conductive and advective energy and moisture transfer mechanisms, (3) particle size, and (4) solar radiation intercepted by the particle. In addition, we assume that (a) the mean particle size decays exponentially with height, (b) the relative humidity follows a logarithmic distribution, decreasing with height, (c) the air temperature in the snow-transport layer is well mixed and constant with height, (d) the variables defined within the saltation layer are constant with height, and those in the turbulent-suspension layer vary with height, and (e) the solar radiation absorbed by snow particles is a function of the solar elevation angle (latitude, time-of-day, day-of-year) and fractional cloud cover, σ_c . The full blowing-snow sublimation component of SnowTran-3D is described by Equations A1–A24 of Liston and Sturm (1998).

Appendix E: SnowDunes

SnowDunes (Liston et al., 2018) was created to simulate snow-bedform distributions on relatively flat terrain, including level, undeformed sea ice. In the SnowDunes context, snow bedforms include snow deposition features such as barchans, dunes, snow-waves, whalebacks, crags and tails, and other features that have not been documented or named. Snow bedforms also include erosion features such as sastrugi (and all its variants), irregular patterns (Doumani, 1967), pits, and other features that have not yet been documented or named (Filhol & Sturm, 2015).

E1. Digital Filter

SnowDunes builds on the qualitative turbulent-wind and bedform-creation ideas of Sturm and Liston (2003). The model requires inputs of representative area-average snow-depth mean and standard deviation, and snow-dune wavelength, and it outputs spatially distributed snow depths that match these statistics. SnowDunes is a statistical (as opposed to deterministic) model, in keeping with observed snow-bedform distributions (Filhol & Sturm, 2015; Liston et al., 2018).

SnowDunes defines a random initial field that is modified using a convolution or digital linear nonrecursive filter. The following digital filter, b , operation defines a snow-bedform depth distribution index, $\zeta_{index}(\mathbf{m})$, in the x, y plane over the simulation domain, where i and j are the grid coordinates of the simulation domain grid cells,

$$\zeta_{index}(i, j) = \sum_{i'=-N_x}^{N_x} \sum_{j'=-N_y}^{N_y} b(i', j') R(i + i', j + j'), \quad (\text{E1})$$

over a collection of random numbers, R (m), with zero mean and that range between -1 and $+1$. Here $\pm N_x$ and $\pm N_y$ represent the filter support (in number of grid cells) in directions x and y ,

corresponding to the digital filter, b , while it is applied over the filter subdomain grid cells represented by i' and j' .

E2. Dune Depth Distribution

The snow-bedform index field is converted to the snow-bedform depth distribution, ζ_b (m), by scaling ζ_{index} by the ratio of the observed snow-bedform depth standard deviation, σ_{obs} (m), to the ζ_{index} standard deviation, $\sigma_{\zeta_{index}}$ (m), and by an adjustment to reproduce the mean snow depth, μ (m),

$$\zeta_b(i, j) = \mu + \left(\zeta_{index}(i, j) - \mu_{\zeta} \right) \left(\frac{\sigma_{obs}}{\sigma_{\zeta_{index}}} \right), \quad (E2)$$

where μ_{ζ} (m) is the mean of ζ_{index} . The mean snow depth can be defined using observations or a model product.

Equation E2 is converted to mass flux units, B ($\text{kg m}^{-2} \text{s}^{-1}$), using

$$B = \rho_w \frac{\partial \zeta_b}{\partial t}, \quad (E3)$$

to be compatible with Equations B1 and B4.

The result is a random, but spatially correlated, snow-bedform depth distribution field that preserves the input statistics, including the snow-depth relative frequency histograms. A Gaussian correlation function was used to represent our conceptual wind-turbulence forcing mechanism and the resulting snow-bedform depth distributions. Additional details of the SnowDunes formulation and implementation are provided by Liston et al. (2018). Equations 1–9, and 11, of Liston et al. (2018) describe the complete SnowDunes model.

Appendix F: EnBal

The solution of Equation C1 requires top and bottom snow-temperature boundary conditions and initial conditions, and Equations C22 and C23 require melt energy and cold content inputs, respectively. The top boundary condition is determined by performing a full energy balance at the surface in the form

$$(1 - \alpha) Q_{si} + Q_{li} + Q_{le} + Q_h + Q_e + Q_c = Q_m, \quad (F1)$$

where Q_{si} (W m^{-2}) is the solar (shortwave) radiation reaching Earth's surface, Q_{li} (W m^{-2}) is the incoming longwave radiation, Q_{le} (W m^{-2}) is the emitted longwave radiation, Q_h (W m^{-2}) is the turbulent exchange of sensible heat, Q_e (W m^{-2}) is the turbulent exchange of latent heat, Q_c (W m^{-2}) is the conductive energy transport, and Q_m (W m^{-2}) is the energy flux available for melt.

Each term in Equation F1 is computed by applying equations that have been cast in a form that leaves the surface (skin) temperature, T_0 (K), as the only unknown. The melt energy is defined to be zero, and Equation F1 is solved iteratively for the surface temperature using the Newton-Raphson method (Burden & Faires, 1989). In the presence of snow, surface temperatures greater than 0°C indicate that energy is available for melting. This energy is computed by fixing the surface temperature at 0°C and solving Equation F1 for Q_m . A similar procedure is used to compute the energy available to freeze, Q_f , any liquid water present within the snowpack (see Equation C23). The resulting value of T_0 is then used as the top boundary condition for Equation C1.

Because SnowModel does not include a soil-temperature submodel, and SnowModel-LG does not include a sea ice and ocean model, the lower boundary condition is defined to be a spatial and temporal constant equal to -1.0°C . This can be relaxed if additional information from observations or from a below-snow model is available. If a snowpack exists at the start of the model simulation, initial conditions throughout the profile are defined to be constant and equal to the snowpack lower boundary condition. Under this definition, the profile has typically reached equilibrium with its environment within several days.

In what follows, each term in the Equation F1 energy balance is described. Energy transfers to the surface are defined to be positive.

F1. Incoming Solar Radiation

Solar radiation striking Earth's surface, including the influence of sloping terrain, is given by

$$Q_{si} = S^* (\Psi_{dir} \cos i + \Psi_{dif} \cos Z), \quad (F2)$$

where the angle between direct solar radiation and a sloping surface is given by i , under the assumption that diffuse radiation impinges upon an area corresponding to a horizontal surface. The solar irradiance at the top of the atmosphere striking a surface normal to the solar beam is given by $S^* = 1,370 \text{ W m}^{-2}$ (Kyle et al., 1985), and Ψ_{dir} and Ψ_{dif} are the direct and diffuse, respectively, net sky transmissivities, or the fraction of solar radiation reaching the surface.

The solar zenith angle, Z , is

$$\cos Z = \sin \delta \sin \varphi + \cos \delta \cos \varphi \cos \tau, \quad (F3)$$

where φ is latitude and τ is the hour angle measured from local solar noon,

$$\tau = \pi \left(\frac{h}{12} - 1 \right), \quad (F4)$$

where h is the hour of the day. The solar declination angle, δ , is approximated by

$$\delta = \varphi_T \cos \left[2\pi \left(\frac{d - d_r}{d_y} \right) \right], \quad (F5)$$

where $\varphi_T = 0.409$ radians is the latitude of the Tropic of Cancer, d is the day of the year, $d_r = 173$ is the day of the summer solstice in Northern Hemisphere, and $d_y = 365.25$ is the average number of days in a year.

The angle i is given by

$$\cos i = \cos \beta \cos Z + \sin \beta \sin Z \cos(\mu - \xi), \quad (F6)$$

and the terrain slope, β , is given by

$$\beta = \tan^{-1} \left[\left(\frac{\partial H}{\partial x} \right)^2 + \left(\frac{\partial H}{\partial y} \right)^2 \right]^{\frac{1}{2}}, \quad (F7)$$

where H (m) is the topographic height, and x (m) and y (m) are the horizontal coordinates. The terrain slope azimuth, ξ , with south having zero azimuth, is

$$\xi = \frac{\pi}{2} - \tan^{-1} \left[\frac{\partial H / \partial y}{\partial H / \partial x} \right]. \quad (F8)$$

The solar azimuth, μ , with south having zero azimuth, is given by

$$\mu = \sin^{-1} \left(\frac{\cos \delta \sin \tau}{\sin Z} \right). \quad (F9)$$

To account for scattering, absorption, and reflection of solar radiation by clouds, the solar radiation is scaled according to (Burridge & Gadd, 1974)

$$\Psi_{dir} = (0.6 - 0.2 \cos Z) (1.0 - \sigma_c) \quad (F10)$$

for direct solar radiation and

$$\Psi_{dif} = (0.3 - 0.1 \cos Z) \sigma_c \quad (F11)$$

for diffuse solar radiation.

The cloud-cover fraction, σ_c , is given by Walcek (1994)

$$\sigma_c = 0.832 \exp\left(\frac{RH_{700} - 100}{41.6}\right); \quad (0 \leq \sigma_c \leq 1), \quad (F12)$$

where RH_{700} (%) is the relative humidity at 700 hPa. See Liston and Elder (2006b) for additional details on the cloud-cover fraction formulation.

Alternatively, incoming solar radiation and/or cloud cover can also be prescribed in the modeling system using other model, (re)analyses, or observational products (Liston & Elder, 2006b).

F2. Albedo

In SnowModel's/SnowModel-LG's simplest option, dry snow and melting snow are prescribed fixed albedos, $\alpha = 0.8$ and 0.6 , respectively, in time and space. Alternatively, the snow albedo is given by Strack et al. (2004) based on Douville et al. (1995).

For cold, dry snow, the albedo, α , is defined by

$$\frac{\partial \alpha}{\partial t} = -\frac{\tau_a}{\tau_1}, \quad (F13)$$

where $\tau_a = 0.008$ and $\tau_1 = 86,400$ s. For a wet, melting snowpack, the albedo is defined by

$$\frac{\partial \alpha}{\partial t} = \frac{1}{\delta t} \left[(\alpha - \alpha_{\min}) \exp\left(-\tau_f \frac{\delta t}{\tau_1}\right) + \alpha_{\min} - \alpha \right], \quad (F14)$$

where δt is the time increment, $\alpha_{\min} = 0.5$, and $\tau_f = 0.24$. New snow is assigned an albedo of 0.8 , and the albedo is reset to 0.8 after 0.003 m of snow-water-equivalent precipitation has fallen. Equations F13 and F14 gradually decrease the albedo to a minimum of 0.5 as the snow ages.

The snow albedo can also be prescribed in the modeling system using other model or observational products.

F3. Incoming Longwave Radiation

Incoming longwave radiation is calculated while accounting for cloud cover fraction and elevation-related variations following Iziomon et al. (2003). Incoming longwave radiation reaching Earth's surface is given by

$$Q_{li} = \varepsilon \sigma T_a^4, \quad (F15)$$

where $\sigma = 5.670 \times 10^{-8} \text{ W m}^{-2} \text{ K}^{-4}$ is the Stefan-Boltzmann constant. The atmospheric emissivity, ε , is

$$\varepsilon = \omega (1 + Z_s \sigma_c^2) [1 - X_s \exp(-Y_s e_a / T_a)], \quad (F16)$$

where e_a (Pa) is the atmospheric vapor pressure defined by Equation C15, and the coefficient $\omega = 1.083$ (Iziomon et al., 2003; Liston & Elder, 2006b).

The coefficients X_s , Y_s , and Z_s depend on elevation according to

$$\begin{aligned} I_s &= I_1; & H < 200 \\ I_s &= I_1 + (H - H_1) \left(\frac{I_2 - I_1}{H_2 - H_1} \right); & 200 \leq H \leq 3000, \\ I_s &= I_2; & 3000 < H \end{aligned} \quad (F17)$$

where H (m) is the surface elevation, and X , Y , and Z can be substituted for I , with $X_1 = 0.35$, $X_2 = 0.51$, $Y_1 = 0.100 \text{ K Pa}^{-1}$, $Y_2 = 0.130 \text{ K Pa}^{-1}$, $Z_1 = 0.224$, $Z_2 = 1.100$, $H_1 = 200$ m, and $H_2 = 3,000$ m (Iziomon et al., 2003; Liston & Elder, 2006b). Additional details of how these parameter values were defined are provided by Liston and Elder (2006b)

F4. Emitted Longwave Radiation

The longwave radiation emitted by the snow surface is computed under the assumption that snow emits as a gray body,

$$Q_{le} = -\varepsilon_s \sigma T_0^4, \quad (F18)$$

where ε_s is the snow surface emissivity, assumed to be 0.98, and T_0 (K) is the surface (skin) temperature.

F5. Sensible and Latent Heat

The turbulent exchange of sensible and latent heat, respectively, are given by (Price & Dunne, 1976)

$$Q_h = \rho_a c_{pa} \Gamma_h \xi (T_a - T_0), \quad (F19)$$

$$Q_e = \rho_a L_v \Gamma_e \xi \left(0.622 \frac{e_a - e_0}{P_a} \right), \quad (F20)$$

where ξ is a nondimensional stability function; $\rho_a = 1.275 \text{ kg m}^{-3}$ is the air density at 0°C and an atmospheric pressure of $1.0 \times 10^5 \text{ Pa}$; e_0 (Pa) is the saturation vapor pressure of the snow surface (at surface temperature, T_0); and the atmospheric pressure, P_a , is given by Equation C6.

Γ_h and Γ_e (m s^{-1}) are exchange coefficients for sensible and latent heat, respectively,

$$\Gamma_{h,e} = \frac{\kappa^2 W_r}{[\ln(z_r/z_0)]^2}, \quad (F21)$$

where $\kappa = 0.40$ (dimensionless) is von Karman's constant, W_r (m s^{-1}) is the wind speed at reference height z_r (m), and z_0 (m) is the roughness length for momentum, assumed to equal $1.0 \times 10^{-4} \text{ m}$. In this application the heat and moisture roughness lengths are assumed to equal that of momentum.

The stability function, ξ , is defined following the surface flux parameterization of Louis (1979) and depends on the bulk Richardson number, Ri (dimensionless). Ri is defined by

$$Ri = \frac{g}{T_a} \frac{\partial T_a / \partial z}{(\partial W_r / \partial z)^2}, \quad (F22)$$

where $g = 9.81 \text{ m s}^{-2}$ is the gravitational acceleration, the atmospheric temperature gradient is computed using the reference-level air temperature and the surface (skin) temperature, and the wind gradient is calculated using the reference-level wind speed and zero wind speed at the surface.

Under unstable atmospheric conditions ($Ri < 0$), ξ modifies the turbulent fluxes through the formula

$$\xi = 1 - \frac{\eta Ri}{1 + \gamma |Ri|^{1/2}}, \quad (F23)$$

where $\eta = 9.4$, and

$$\gamma = \psi \eta \frac{\Gamma_{h,e}}{W_r} \left(\frac{z_r}{z_0} \right)^{1/2}, \quad (F24)$$

where $\psi = 5.3$.

Under stable atmospheric conditions ($Ri > 0$),

$$\xi = 1 / (1 + \eta^* Ri)^2, \quad (F25)$$

where $\eta^* = \eta/2$. When the atmosphere is neutrally buoyant (i.e., $Ri = 0$), $\xi = 1.0$.

The latent heat flux is used to calculate the static-surface sublimation, S_{ss} ($\text{kg m}^{-2} \text{ s}^{-1}$), using

$$L_{wi}S_{ss} = -Q_e, \quad (\text{F26})$$

where vapor transfers away from the surface (negative Q_e) yields positive sublimation values that result in mass lost from the surface (because of the negative sign in Equations B1 and B4). Similarly, vapor deposition on the surface results in surface mass gain. S_{ss} can be converted to depth units using Equation B2.

F6. Heat Conduction

The heat conduction flux at the surface ($z = h_s$) is given by

$$Q_c = -k_s \frac{\partial T_s}{\partial z} \bigg|_{z=h_s}, \quad (\text{F27})$$

where the required temperature profile is computed from Equation C1.

Appendix G: MicroMet

Atmospheric property distributions required to solve SnowModel/SnowModel-LG Equations B1–B4, C1–C24, D1–D2, E1–E3, F1–F27, and G1–G3 are provided by MicroMet. MicroMet performs two kinds of adjustments to the available meteorological data: (1) all available data, at a given time, are spatially interpolated over the domain, and (2) physical submodels are applied to each MicroMet variable to improve parameter realism at a given point in space and time. The base meteorological data can be provided in the form of meteorological station observations, or gridded (re)analyses or remote sensing products.

The model distributes fundamental atmospheric forcing variables required to run most Earth-surface process models, including SnowModel/SnowModel-LG: (1) air temperature, (2) relative humidity, (3) wind speed, (4) wind direction, (5) incoming solar radiation, (6) incoming longwave radiation, (7) surface pressure, and (8) precipitation. To calculate these distributions, MicroMet assumes at least one value of each of the following meteorological variables are available at each time step of interest, somewhere within (or near) the simulation domain: air temperature, relative humidity, wind speed, wind direction, and precipitation. The model uses known relationships between meteorological variables and the surrounding landscape (primarily topography) to distribute those variables over any given domain in computationally efficient and physically plausible ways.

For surface pressure and incoming solar and longwave radiation, MicroMet has two options: (1) let the MicroMet submodels create the distributions (in the absence of observations), or (2) merge available observations and/or (re)analyses products with the submodel generated distributions, as part of a data assimilation procedure. This second option produces distributions that closely match the observations when and where they exist, while accounting for higher resolution information such as topographic slope and aspect.

MicroMet's spatial interpolation and physically based adjustment procedures are described in Liston and Elder (2006b).

G1. Rain and Snow Precipitation

Precipitation is a key SnowModel/SnowModel-LG input. It defines the amount of snow available to accumulate and evolve across the landscape and icescape, and it plays a key role in defining snow properties and snow property evolution. Precipitation inputs are generally provided to MicroMet in units of water-equivalent mass flux ($\text{kg m}^{-2} \text{s}^{-1}$); this is equivalent to units of mm s^{-1} . MicroMet converts these values to water-equivalent rainfall and snowfall fluxes following Dai (2008). The snowfall fraction, P_{sf} (0–1), is given by

$$P_{sf} = J_1 (\tanh\{J_2 [(T_a - T_f) - J_3]\} - J_4), \quad (\text{G1})$$

where, over land, parameters J_1 , J_2 , J_3 , and J_4 , are -0.482292 , 0.7205 , 1.1662 , and 1.0223 , respectively; and over ocean, they are -0.471472 , 0.4049 , 1.9280 , and 1.0203 , respectively (Dai, 2008).

This snowfall fraction is used to convert water-equivalent precipitation mass flux, P ($\text{kg m}^{-2} \text{s}^{-1}$), into rainfall, P_r ($\text{kg m}^{-2} \text{s}^{-1}$), and snowfall, P_s ($\text{kg m}^{-2} \text{s}^{-1}$), quantities at every time step using the formulas

$$P_s = P_{sf}P, \quad (G2)$$

$$P_r = (1 - P_{sf})P. \quad (G3)$$

Rainfall, snowfall, or any combination of the two can fall on the SnowModel/SnowModel-LG snowpack at any given time step, while partitioned according to the above formulas. Precipitation variation with elevation is given by Equation 33 in Liston and Elder (2006b).

G2. SnowPack Layer Formation

Snow layers simulated by SnowModel/SnowModel-LG are created by temporally continuous precipitation events. For example, if there is nonzero snowfall for three model time steps in a row, followed by zero snowfall at the next time step, the snow that fell during that three-time-step period creates a new snow layer. This approach was chosen because it mimics the stratigraphy found in natural snowpacks, where each snow layer can often be traced to the specific storm that created it (e.g., Benson & Sturm, 1993; Sturm et al., 2001).

Numerically, there is no limit to the number of snow layers generated during a model simulation (hundreds are possible). In practice, the user can define the maximum number of layers that are simulated. SnowModel/SnowModel-LG includes an algorithm that merges any relatively thin (e.g., thermodynamically unimportant) layer with the layer below to prevent the layer-limit from being exceeded. The vertical resolution or grid increment of the snowpack is defined by the layer thicknesses; these thicknesses can range from as small as ~1 mm to as large a few tens of centimeters, depending on the precipitation amount that fell during the storm that created the layer. Alternatively, SnowModel/SnowModel-LG can be run with a single-layer snowpack.

Each snow layer in the snowpack carries and evolves its own physical properties, like thickness, grain size, density, and thermal conductivity. Because the snowpack layer thicknesses are changing with time, the resolution of the vertical grid is also changing with time. The vertical grid defined by this snow-layer structure is used to solve for the temperature profile in Equation C1. Examples of this snowpack layer structure is provided by Liston and Mernild (2012) and Liston et al. (2018).

G3. Precipitation Drizzle Adjustments

The tendency of atmospheric (re)analyses products to continuously drizzle in time (defined by Boisvert et al., 2018; Dai, 2006; Radionov et al., 1997, to be $\leq 1 \text{ mm day}^{-1}$) does not generally represent the natural system, and is not compatible with SnowModel's/SnowModel-LG's discrete-precipitation-event snow-layer formation approach. For example, if there is a nonzero snowfall value during each winter time step of the simulation, only a single snow layer will be produced by SnowModel/SnowModel-LG. Boisvert et al. (2018) compared drifting ice mass balance buoy data with Arctic Ocean precipitation estimates from eight atmospheric reanalyses from 2000–2016. They found the 1 mm day^{-1} drizzle threshold produces more snow-accumulation-producing storms than are observed. This suggests that to accurately identify individual storms that produce their own unique snow layers, a reanalysis clipping precipitation threshold $> 1 \text{ mm day}^{-1}$ is likely required. Dai (2006) found that coupled global climate models overestimate the frequency of light precipitation, defined to be precipitation falling at rates of $1\text{--}10 \text{ mm day}^{-1}$.

To correct this unrealistic tendency to drizzle, MicroMet sweeps through, in time, any prescribed (re)analyses precipitation forcing, and clips minimal values to create discrete precipitation events. The clipped precipitation is then added to the remaining nonzero precipitation periods, thus conserving the total, temporally integrated, (re)analyses precipitation quantities. Clipping levels are defined (either by the user or from some objective procedure) so the resulting precipitation events approximately match synoptic precipitation-frequency time scales.

G4. Other Atmospheric Forcing Variables

MicroMet's air temperature, relative humidity, and wind speed and direction adjustments for topography are described in detail through Equations 2–19 of Liston and Elder (2006b). Incoming solar and longwave radiation reaching Earth's surface are given by Equations F2–F12 and F15–F17, above, respectively. Surface pressure is given by Equation C6 above.

A general summary of MicroMet, and how it couples with SnowModel/SnowModel-LG, is provided by Liston and Elder (2006b).

Appendix H: SnowAssim

SnowAssim (Liston & Hiemstra, 2008) is designed specifically to assimilate ground-based and remotely sensed snow data within SnowModel/SnowModel-LG. SnowAssim is consistent with optimal interpolation data assimilation approaches, where the differences between the observed and modeled snow values are used to constrain modeled outputs. The calculated corrections are applied backward in time to create improved fields prior to the assimilated observations. Thus, one of the advantages of this scheme is improved simulation of snow-related distributions throughout the entire snow season, even when observations are only available late in the accumulation and/or during the ablation periods.

Simulations using SnowAssim display considerably more realistic spatial heterogeneity and temporal evolution than those provided by models or observations alone (Liston et al., 2007, 2008; Stuefer et al., 2013). SnowAssim is described by Equations 1–9 of Liston and Hiemstra (2008).

Data Availability Statement

Parcel tracking data were provided by M. Tschudi and S. Stewart. The NSIDC ice-age data are available online (<https://nsidc.org/data/nsidc-0611/versions/4>). The OSI-SAF sea-ice type data are available online (<http://www.osi-saf.org/?q=content/global-sea-ice-type-c>). Daily, 1 September 1980 through 31 July 2018, EASE-grid snow depths and densities presented in this paper are available at the National Snow and Ice Data Center (NSIDC), Boulder, Colorado USA: Liston, G. E., J. Stroeve, and P. Itkin; Lagrangian Snow Distributions for Sea-Ice Applications; <http://dx.doi.org/10.5067/27A0P5M6LZBI>.

Acknowledgments

This work was funded under NASA Grants NNX16AK85G and 80NSSC18K0571; European Space Agency Grant ITT 4000118057/16/I-NB; and National Science Foundation Grants 1602889 and 1820927. P. Itkin's contribution was funded by Norwegian Research Council project 287871 and a travel grant by UiT and CSU in summer 2019. The authors thank C. Polashenski for discussions about how snow blowing into leads affects the snowpack's mass budget. We also thank I. Merkouriadi and two anonymous reviewers for their insightful comments on an early version of the manuscript.

References

- Aaboe, S., Breivik, L.-A., Sørensen, A., Eastwood, S., & Laverne, T. (2018). *Global sea ice edge and type product user's manual OSI-402-c & OSI-403-c version 2.3, EUMETSAT*. Retrieved from http://osisaf.met.no/docs/osisaf_cdop3_ss2_pum_sea-ice-edge-type_v2p3.pdf
- Anderson, E. A. (1976). *A point energy and mass balance model of a snow cover* (NOAA, Technical Report NWS 19) (pp. 1–150).
- Barrett, A. P., Stroeve, J. C., & Serreze, M. C. (2020). Arctic Ocean precipitation from atmospheric reanalyses and comparisons with North Pole drifting station records. *Journal of Geophysical Research: Oceans*, 125, e2019JC015415. <https://doi.org/10.1029/2019JC015415>
- Benson, C. S., & Sturm, M. (1993). Structure and wind transport of seasonal snow on the Arctic slope of Alaska. *Annals of Glaciology*, 18, 261–267. <https://doi.org/10.3189/S0260305500011629>
- Blanchard-Wrigglesworth, E., Webster, M., Farrell, S., & Bitz, C. M. (2018). Reconstruction of Arctic snow on sea ice. *Journal of Geophysical Research: Oceans*, 123, 3588–3602. <https://doi.org/10.1002/2017JC013364>
- Boelman, N., Liston, G. E., Gurarie, E., Meddens, A. J. H., Mahoney, P. J., Kirchner, P. B., et al. (2019). Integrating snow science and wildlife ecology in Arctic-boreal North America. *Environmental Research Letters*, 14(1), 010401. <https://doi.org/10.1088/1748-9326/aaec1>
- Bogdanova, E. G., Ilyin, B. M., & Dragomilova, I. V. (2002). Application of a comprehensive bias-correction model to precipitation measured at Russian North Pole drifting stations. *Journal of Hydrometeorology*, 3(6), 700–713. [https://doi.org/10.1175/1525-7541\(2002\)003%3C0700:AOACBC%3E2.0.CO;2](https://doi.org/10.1175/1525-7541(2002)003%3C0700:AOACBC%3E2.0.CO;2)
- Boisvert, L., Webster, M. A., Petty, A. A., Markus, T., Bromwich, D. H., & Cullather, R. I. (2018). Intercomparison of precipitation estimates over the Arctic Ocean and its peripheral seas from reanalyses. *Journal of Climate*, 31(20), 8441–8462. <https://doi.org/10.1175/JCLI-D-18-0125.1>
- Brodzik, M. J., & Knowles, K. W. (2002). Chapter 5: EASE-grid: A versatile set of equal-area projections and grids. In M. F. Goodchild (Ed.), *Discrete global grids: A web book* (pp. 98–113). Santa Barbara, CA: National Center for Geographic Information & Analysis. Retrieved from <https://escholarship.org/uc/item/9492q6sm>
- Bruland, O., Liston, G. E., Vonk, J., & Killingtveit, A. (2004). Modelling the snow distribution at two high-Arctic sites at Svalbard, Norway, and at a sub-Arctic site in Central Norway. *Nordic Hydrology*, 35(3), 191–208. <https://doi.org/10.2166/nh.2004.0014>
- Buck, A. L. (1981). New equations for computing vapor pressure and enhancement factor. *Journal of Applied Meteorology*, 20(12), 1527–1532. [https://doi.org/10.1175/1520-0450\(1981\)020<1527:NEFCVP>2.0.CO;2](https://doi.org/10.1175/1520-0450(1981)020<1527:NEFCVP>2.0.CO;2)
- Burden, R. L., & Faires, J. D. (1989). *Numerical analysis*. Boston: PWS-KENT Publishing Company.
- Burridge, D. M., & Gadd, A. J. (1974). *The Meteorological Office operational 10 level numerical weather prediction model (December 1974)* (British Met. Office Tech. Notes Nos. 12 and 48) (pp. 1–57). Berkshire, England.
- Cavalieri, D. J., & Parkinson, C. L. (2012). Arctic sea ice variability and trends, 1979–2010. *The Cryosphere*, 6(4), 881–889. <https://doi.org/10.5194/tc-6-881-2012>
- Cavalieri, D. J., Parkinson, C. L., Gloersen, P., & Zwally, H. J. (1996). *Sea ice concentrations from Nimbus-7 SMMR and DMSP SSM/I-SSMIS passive microwave data, version 1*. Boulder, CO: NASA National Snow and Ice Data Center Distributed Active Archive Center. <https://doi.org/10.5067/8GQ8LZQVLOVL>
- Dai, A. (2006). Precipitation characteristics in eighteen coupled climate models. *Journal of Climate*, 19(18), 4605–4630. <https://doi.org/10.1175/JCLI3884.1>
- Dai, A. (2008). Temperature and pressure dependence of the rain-snow phase transition over land and ocean. *Geophysical Research Letters*, 35, L12802. <https://doi.org/10.1029/2008GL033295>

- Dee, D. P., Uppala, S. M., Simmons, A. J., Berrisford, P., Poli, P., Kobayashi, S., et al. (2011). The ERA-Interim reanalysis: Configuration and performance of the data assimilation system. *Quarterly Journal of the Royal Meteorological Society*, 137(656), 553–597. <https://doi.org/10.1002/qj.828>
- Déry, S. J., & Tremblay, L.-B. (2004). Modeling the effects of wind redistribution on the snow mass budget of polar sea ice. *Journal of Physical Oceanography*, 34(1), 258–271. [https://doi.org/10.1175/1520-0485\(2004\)034<0258:MTEOWR>2.0.CO;2](https://doi.org/10.1175/1520-0485(2004)034<0258:MTEOWR>2.0.CO;2)
- Doumani, G. A. (1967). Surface structures in snow. *Physics Snow Ice: Proceedings*, 1(2), 1119–1136.
- Douville, H., Royer, J. F., & Mahfouf, J. F. (1995). A new snow parameterization for the Meteo-France climate model. Part 1. Validation in stand-alone experiments. *Climate Dynamics*, 12(1), 21–35.
- Fernández-Méndez, M., Olsen, L. M., Kauko, H. M., Meyer, A., Rösel, A., Merkouriadi, I., et al. (2018). Algal hot spots in a changing Arctic Ocean: Sea-ice ridges and the snow-ice interface. *Frontiers in Marine Science*, 5. <https://doi.org/10.3389/fmars.2018.00075>
- Filhol, S., & Sturm, M. (2015). Snow bedforms: A review, new data, and a formation model. *Journal of Geophysical Research: Earth Surface*, 120, 1645–1669. <https://doi.org/10.1002/2015JF003529>
- Fletcher, S. J., Liston, G. E., Hiemstra, C. A., & Miller, S. D. (2012). Assimilating MODIS and AMSR-E snow observations in a snow evolution model. *Journal of Hydrometeorology*, 13(5), 1475–1492. <https://doi.org/10.1175/JHM-D-11-082.1>
- Gascoin, S., Lhermitte, S., Kinnard, C., Borstel, K., & Liston, G. E. (2012). Wind effects on snow cover in Pascua-Lama, dry Andes of Chile. *Advances in Water Resources*, 55, 25–39.
- Gelaro, R., McCarty, W., Suárez, M. J., Todling, R., Molod, A., Takacs, L., et al. (2017). The Modern-Era Retrospective Analysis for Research and Applications, Version 2 (MERRA-2). *Journal of Climate*, 30(14), 5419–5454. <https://doi.org/10.1175/JCLI-D-16-0758.1>
- Graham, R., Itkin, P., Meyer, A., Sundfjord, A., Spreen, G., Smedsrud, L. H., et al. (2019). Winter storms accelerate the demise of sea ice in the Atlantic sector of the Arctic Ocean. *Scientific Reports*, 9(1), 9222. <https://doi.org/10.1038/s41598-019-45574-5>
- Granskog, M. A., Leppäranta, M., Kawamura, T., Ehn, J., & Shirasawa, K. (2004). Seasonal development of the properties and composition of landfast sea ice in the Gulf of Finland, the Baltic Sea. *Journal of Geophysical Research*, 109, C02020. <https://doi.org/10.1029/2003JC001874>
- Granskog, M. A., Rösel, A., Dodd, P. A., Divine, D. V., Gerland, S., Martma, T., & Leng, M. J. (2017). Snow contribution to first-year and second-year Arctic sea ice mass balance north of Svalbard. *Journal of Geophysical Research: Oceans*, 122, 2539–2549. <https://doi.org/10.1002/2016JC012398>
- Greene, E. M., Liston, G. E., & Pielke, R. A. Sr. (1999). Simulation of above treeline snowdrift formation using a numerical snow-transport model. *Cold Regions Science and Technology*, 30(1-3), 135–144. [https://doi.org/10.1016/S0165-232X\(99\)00008-7](https://doi.org/10.1016/S0165-232X(99)00008-7)
- Haas, C., Beckers, J., King, J., Silis, A., Stroeve, J., Wilkinson, J., et al. (2017). Ice and snow thickness variability and change in the high Arctic Ocean observed by in situ measurements. *Geophysical Research Letters*, 44, 10,462–10,469. <https://doi.org/10.1002/2017GL075434>
- Haas, C., Thomas, D. N., & Bareiss, J. (2001). Surface properties and processes of perennial Antarctic sea ice in summer. *Journal of Glaciology*, 47(159), 613–625. <https://doi.org/10.3189/172756501781831864>
- Hancke, K., Lund-Hansen, L. C., Lamare, M. L., Højlund Pedersen, S., King, M. D., Andersen, P., & Sorrell, B. K. (2018). Extreme low light requirement for algae growth underneath sea ice: A case study from Station Nord, NE Greenland. *Journal of Geophysical Research: Oceans*, 123, 985–1000. <https://doi.org/10.1002/2017JC013263>
- Hasholt, B., Liston, G. E., & Knudsen, N. T. (2003). Snow distribution modelling in the Ammassalik Region, south East Greenland. *Nordic Hydrology*, 34(1–2), 1–16. <https://doi.org/10.2166/nh.2003.0025>
- Hersbach, H., Bell, B., Berrisford, P., Hirahara, S., Horányi, A., Muñoz-Sabater, J., et al. (2020). The ERA5 global reanalysis. *Quarterly Journal of the Royal Meteorological Society*, 146(730), 1999–2049. <https://doi.org/10.1002/qj.3803>
- Hezel, P., Zhang, X., Bitz, C., Kelly, B., & Massonnet, F. (2012). Projected decline in spring snow depth on Arctic sea ice caused by progressively later autumn open ocean freeze-up this century. *Geophysical Research Letters*, 39, L17505. <https://doi.org/10.1029/2012GL052794>
- Hiemstra, C. A., Liston, G. E., Pielke, R. A. Sr., Birkenheuer, D. L., & Albers, S. C. (2006). Comparing Local Analysis and Prediction System (LAPS) assimilations with independent observations. *Weather and Forecasting*, 21(6), 1024–1040. <https://doi.org/10.1175/WAF961.1>
- Hiemstra, C. A., Liston, G. E., & Reiners, W. A. (2002). Snow redistribution by wind and interactions with vegetation at upper treeline in the Medicine Bow Mountains, Wyoming, USA. *Arctic, Antarctic, and Alpine Research*, 34(3), 262–273. <https://doi.org/10.1080/15230430.2002.12003493>
- Hoffman, M. J., Fountain, A. G., & Liston, G. E. (2014). Near-surface internal melting—A substantial mass loss on Antarctic Dry Valley glaciers. *Journal of Glaciology*, 60(220), 361–374. <https://doi.org/10.3189/2014JoG13J095>
- Hoffman, M. J., Fountain, A. G., & Liston, G. E. (2016). Distributed modeling of ablation (1996–2011) and climate sensitivity on the glaciers of Taylor Valley, Antarctica. *Journal of Glaciology*, 62(232), 215–229. <https://doi.org/10.1017/jog.2015.2>
- Holland, M. M., Bailey, D. A., Briegleb, B. P., Light, B., & Hunke, E. (2012). Improved sea ice shortwave radiation physics in CCSM4: The impact of melt ponds and aerosols on Arctic sea ice. *Journal of Climate*, 25, 1413–1430. <https://doi.org/10.1175/JCLI-D-11-00078.1>
- Holland, M. M., & Landrum, L. (2015). Factors affecting projected Arctic surface shortwave heating and albedo change in coupled climate models. *Philosophical Transactions of the Royal Society A*, 373(2045), 20140162. <https://doi.org/10.1098/rsta.2014.0162>
- Hunke, E. C., Hebert, D. A., & Lecomte, O. (2013). Level-ice melt ponds in the Los Alamos sea ice model, CICE. *Ocean Modelling*, 71, 26–42. <https://doi.org/10.1016/j.ocemod.2012.11.008>
- Hurley, A. R. (2014). *Comparison and validation of Arctic precipitation fields from three atmospheric reanalyses: CFSR, MERRA, ERA-Interim* (Geography graduate theses & dissertations, p. 75). Retrieved from http://scholar.colorado.edu/geog_gradetds/75
- Itkin, P., Spreen, G., Hvidegaard, S. M., Skourup, H., Wilkinson, J., Gerland, S., & Granskog, M. A. (2018). Contribution of deformation to sea-ice mass balance: A case study from an N-ICE2015 storm. *Geophysical Research Letters*, 45, 789–796. <https://doi.org/10.1002/2017GL076056>
- Iziomon, M. G., Mayer, H., & Matzarakis, A. (2003). Downward atmospheric longwave irradiance under clear and cloudy skies: Measurement and parameterization. *Journal of Atmospheric and Solar-Terrestrial Physics*, 65(10), 1107–1116. <https://doi.org/10.1016/j.jastp.2003.07.007>
- Jordan, R. (1991). *A one-dimensional temperature model for a snow cover: Technical documentation for SNTherm* (Tech. Rep. 89). Hanover, NH: Cold Regions Research and Engineering Lab. Retrieved from <https://apps.dtic.mil/docs/citations/ADA245493>
- Kind, R. J. (1981). Chapter 8. Drifting snow. In D. M. Gray, & D. H. Male (Eds.), *Handbook of Snow, Principles, Processes, Management and Use* (pp. 338–359). Toronto: Pergamon Press.
- King, J., Howell, S., Derksen, C., Rutter, N., Toose, P., Beckers, J. F., et al. (2015). Evaluation of Operation IceBridge quick-look snow depth estimates on sea ice. *Geophysical Research Letters*, 42, 9302–9310. <https://doi.org/10.1002/2015GL066389>

- Kojima, K. (1967). *Densification of seasonal snow cover. Physics of snow and ice* (pp. 929–952). Paper presented at Proceedings of International Conference on Low Temperature Science, Institute of low Temperature Science, Hokkaido University, Sapporo, Japan.
- Kwok, R. (2018). Arctic sea ice thickness, volume, and multiyear ice coverage: Losses and coupled variability (1958–2018). *Environmental Research Letters*, 13(10), 105005. <https://doi.org/10.1088/1748-9326/aae3ec>
- Kwok, R., & Cunningham, G. F. (2008). ICESat over Arctic sea ice: Estimation of snow depth and ice thickness. *Journal of Geophysical Research*, 113, C08010. <https://doi.org/10.1029/2008JC004753>
- Kwok, R., Kurtz, N. T., Brucker, L., Ivanoff, A., Newman, T., Farrell, S. L., et al. (2017). Intercomparison of snow depth retrievals over Arctic sea ice from radar data acquired by Operation Ice Bridge. *The Cryosphere*, 11(6), 2571–2593. <https://doi.org/10.5194/tc-11-2571-2017>
- Kwok, R., Schweiger, A., Rothrock, D. A., Pang, S., & Kottmeier, C. C. (1998). Sea ice motion from satellite passive microwave imagery assessed with ERS SAR and buoy motions. *Journal of Geophysical Research*, 103(C4), 8191–8214. <https://doi.org/10.1029/97JC03334>
- Kyle, H. L., Ardanuy, P. E., & Hurley, E. J. (1985). The status of the Nimbus-7 earth-radiation-budget data set. *Bulletin of American Meteorological Society*, 66(11), 1378–1388. [https://doi.org/10.1175/1520-0477\(1985\)066<1378:TSOTER>2.0.CO;2](https://doi.org/10.1175/1520-0477(1985)066<1378:TSOTER>2.0.CO;2)
- LaChapelle, E. R. (1969). *Properties of snow* (pp. 1–21). Seattle: College of Forest Resources, University of Washington.
- Lecomte, O., Fichet, T., Flocco, D., Schröder, D., & Vancoppenolle, M. (2015). Interactions between wind-blown snow redistribution and melt ponds in a coupled ocean–sea ice model. *Ocean Modelling*, 87, 67–80. <https://doi.org/10.1016/j.ocemod.2014.12.003>
- Lecomte, O., Fichet, T., Vancoppenolle, M., Domine, F., Massonnet, F., Mathiot, P., et al. (2013). On the formulation of snow thermal conductivity in large-scale sea ice models. *Journal of Advances in Modeling Earth Systems*, 5, 542–557. <https://doi.org/10.1002/jame.20039>
- Leonard, K. C., & Maksym, T. (2011). The importance of wind-blown snow redistribution to snow accumulation on Bellingshausen Sea ice. *Annals of Glaciology*, 52(57), 271–278. <https://doi.org/10.3189/172756411795931651>
- Li, L., & Pomeroy, J. W. (1997). Estimates of threshold wind speeds for snow transport using meteorological data. *Journal of Applied Meteorology*, 36(3), 205–213. [https://doi.org/10.1175/1520-0450\(1997\)036<0205:EOTWSF>2.0.CO;2](https://doi.org/10.1175/1520-0450(1997)036<0205:EOTWSF>2.0.CO;2)
- Lindsay, R. (1998). Temporal variability of the energy balance of thick Arctic pack ice. *Journal of Climate*, 11(3), 313–333. [https://doi.org/10.1175/1520-0442\(1998\)011<0313:TVOTEB>2.0.CO;2](https://doi.org/10.1175/1520-0442(1998)011<0313:TVOTEB>2.0.CO;2)
- Lindsay, R., Wensnahan, M., Schweiger, A., & Zhang, J. (2014). Evaluation of seven different atmospheric reanalysis products in the Arctic. *Journal of Climate*, 27(7), 2588–2606. <https://doi.org/10.1175/JCLI-D-13-00014.1>
- Lindsay, R. W., & Schweiger, A. (2015). Arctic sea ice thickness loss determined using subsurface, aircraft, and satellite observations. *The Cryosphere*, 9(1), 269–283. <https://doi.org/10.5194/tc-9-269-2015>
- Lipscomb, W. H., & Hunke, E. C. (2004). Modeling sea ice transport using incremental remapping. *Monthly Weather Review*, 132(6), 1341–1354. [https://doi.org/10.1175/1520-0493\(2004\)132<1341:MSITU1>2.0.CO;2](https://doi.org/10.1175/1520-0493(2004)132<1341:MSITU1>2.0.CO;2)
- Liston, G. E. (1995). Local advection of momentum, heat, and moisture during the melt of patchy snow covers. *Journal of Applied Meteorology*, 34(7), 1705–1715. <https://doi.org/10.1175/1520-0450-34.7.1705>
- Liston, G. E., & Elder, K. (2006a). A distributed snow-evolution modeling system (SnowModel). *Journal of Hydrometeorology*, 7(6), 1259–1276. <https://doi.org/10.1175/JHM548.1>
- Liston, G. E., & Elder, K. (2006b). A meteorological distribution system for high-resolution terrestrial modeling (MicroMet). *Journal of Hydrometeorology*, 7(2), 217–234. <https://doi.org/10.1175/JHM486.1>
- Liston, G. E., Haehnel, R. B., Sturm, M., Hiemstra, C. A., Berezovskaya, S., & Tabler, R. D. (2007). Simulating complex snow distributions in windy environments using SnowTran-3D. *Journal of Glaciology*, 53(181), 241–256. <https://doi.org/10.3189/172756507782202865>
- Liston, G. E., & Hall, D. K. (1995). An energy balance model of lake ice evolution. *Journal of Glaciology*, 41(138), 373–382. <https://doi.org/10.1017/S0022143000016245>
- Liston, G. E., & Hiemstra, C. A. (2008). A simple data assimilation system for complex snow distributions (SnowAssim). *Journal of Hydrometeorology*, 9(5), 989–1004. <https://doi.org/10.1175/2008JHM871.1>
- Liston, G. E., & Hiemstra, C. A. (2011a). The changing cryosphere: Pan-Arctic snow trends (1979–2009). *Journal of Climate*, 24(21), 5691–5712. <https://doi.org/10.1175/JCLI-D-11-00081.1>
- Liston, G. E., & Hiemstra, C. A. (2011b). Representing grass- and shrub-snow-atmosphere interactions in climate system models. *Journal of Climate*, 24(8), 2061–2079. <https://doi.org/10.1175/2010JCLI4028.1>
- Liston, G. E., Hiemstra, C. A., Elder, K., & Cline, D. W. (2008). Meso-cell study area (MSA) snow distributions for the Cold Land Processes Experiment (CLPX). *Journal of Hydrometeorology*, 9(5), 957–976. <https://doi.org/10.1175/2008JHM869.1>
- Liston, G. E., McFadden, J. P., Sturm, M., & Pielke, R. A. Sr. (2002). Modeled changes in arctic tundra snow, energy, and moisture fluxes due to increased shrubs. *Global Change Biology*, 8(1), 17–32. <https://doi.org/10.1046/j.1354-1013.2001.00416.x>
- Liston, G. E., & Mernild, S. H. (2012). Greenland freshwater runoff. Part I: A runoff routing model for glaciated and non-glaciated landscapes (HydroFlow). *Journal of Climate*, 25(17), 5997–6014. <https://doi.org/10.1175/JCLI-D-11-00591.1>
- Liston, G. E., Perham, C. J., Shideler, R. T., & Cheuvront, A. N. (2016). Modeling snowdrift habitat for polar bear dens. *Ecological Modelling*, 320, 114–134. <https://doi.org/10.1016/j.ecolmodel.2015.09.010>
- Liston, G. E., Polashenski, C., Rösel, A., Itkin, P., King, J., Merkouriadi, I., & Haapala, J. (2018). A distributed snow-evolution model for sea-ice applications (SnowModel). *Journal of Geophysical Research: Oceans*, 123, 3786–3810. <https://doi.org/10.1002/2017JC013706>
- Liston, G. E., & Sturm, M. (1998). A snow-transport model for complex terrain. *Journal of Glaciology*, 44(148), 498–516. <https://doi.org/10.1017/S0022143000002021>
- Liston, G. E., & Sturm, M. (2002). Winter precipitation patterns in arctic Alaska determined from a blowing-snow model and snow-depth observations. *Journal of Hydrometeorology*, 3(6), 646–659. [https://doi.org/10.1175/1525-7541\(2002\)003<0646:WPPIAA>2.0.CO;2](https://doi.org/10.1175/1525-7541(2002)003<0646:WPPIAA>2.0.CO;2)
- Liston, G. E., & Sturm, M. (2004). The role of winter sublimation in the Arctic moisture budget. *Nordic Hydrology*, 35(4–5), 325–334. <https://doi.org/10.2166/nh.2004.0024>
- Liston, G. E., & Winther, J.-G. (2005). Antarctic surface and subsurface snow and ice melt fluxes. *Journal of Climate*, 18(10), 1469–1481. <https://doi.org/10.1175/JCLI3344.1>
- Liston, G. E., Winther, J.-G., Bruland, O., Elvehøy, H., & Sand, K. (1999). Below-surface ice melt on the coastal Antarctic ice sheet. *Journal of Glaciology*, 45(150), 273–285. <https://doi.org/10.3189/s0022143000001775>
- Liston, G. E., Winther, J.-G., Bruland, O., Elvehøy, H., Sand, K., & Karlöf, L. (2000). Snow and blue-ice distribution patterns on the coastal Antarctic ice sheet. *Antarctic Science*, 12(1), 69–79. <https://doi.org/10.1017/S0954102000000109>
- Louis, J. -F. (1979). A parametric model of vertical eddy fluxes in the atmosphere. *Boundary-Layer Meteorology*, 17(2), 187–202. <https://doi.org/10.1007/BF00117978>

- Markus, T., Stroeve, J. C., & Miller, J. (2009). Recent changes in Arctic sea ice melt onset, freezeup, and melt season length. *Journal of Geophysical Research*, 114, C12024. <https://doi.org/10.1029/2009JC005436>
- Maslanik, J., Stroeve, J., Fowler, C., & Emery, W. (2011). Distribution and trends in Arctic sea ice age through spring 2011. *Geophysical Research Letters*, 38, L13502. <https://doi.org/10.1029/2011GL047735>
- Maslanik, J. A., Fowler, C., Stroeve, J., Drobot, S., Zwally, J., Yi, D., & Emery, W. (2007). A younger, thinner Arctic ice cover: Increased potential for rapid extensive sea ice loss. *Geophysical Research Letters*, 34, L24501. <https://doi.org/10.1029/2007/GL032043>
- Maykut, G. A., & Untersteiner, N. (1971). Some results from a time-dependent thermodynamic model of sea ice. *Journal of Geophysical Research*, 76(6), 1550–1575. <https://doi.org/10.1029/JC076i006p01550>
- Meier, W. N., Maslanik, J. A., & Fowler, C. W. (2000). Error analysis and assimilation of remotely sensed ice motion within an Arctic sea ice model. *Journal of Geophysical Research*, 105(C2), 3339–3356. <https://doi.org/10.1029/1999JC900268>
- Merkouriadi, I., Cheng, B., Graham, R. M., Rösel, A., & Granskog, M. A. (2017). Critical role of snow on sea ice growth in the Atlantic sector of the Arctic Ocean. *Geophysical Research Letters*, 44, 10,479–10,485. <https://doi.org/10.1002/2017GL075494>
- Merkouriadi, I., Liston, G. E., Graham, R. M., & Granskog, M. A. (2020). Quantifying the potential for snow-ice formation in the Arctic Ocean. *Geophysical Research Letters*, 47, e2019GL085020. <https://doi.org/10.1029/2019GL085020>
- Mernild, S., Hasholt, H. B., & Liston, G. E. (2008). Climatic control on river discharge simulations, Zackenberg River drainage basin, northeast Greenland. *Hydrological Processes*, 22(12), 1932–1948. <https://doi.org/10.1002/hyp.6777>
- Mernild, S. H., Holland, D. M., Holland, D., Rosing-Asvid, A., Yde, J. C., Liston, G. E., & Steffen, K. (2015). Freshwater flux and spatiotemporal simulated runoff variability into Ilulissat Icefjord, West Greenland, linked to salinity and temperature observations near tidewater glacier margins obtained using instrumented ringed seals. *Journal of Physical Oceanography*, 45(5), 1426–1445. <https://doi.org/10.1175/JPO-D-14-0217.1>
- Mernild, S. H., & Liston, G. E. (2010). The influence of air temperature inversions on snowmelt and glacier mass-balance simulations, Ammassalik Island, SE Greenland. *Journal of Applied Meteorology and Climatology*, 49(1), 47–67. <https://doi.org/10.1175/2009JAMC2065.1>
- Mernild, S. H., Liston, G. E., Hasholt, B., & Knudsen, N. T. (2006). Snow-distribution and melt modeling for Mittivakkat Glacier, Ammassalik Island, Southeast Greenland. *Journal of Hydrometeorology*, 7(4), 808–824. <https://doi.org/10.1175/JHM522.1>
- Mernild, S. H., Liston, G. E., & Hiemstra, C. A. (2014). Northern hemisphere glacier and ice cap surface mass balance and contribution to sea level rise. *Journal of Climate*, 27(15), 6051–6073. <https://doi.org/10.1175/JCLI-D-13-00669.1>
- Mernild, S. H., Liston, G. E., Hiemstra, C. A., & Christensen, J. H. (2010). Greenland ice sheet surface mass-balance modeling in a 131-year perspective, 1950–2080. *Journal of Hydrometeorology*, 11(1), 3–25. <https://doi.org/10.1175/2009jhm1140.1>
- Mernild, S. H., Liston, G. E., Hiemstra, C. A., Steffen, K., Hanna, E., & Christensen, J. H. (2009). Greenland ice sheet surface mass-balance modelling and freshwater flux for 2007, and in a 1995–2007 perspective. *Hydrological Processes*, 23(17), 2470–2484. <https://doi.org/10.1002/hyp.7354>
- Mernild, S. H., Mote, T. L., & Liston, G. E. (2011). Greenland ice sheet surface melt extent and trends, 1960–2010. *Journal of Glaciology*, 57(204), 621–628. <https://doi.org/10.3189/002214311797409712>
- Mundy, C. J., Barber, D. G., & Michel, C. (2005). Variability of snow and ice thermal, physical and optical properties pertinent to sea ice algae biomass during spring. *Journal of Marine Systems*, 58(3–4), 107–120. <https://doi.org/10.1016/j.jmarsys.2005.07.003>
- NSIDC (2016). IceBridge sea ice freeboard, snow depth, and thickness quick look, version 1. National Snow and Ice Data Center, doi: <https://doi.org/10.5067/GRIZ91DE0L9>
- Overland, J. E., Walter, B. A., Curtin, T. B., & Turet, P. (1995). Hierarchy and sea ice mechanics: A case study from the Beaufort Sea. *Journal of Geophysical Research*, 100(C3), 4559–4571. <https://doi.org/10.1029/94JC02502>
- Patankar, S. V. (1980). *Numerical heat transfer and fluid flow* (p. 197). New York: Hemisphere Publishing.
- Pedersen, S. H. (2017). *Scaling-up climate change effects in Greenland* (PhD thesis, pp. 1–178). Roskilde, Denmark: Department of Bioscience, Aarhus University.
- Pedersen, S. H., Liston, G. E., Tamstorf, M. P., Abermann, J., & Schmidt, N. M. (2018). Quantifying snow controls on vegetation greenness. *Ecosphere*, 9(6), e02309. <https://doi.org/10.1002/ecs2.2309>
- Pedersen, S. H., Liston, G. E., Tamstorf, M. P., Westergaard-Nielsen, A., & Schmidt, N. M. (2015). Quantifying episodic snowmelt events in Arctic ecosystems. *Ecosystems*, 18(5), 839–856. <https://doi.org/10.1007/s10021-015-9867-8>
- Perovich, D., Meier, W., Tschudi, M., Farrell, S., Hendricks, S., Gerland, S., et al. (2019). In J. Richter-Menge, M. L. Druckenmiller, & M. Jeffries (Eds.), *Sea ice. Arctic report card 2019* (pp. 26–34). Washington, DC: National Oceanic and Atmospheric Administration (NOAA). Retrieved from <http://www.arctic.noaa.gov/Report-Card>
- Petrich, C., Eicken, H., Polashenski, C. M., Sturm, M., Harbeck, J. P., Perovich, D. K., & Finnegan, D. C. (2012). Snow dunes: A controlling factor of melt pond distribution on Arctic sea ice. *Journal of Geophysical Research*, 117, C09029. <https://doi.org/10.1029/2012JC008192>
- Petty, A. A., Webster, M., Boisvert, L. N., & Markus, T. (2018). The NASA Eulerian Snow on Sea Ice Model (NESOSIM): Initial model development and analysis. *Geoscientific Model Development*, 11(11), 4577–4602. <https://doi.org/10.5194/gmd-2018-84>
- Pflug, J. M., Liston, G. E., Nijssen, B., & Lundquist, J. D. (2019). Testing model representations of snowpack liquid water percolation across multiple climates. *Water Resources Research*, 55, 2018WR024632. <https://doi.org/10.1029/2018WR024632>
- Polashenski, C., Perovich, D., & Courville, Z. (2012). The mechanisms of sea ice melt pond formation and evolution. *Journal of Geophysical Research*, 117, C01001. <https://doi.org/10.1029/2011JC007231>
- Pomeroy, J. W., & Gray, D. M. (1995). *Snowcover accumulation, relocation and management (National Hydrology Research Institute Science Report No. 7)* (pp. 1–144). Saskatoon: Hydrological Sciences Division, NHRI Division of Hydrology, University of Saskatchewan.
- Pomeroy, J. W., Gray, D. M., & Landine, P. G. (1993). The prairie blowing snow model—Characteristics, validation, operation. *Journal of Hydrology*, 144(1–4), 165–192. [https://doi.org/10.1016/0022-1694\(93\)90171-5](https://doi.org/10.1016/0022-1694(93)90171-5)
- Prasad, R., Tarboton, D. G., Liston, G. E., Luce, C. H., & Seyfried, M. S. (2001). Testing a blowing snow model against distributed snow measurements at Upper Sheep Creek, Idaho, USA. *Water Resources Research*, 37(5), 1341–1357.
- Price, A. G., & Dunne, T. (1976). Energy balance computations of snowmelt in a subarctic area. *Water Resources Research*, 12(4), 686–694. <https://doi.org/10.1029/WR012i004p00686>
- Provost, C., Sennéchal, N., Miguët, J., Itkin, P., Rösel, A., Koenig, Z., et al. (2017). Observations of flooding and snow-ice formation in a thinner Arctic sea ice regime during the N-ICE2015 campaign: Influence of basal ice melt and storms. *Journal of Geophysical Research: Oceans*, 122, 7115–7134. <https://doi.org/10.1002/2016JC012011>
- Quarteroni, A., & Valli, A. (1994). *Numerical approximation of partial differential equations*. Berlin: Springer. <https://doi.org/10.1007/978-3-540-85268-1>
- Radionov, V. F., Bryazgin, N. N., & Alexandrov, E. I. (1997). *The snow cover of the Arctic Basin (Applied Physics Laboratory Tech. Rep. APL-UW TR 9701)* (pp. 1–95).

- Rampal, P., Weiss, J., & Marsan, D. (2009). Positive trend in the mean speed and deformation rate of Arctic sea ice, 1979–2007. *Journal of Geophysical Research*, 114, C05013. <https://doi.org/10.1029/2008JC005066>
- Rapaic, M., Brown, R., Markovic, M., & Chaumont, D. (2015). An evaluation of temperature and precipitation surface-based and reanalysis data sets for the Canadian Arctic, 1950–2010. *Atmosphere-Ocean*, 53(3), 283–303. <https://doi.org/10.1080/07055900.2015.1045825>
- Rogers, R. R. (1979). *A short course in cloud physics*. New York: Pergamon Press.
- Rousset, C., Vancoppenolle, M., Madec, G., Fichefet, T., Flavoni, S., Barthélemy, A., et al. (2015). The Louvain-la-Neuve sea ice model LIM3.6: Global and regional capabilities. *Geoscientific Model Development Discussion*, 8(10), 2991–3005. <https://doi.org/10.5194/gmd-8-2991-2015>
- Sadeghi, S.-H., Peters, T. R., Cobos, D. R., Loescher, H. W., & Campbell, C. S. (2013). Direct calculation of thermodynamic wet-bulb temperature as a function of pressure and elevation. *Journal of Atmospheric and Oceanic Technology*, 30(8), 1757–1765. <https://doi.org/10.1175/JTECH-D-12-00191.1>
- Schmidt, R. A. (1972). *Sublimation of wind-transported snow—A model (Research Paper RM-90)* (pp. 1–24). U.S. Forest Service, Rocky Mountain Forest and Range Experiment Station.
- Schmidt, R. A. (1982). Vertical profiles of wind speed, snow concentration, and humidity in blowing snow. *Boundary-Layer Meteorology*, 23(2), 223–246. <https://doi.org/10.1007/BF00123299>
- Schmidt, R. A. (1986). Transport rate of drifting snow and the mean wind speed profile. *Boundary-Layer Meteorology*, 34(3), 213–241. <https://doi.org/10.1007/BF00122380>
- Schmidt, R. A. (1991). Sublimation of snow intercepted by an artificial conifer. *Agricultural and Forest Meteorology*, 54(1), 1–27. [https://doi.org/10.1016/0168-1923\(91\)90038-R](https://doi.org/10.1016/0168-1923(91)90038-R)
- Schröder, D., Feltham, D. L., Tsamados, M., Ridout, A., & Tilling, R. (2019). New insight from CryoSat-2 sea ice thickness for sea ice modelling. *The Cryosphere*, 13(1), 125–139. <https://doi.org/10.5194/tc-13-125-2019>
- Serreze, M. C., Barrett, A. P., & Lo, F. (2005). Northern high-latitude precipitation as depicted by atmospheric reanalyses and satellite retrievals. *Monthly Weather Review*, 133(12), 3407–3430. <https://doi.org/10.1175/MWR3047.1>
- Strack, J. E., Liston, G. E., & Pielke, R. A. Sr. (2004). Modeling snow depth for improved simulation of snow–vegetation–atmosphere interactions. *Journal of Hydrometeorology*, 5(5), 723–734. [https://doi.org/10.1175/1525-7541\(2004\)005<0723:MSDFIS>2.0.CO;2](https://doi.org/10.1175/1525-7541(2004)005<0723:MSDFIS>2.0.CO;2)
- Stroeve, J., Liston, G. E., Buzzard, S., Zhou, L., Mallett, R., Barrett, A., et al. (2020). A Lagrangian snow-evolution system for sea ice applications (SnowModel-LG): Part II—Analyses. *Journal of Geophysical Research: Oceans*, e2019JC015913. <https://doi.org/10.1029/2019JC015913>
- Stroeve, J., & Notz, D. (2018). Changing state of Arctic sea ice across all seasons. *Environmental Research Letters*, 13(10), 103001. <https://doi.org/10.1088/1748-9326/aade56>
- Stuefer, S., Kane, D., & Liston, G. E. (2013). In situ snow water equivalent observations in the U.S. Arctic. *Hydrology Research*, 44(1), 21–34. <https://doi.org/10.2166/nh.2012.177>
- Sturm, M., & Benson, C. (1997). Vapor transport, grain growth and depth-hoar development in the subarctic snow. *Journal of Glaciology*, 43(143), 42–59. <https://doi.org/10.3189/s0022143000002793>
- Sturm, M., Holmgren, J., König, M., & Morris, K. (1997). The thermal conductivity of seasonal snow. *Journal of Glaciology*, 43(143), 26–41. <https://doi.org/10.1017/S0022143000002781>
- Sturm, M., Holmgren, J., & Liston, G. E. (1995). A seasonal snow cover classification system for local to global applications. *Journal of Climate*, 8(5), 1261–1283. [https://doi.org/10.1175/1520-0442\(1995\)008<1261:ASSCCS>2.0.CO;2](https://doi.org/10.1175/1520-0442(1995)008<1261:ASSCCS>2.0.CO;2)
- Sturm, M., & Liston, G. E. (2003). The snow cover on lakes of the Arctic Coastal Plain of Alaska, U.S.A. *Journal of Glaciology*, 49(166), 370–380.
- Sturm, M., McFadden, J. P., Liston, G. E., Chapin, F. S. III, Racine, C. H., & Holmgren, J. (2001). Snow-shrub interactions in arctic tundra: A hypothesis with climatic implications. *Journal of Climate*, 14(3), 336–344. [https://doi.org/10.1175/1520-0442\(2001\)014<0336:SSIIAT>2.0.CO;2](https://doi.org/10.1175/1520-0442(2001)014<0336:SSIIAT>2.0.CO;2)
- Suzuki, K., Kodama, Y., Nakai, T., Liston, G. E., Yamamoto, K., Ohata, T., et al. (2011). Impact of land-use changes on snow in a forested region with heavy snowfall in Hokkaido, Japan. *Hydrological Sciences Journal*, 56(3), 443–467. <https://doi.org/10.1080/02626667.2011.565008>
- Suzuki, K., Liston, G. E., & Kodama, Y. (2015). Variations in winter surface net shortwave radiation caused by land-use change in northern Hokkaido, Japan. *Journal of Forest Research*, 20(2), 281–292. <https://doi.org/10.1007/s10310-015-0478-1>
- Suzuki, K., Liston, G. E., & Matsuo, K. (2015). Estimation of continental-basin-scale sublimation in the Lena River basin, Siberia 2015. *Advances in Meteorology* 286206, <https://doi.org/10.1155/2015/286206>, 1.
- Tschudi, M., Fowler, C., Maskanik, J., & Stroeve, J. (2010). Tracking the movement and changing surface characteristics of Arctic sea ice. *IEEE Journal of Selected Topics in Applied Earth Observations and Remote Sensing*, 3(4), 536–540. <https://doi.org/10.1109/JSTARS.2010.2048305>
- Tschudi, M., Meier, W. N., Stewart, J. S., Fowler, C., & Maslanik, J. (2019a). *Polar Pathfinder Daily 25 km EASE-Grid Sea Ice Motion Vectors, Version 4*. Boulder, CO: NASA National Snow and Ice Data Center Distributed Active Archive Center. <https://doi.org/10.5067/INAWUWO7QH7B>
- Tschudi, M., Meier, W. N., Stewart, J. S., Fowler, C., & Maslanik, J. (2019b). *EASE-Grid Sea Ice Age, Version 4*. Boulder, CO: NASA National Snow and Ice Data Center Distributed Active Archive Center. <https://doi.org/10.5067/UTAV7490FEPB>
- Tschudi, M. A., Meier, W. N., & Stewart, J. S. (2020). An enhancement to sea ice motion and age products at the National Snow and Ice Data Center (NSIDC). *The Cryosphere*, 14(5), 1519–1536. <https://doi.org/10.5194/tc-14-1519-2020>
- Walcek, C. J. (1994). Cloud cover and its relationship to relative humidity during a spring midlatitude cyclone. *Monthly Weather Review*, 122(6), 1021–1035. [https://doi.org/10.1175/1520-0493\(1994\)122<1021:CCAIRT>2.0.CO;2](https://doi.org/10.1175/1520-0493(1994)122<1021:CCAIRT>2.0.CO;2)
- Wallace, J. M., & Hobbs, P. V. (1977). *Atmospheric science, an introductory survey* (p. 467). New York: Academic Press.
- Wang, C., Graham, R. M., Wang, K., Gerland, S., & Granskog, M. A. (2019). Comparison of ERA5 and ERA-Interim near-surface air temperature, snowfall and precipitation over Arctic sea ice: Effects on sea ice thermodynamics and evolution. *The Cryosphere*, 13(6), 1661–1679. <https://doi.org/10.5194/tc-13-1661-2019>
- Warren, S., Rigor, I., Untersteiner, N., Radionov, V. F., Bryazgin, N. N., Aleksandrov, Y. I., & Colony, R. (1999). Snow depth on Arctic sea ice. *Journal of Climate*, 12(6), 1814–1829. [https://doi.org/10.1175/1520-0442\(1999\)012<1814:SDOASI>2.0.CO;2](https://doi.org/10.1175/1520-0442(1999)012<1814:SDOASI>2.0.CO;2)
- Webster, M. A., Parker, C., Boisvert, L., & Kwok, R. (2019). The role of cyclone activity in snow accumulation on Arctic sea ice. *Nature Communications*, 10, 5285. <https://doi.org/10.1038/s41467-019-13299-8>
- Yang, D. (1999). An improved precipitation climatology for the Arctic Ocean. *Geophysical Research Letters*, 26(11), 1625–1628. <https://doi.org/10.1029/1999GL900311>